Alma Mater Studiorum – Università di Bologna

DOTTORATO DI RICERCA IN

Meccanica e Scienze Avanzate dell'Ingegneria
Progetto n. 3 - Meccanica Applicata

Ciclo XXV

Settore Concorsuale di afferenza: 09/A2
Settore Scientifico-Disciplinare: ING-IND/13

MODEL REDUCTION TECHNIQUES IN FLEXIBLE MULTIBODY DYNAMICS WITH APPLICATION TO ENGINE CRANKTRAIN SIMULATION

Presentata da:
Ing. Stefano Ricci

Coordinatore Dottorato:
Prof. Vincenzo Parenti Castelli

Relatore:
Prof. Alessandro Rivola

Esame Finale Anno 2013

Alla mia famiglia

Ringraziamenti

Vorrei innanzitutto ringraziare le persone che hanno contribuito alla realizzazione di questa Tesi di Dottorato.

Ringrazio il Prof. Alessandro Rivola, il mio relatore, per avermi dato l'opportunità di lavorare a questo progetto, per la fiducia e per la sua attenta supervisione.

Un sentito ringraziamento va al Dott. Marco Troncossi, per la sua disponibilità e per il supporto fornito in questi anni. Marco, sarà difficile dimenticare la camminata assurda che abbiamo fatto a Helsinki! Un ringraziamento va anche al Dott. Alberto Martini, con il quale abbiamo condiviso un paio di anni da dottorandi, per i consigli e gli interessanti spunti di discussione.

Un ringraziamento particolare va ai miei colleghi, ed ex-colleghi, della Ducati, in particolare nelle persone di Massimo Rosso, Gabriele Stagni e Michele Mazziotta, per la disponibilità, la simpatia e il supporto nelle fasi iniziali del progetto. Un doveroso grazie anche agli altri miei colleghi per sopportarmi tutti i giorni…

Un grazie di cuore a Simone Delvecchio, per l'impagabile amicizia, la simpatia e la vicinanza nei periodi di difficoltà. Grazie a tutti i miei amici, il cui supporto e la cui stima mi hanno spinto anche quando pensavo di dover desistere.

Un ringraziamento speciale va ai miei genitori e a mio fratello: senza di voi non ce l'avrei mai fatta. Infine a te: grazie per l'amore e l'immenso supporto che mi hai dato in questi anni, e per l'infinita pazienza con la quale mi hai sostenuto in questa esperienza.

Stefano Ricci
Bologna, Marzo 2013

Abstract

The development of a multibody model of a motorbike engine cranktrain is presented in this work, with an emphasis on flexible component model reduction.

A modelling methodology based upon the adoption of non-ideal joints at interface locations, and the inclusion of component flexibility, is developed: both are necessary tasks if one wants to capture dynamic effects which arise in lightweight, high-speed applications.

With regard to the first topic, both a ball bearing model and a journal bearing model are implemented, in order to properly capture the dynamic effects of the main connections in the system: angular contact ball bearings are modelled according to a five-DOF nonlinear scheme in order to grasp the crankshaft main bearings behaviour, while an impedance-based hydrodynamic bearing model is implemented providing an enhanced operation prediction at the conrod big end locations.

Concerning the second matter, flexible models of the crankshaft and the connecting rod are produced. The well-established Craig-Bampton reduction technique is adopted as a general framework to obtain reduced model representations which are suitable for the subsequent multibody analyses. A particular component mode selection procedure is implemented, based on the concept of Effective Interface Mass, allowing an assessment of the accuracy of the reduced models prior to the nonlinear simulation phase. In addition, a procedure to alleviate the effects of modal truncation, based on the Modal Truncation Augmentation approach, is developed. In order to assess the performances of the proposed modal reduction schemes, numerical tests are performed onto the crankshaft and the conrod models in both frequency and modal domains.

A multibody model of the cranktrain is eventually assembled and simulated using a commercial software. Numerical results are presented, demonstrating the effectiveness of the implemented flexible model reduction techniques. The advantages over the conventional frequency-based truncation approach are discussed.

Contents

Chapter 1

Introduction

Modern powertrain design is facing increasingly strict requirements in terms of emissions, fuel consumption, noise and vibration levels. In recent years, this trend is extending towards the motorcycle industry, in which competitive design focused on achieving a high power-to-weight ratio calls for optimized engine components. This in turn requires the adoption of a multidisciplinary approach early in the conception phase, and the use of advanced simulation tools which help the analysts in gaining a deeper insight into the physical phenomena associated with the engine operation.

1.1 Cranktrain dynamics simulation

Concerning structural design aspects, modern analysis techniques involve the adoption of *multibody* simulation tools, which allow an accurate prediction of loads acting on the system components at operational speed, thus improving the subsequent stress and fatigue life analysis.

Several approaches are described in literature dealing with multibody modelling of internal combustion engine powertrains. Some papers deal with the construction of fully coupled cranktrain models through the use of commercial multibody dynamics codes, which provide a general modelling platform for mechanical systems, see e.g. [10, 12, 25, 26, 28, 66, 71, 72, 82, 83]: the system equations of motion are in this case automatically generated by the software kernel, and solved by means of some standard integration scheme. As an alternative, some studies describe the development of specialized modelling codes, see e.g. [14, 24, 27, 47, 58, 61, 68, 69, 70]: the system equations of motion are retrieved analytically and implemented in specific computational algorithms.

In this work, the former approach has been followed to investigate the elastodynamic behaviour of the cranktrain of a Ducati L-twin, four strokes engine, having a displacement of 1.2 litres, capable of delivering 180 horsepower.

In the context of multibody modelling, the definition of a system made up of rigid links connected to each other via kinematic joints typically represents the first step in the process; in fact, commercial multibody software platforms offer both geometry and joint libraries, permitting the analyst to set up a basic dynamic model with little time and effort. Clearly, this modelling approach is affected by some important limitations: first of all, the adoption of rigid bodies in combination with kinematic joints prevents some interface loads to be evaluated whenever the mechanism under study exhibits some static indeterminacy; furthermore, any dynamic amplification effect, which might significantly affect the actual loads, is evidently lost. These shortcomings can be eliminated by embracing a refined modelling methodology, based upon the introduction of non-ideal joints at interface locations, and the inclusion of component flexibility.

In this study both a ball bearing model and a journal bearing model have been implemented, starting from available literature descriptions, in order to properly capture the dynamic effects of the main connections in the system under study: in fact, the crankshaft is supported by four main journals, three of which equipped with ball bearings, the other one with a bush bearing, while the two connecting rods act on the crankpin through hydrodynamically lubricated journal bearings.

Several ball bearing models are found in literature, mainly referring to different approaches: a numerical approach, see e.g. [2, 13, 20, 48, 51], for which the discrete ball-race loads are summed numerically, and an analytical approach, cf. [41, 49], for which the summation of ball-race loads is replaced by an integration. While the former is considered superior in terms of accuracy, the latter is often more accessible for designers who want to include bearing models in their application codes in order to predict bearing performances without having to perform heavy numerical calculations.

The angular contact ball bearing model proposed in [41] is adopted here: the model provides a nonlinear definition of loads and moments acting on the inner ring taking into account five relative race displacements, i.e. three translations and two tilting angles; a full coupling between those is considered.

Concerning journal bearings, their importance in rotating and reciprocating machine applications is proved by the huge number of papers published on this subject. Numerical methods, especially the Finite Element Method (FEM), are widely used to analyse journal bearings including oil feed holes and grooves, and geometry effects like taper and misalignment; such methods, see e.g. [6,

9, 27, 36, 56, 57], are probably the most accurate and versatile, but they tend to be expensive and not always practical. Often, designers use less expensive, approximate analytical methods, cf. [7, 8, 15, 35, 46]; amongst those, the mobility method and its dual counterpart, the impedance method, are the most popular.

The impedance description as proposed in [15] for plain, circumferentially-symmetric fluid journal bearings is taken here as reference. Such a model provides a dynamic nonlinear definition of the bearing reaction force as a function of the journal motion, being particularly suited for transient simulation work. The adopted formulation is a combination of the two asymptotic short bearing and long bearing solutions [65], and performs well for general finite-length bearings at both large and small eccentricity ratios; furthermore, since the pressure distributions are not calculated, the method permits very efficient computation.

Specific computational routines have been produced concerning both bearing types, and embedded into the adopted multibody solver.

As mentioned, another key aspect in obtaining realistic results from multibody dynamic simulations is the inclusion of component flexibility: this is a necessary task if one wants to capture dynamic effects which arise in lightweight, high-speed applications.

Different techniques exist to incorporate body flexibility in multibody models [75, 80]; among those, the Floating Frame of Reference formulation is certainly the most widely used, and is currently implemented in several commercial multibody dynamics software packages. The assumption here is that the deformation of the generic flexible body keeps small with respect to a body local reference frame, which in turn undergoes large, nonlinear motion relative to an inertial global reference frame; such hypothesis of linear body flexibility allows linear *model reduction* techniques to be exploited to reduce the number of coordinates required to describe the component deformation, thus reducing the needed computational effort.

In particular, Component Mode Synthesis (CMS) techniques can be employed to describe body deformation as a linear combination of a number of mode shapes: this task is accomplished by means of some coordinate transformation, from physical to modal domain, which can include different kind of modes [16, 17], i.e. eigenmodes, constraint modes, attachment modes, etc. With this respect, several schemes were proposed by a number of authors in the past, see e.g. [18, 42, 45, 50, 62, 73, 74]; due to a simple, straightforward formulation of the reduction process, combined with good overall performance, the Craig-Bampton (CB) approach [18] has gained increasing popularity among the structural dynamics community, and is nowadays the most widely used reduction method for flexible multibody dynamics applications.

Such method has been employed here as a general framework to obtain reduced model representations for both the crankshaft and the connecting rods involved in the cranktrain under study.

1.2 Focus of the thesis

Model reduction through CMS implies that the full set of physical coordinates is reduced to a smaller set of generalized coordinates, giving rise to a *modal selection* problem. Clearly, the two most important aspects of such a problem are model order and model accuracy: an optimal reduction would result in the minimal set of component modes which ensures acceptable accuracy in the simulation results. Despite modal selection being an important concern in CMS techniques, and CB in particular, not many papers exist on the subject, and the standard practice consists in using some frequency-based criterion to select mode shapes to retain in the reduced representation of a component.

In the present work, a different approach is proposed: the mode selection procedure is carried out in accordance with a modal ordering scheme based upon Effective Interface Mass (EIM), which determines the contribution of each mode shape to the dynamic loads at the interface, providing a rigorous measure of modal dynamic importance. The EIM approach was introduced in the mid-nineties [54, 55], with main focus on dynamic substructuring and control-structure interaction applications; an extension towards multibody dynamics is presented here.

The dual aspect of modal selection is *modal truncation*: modes which are not retained in the reduced representation of a component are simply discarded. This might lead to inaccurate representation of the applied loading, both concerning its time dependency and its spatial dependency [21]: while the first concern is usually addressed by including in the reduced representation a number of modes spanning a multiple of the frequency range of interest, the latter is often ignored. Some techniques were proposed in the past to tackle this problem, being the Mode Acceleration method [19] the most popular one: such method, however, acts only at the physical response recovery stage, and does not provide any enhancement to the modal representation of the component.

In the present study, the Modal Truncation Augmentation (MTA) technique [21, 23, 31] is adopted to augment the CB reduction transformation matrix with a set of pseudo-eigenvectors, which provide a quasi-static correction for low-frequency excitation, as well as a dynamic correction for high-frequency excitation. Unlike Mode Acceleration, the enhancement impacts the dynamic characteristics of the reduced flexible component, thus resulting attractive for

multibody dynamics applications.

Both the EIM and the MTA techniques have been implemented as specific routines within the adopted FE commercial code, and used to obtain reduced models of both the crankshaft and the connecting rod employed for the subsequent multibody dynamic simulations.

1.3 Outline of the dissertation

This thesis is organized as follows.

Chapter 1 introduces the thesis by presenting the subject, highlighting the main focus and clarifying the organization of the text.

Chapter 2 presents the ball bearing and journal bearing models employed for simulation purposes, describing the theoretical developments of the models and providing some details about their specific implementation in the multibody dynamics software.

Chapter 3 discusses the component model reduction techniques which are used to obtain reduced flexible component models of the crankshaft and the connecting rod. The theoretical developments of the CB, EIM and MTA methods are provided, along with the details about their practical implementation in the FE code. The assessment of the reduced models through numerical tests performed onto the single components is eventually described.

Chapter 4 presents the development of the multibody model of the engine cranktrain. A brief theoretical overview about the Floating Frame of Reference formulation in flexible multibody dynamics is provided first. The multibody model assembly is then described, and the specific simulation results are discussed demonstrating the benefits of the adopted model reduction techniques.

Chapter 5 provides some concluding remarks and suggestions for future research.

Chapter 2

Bearing modelling

The use of ideal joints, i.e. kinematic constraints, is a standard practice in multi-body dynamics simulation, especially when commercial software platforms are employed for the purpose: these usually provide ready-to-use joint libraries from which the user selects the most suitable ones for his specific application, allowing for an express model deployment. Whenever accuracy is a major concern, however, this modelling approach is somewhat restrictive, and the use of non-ideal joints, i.e. force constraints, should be taken into consideration for the main connections in the system. Clearly this requires the additional effort of implementing joint models, which can be an expensive activity depending on the complexity of the involved theoretical background; furthermore, dynamic simulations including such kind of models can be costly, thus a cost-benefit analysis should always be made to choose adequate modelling strategies.

In this study both a ball bearing model and a journal bearing model have been implemented, starting from available literature descriptions, in order to properly capture the dynamic effects of the main connections in the cranktrain under study, cf. Chapter 4: in fact, the crankshaft is supported by four main journals, three of which equipped with ball bearings, the other one with a bush bearing, while the two connecting rods act on the crankpin through hydrodynamically lubricated journal bearings.

2.1 Ball bearing modelling

Several ball bearing models are found in literature, mainly referring to different approaches: a numerical approach, see e.g. [2, 13, 20, 48, 51], for which the discrete ball-race loads are summed numerically, and an analytical approach, cf. [41, 49], for which the summation of ball-race loads is replaced by an integration.

While the former is considered superior in terms of accuracy, the latter is often more accessible for designers who want to include bearing models in their application codes in order to predict bearing performances without having to perform heavy numerical calculations. The method proposed by Hernot et al. [41] is adopted here, this consisting actually in a matrix formulation of Houpert's *uniform* analytical approach [49], based on a first-order development of the ball-race Hertzian deformation.

Hertzian theory refers to the localized stresses that develop as the generic bearing ball comes in contact with the inner and outer raceways, slightly deforming under the imposed loads. Such deformations, assumed as elastic, are small compared to the dimensions of the contact area, which, in turn, is considered to be small with respect to the radii of curvature of the contacting bodies. No deformation of the inner and outer rings occur, except at the balls contact area: the stiffness of the whole bearing can be seen as a result of the stiffnesses associated to each ball-raceway contact. The load on each rolling element is assumed to be normal to the contacting surfaces, and the effects of surface shear stresses are neglected: the direction of such load identifies the *contact angle*, that defines the ability of angular contact bearings to support thrust loads and that does not usually exceed 40 degrees. Such angle is assumed as a constant throughout the mentioned references [41, 49]: any variation caused by imposed loads or centrifugal effects is ignored. In very high speed applications, though, such hypothesis becomes too strict, and models taking into account a contact angle variation must be employed [3, 59, 60].

The model presented here provides a nonlinear definition of loads and moments acting on the inner ring taking into account five relative race displacements, i.e. three translations and two tilting angles; a full coupling between those is considered. No radial clearances within the bearing, nor thermal effects are included; furthermore, the influence of the lubrication film is ignored.

2.1.1 Theoretical background

In order to clarify how the matrix formulation has been obtained in [41], the 2-degrees-of-freedom (2-DOF) ball bearing model is reviewed first. This model neglects any misalignment between inner and outer ring axes, which are thus considered to remain parallel under load. Such load, which can be expressed as a superposition of a thrust load F_a and a radial load F_r, determines a displacement of the inner ring with respect to the outer ring, which will be considered as fixed hereinafter. The variation of the distance between inner and outer ring can be approximated as a combination of an axial displacement, δ_a, and a displacement

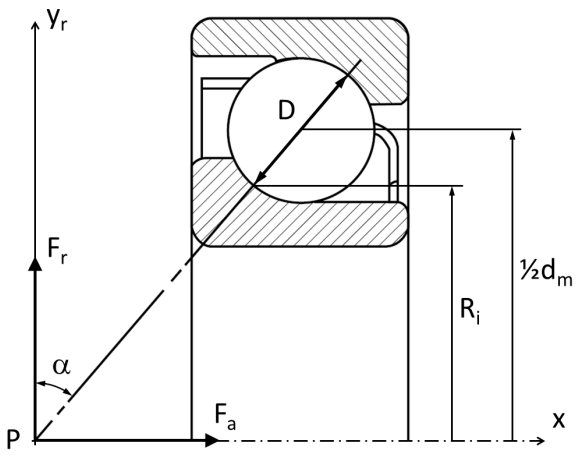

Figure 2.1 Angular contact ball bearing parameters, adapted from [41]

along the radial load direction, δ_r, as:

$$d_\psi \approx \delta_a \sin\alpha + \delta_r \cos\alpha \cos\psi \tag{2.1}$$

where α is the bearing contact angle, see Figure 2.1, while ψ defines the generic rolling element angular position with respect to the radial load direction. This approximation ignores any contact angle variation, which is commonly acceptable for bearing analysis provided that both δ_a and δ_r are very small when compared to the overall bearing dimensions. The ball-race deflection is given by:

$$\delta_\psi = \max\left(0, d_\psi\right) \tag{2.2}$$

since compression only occurs for positive values of d_ψ.

The ball-raceway contact load Q is estimated using the traditional Hertzian load-deflection relationship:

$$Q = k\delta^n \tag{2.3}$$

where k is a factor depending on the contact geometry and the material elastic constants. The exponent n only depends upon the contact geometry: for ball bearings, where point contact can be assumed, $n = 3/2$. The contact load at any angular position is then given by:

$$Q_\psi = k\left[\max\left(0, d_\psi\right)\right]^n \tag{2.4}$$

which can be rearranged as:

$$\mathrm{Q}_\psi = k d_\psi \left[\max\left(0, d_\psi\right)\right]^{n-1} \tag{2.5}$$

This simple step is crucial towards the definition of a matrix formulation of the problem.

For static equilibrium to exist, the summation of rolling element forces in each direction must equal the applied load in that direction:

$$\mathrm{F}_a = \sum_{\psi=0}^{2\pi} \mathrm{Q}_\psi \sin\alpha \tag{2.6a}$$

$$\mathrm{F}_r = \sum_{\psi=0}^{2\pi} \mathrm{Q}_\psi \cos\psi \cos\alpha \tag{2.6b}$$

If equation (2.5) is used instead of (2.4), then the previous can be rearranged in matrix format as:

$$\begin{Bmatrix} \mathrm{F}_a \\ \mathrm{F}_r \end{Bmatrix} = \begin{bmatrix} \mathrm{K}_{11} & \mathrm{K}_{12} \\ \mathrm{K}_{12} & \mathrm{K}_{22} \end{bmatrix} \begin{Bmatrix} \delta_a \\ \delta_r \end{Bmatrix} \tag{2.7}$$

with:

$$\mathrm{K}_{11} = \sum_{\psi=0}^{2\pi} k \left[\max\left(0, d_\psi\right)\right]^{n-1} \sin^2\alpha \tag{2.8a}$$

$$\mathrm{K}_{12} = \sum_{\psi=0}^{2\pi} k \left[\max\left(0, d_\psi\right)\right]^{n-1} \cos\psi \sin\alpha \cos\alpha \tag{2.8b}$$

$$\mathrm{K}_{22} = \sum_{\psi=0}^{2\pi} k \left[\max\left(0, d_\psi\right)\right]^{n-1} \cos^2\psi \cos^2\alpha \tag{2.8c}$$

Since the angular position of the balls changes during normal operation, the stiffness of the bearing also changes continuously in real-life applications. In order to avoid taking into account the angular position of each ball, which would result in an increased model complexity, it is possible to use the integral form of Sjoväll [39, 77]: this prevents summing the discrete rolling element loads, by making the assumption that the angular position of the rolling elements with respect to each other is always maintained due to a rigid, ideal cage. The expressions of the bearing stiffness matrix elements in (2.8) may then be rewritten as:

$$\mathrm{K}_{11} = \mathrm{K}_\varepsilon \sin^2\alpha \, J_{aa}\left(\varepsilon\right) \tag{2.9a}$$

$$K_{12} = K_\varepsilon \sin\alpha \cos\alpha \, J_{ra}(\varepsilon) \tag{2.9b}$$

$$K_{22} = K_\varepsilon \cos^2\alpha \, J_{rr}(\varepsilon) \tag{2.9c}$$

being K_ε a stiffness dimensional factor:

$$K_\varepsilon = Zk\left(\delta_a \sin\alpha + \delta_r \cos\alpha\right)^{n-1} \tag{2.10}$$

Here, Z is the number of rolling elements. The integrals in (2.9) can be expressed as:

$$J_{aa}(\varepsilon) = \frac{1}{2\pi}\int_0^{2\pi} H(\varepsilon)\, d\psi \tag{2.11a}$$

$$J_{ra}(\varepsilon) = \frac{1}{2\pi}\int_0^{2\pi} H(\varepsilon)\cos\psi d\psi \tag{2.11b}$$

$$J_{rr}(\varepsilon) = \frac{1}{2\pi}\int_0^{2\pi} H(\varepsilon)\cos^2\psi d\psi \tag{2.11c}$$

where:

$$H(\varepsilon) = \left[\max\left(0, 1 - \frac{1-\cos\psi}{2\varepsilon}\right)\right]^{n-1} \tag{2.12}$$

The load distribution factor ε is defined as:

$$\varepsilon = \frac{1}{2}\left(1 + \frac{\delta_a \tan\alpha}{\delta_r}\right) \tag{2.13}$$

The integrals in (2.11) may be evaluated numerically for any value of ε; Hernot proposed approximate equations which precisely fit these numerical results [41], and which allow an easier implementation.

Let's now extend the explained concepts to the 5-DOF model. In this case the distance variation between inner and outer race has been calculated by Houpert [49] by taking into account five relative displacements, i.e. three translations and two tilting angles. The exact relationship is rather cumbersome, but Houpert used a first-order development to obtain a simplified relationship:

$$d_\varphi \approx \delta_x \sin\alpha + \Delta_y \cos\alpha \cos\varphi + \Delta_z \cos\alpha \sin\varphi \tag{2.14}$$

where Δ_y, Δ_z are the equivalent radial displacement components along the global y and z axes:

$$\Delta_y = \delta_y - \delta_{\theta z} R_i \tan\alpha \tag{2.15a}$$

$$\Delta_z = \delta_z + \delta_{\theta y} R_i \tan\alpha \tag{2.15b}$$

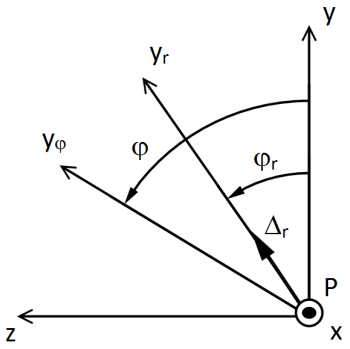

Figure 2.2 Coordinate system used for the 5-DOF model, adapted from [41]

Here, R_i is the mean inner race radius[1], while φ is the generic rolling element angular position with respect to the y axis, see Figure 2.2. The equivalent radial displacement can be expressed as:

$$\Delta_r = \sqrt{\Delta_y^2 + \Delta_z^2} \tag{2.16}$$

so that (2.14) can be rewritten:

$$d_\varphi \approx \delta_x \sin\alpha + \Delta_r \cos\alpha \cos\left(\varphi - \varphi_r\right) \tag{2.17}$$

In the previous, φ_r represents the direction of the maximum radial displacement and is defined as:

$$\varphi_r = \begin{cases} \arctan\left(\Delta_z/\Delta_y\right), & \Delta_y \geq 0 \\ \arctan\left(\Delta_z/\Delta_y\right) + \pi, & \Delta_y < 0 \end{cases} \tag{2.18}$$

Note that there is a complete analogy between (2.17) and (2.1).

The static equilibrium between rolling element forces and applied loads now holds:

$$F_x = \sum_{\varphi=0}^{2\pi} Q_\varphi \sin\alpha \tag{2.19a}$$

$$F_y = \sum_{\varphi=0}^{2\pi} Q_\varphi \cos\varphi \cos\alpha \tag{2.19b}$$

[1]Houpert derived expression (2.14) by using the mean inner race radius R_i, see Figure 2.1, while Hernot uses the radius of the intersection between the contact cone and the inner raceway median plane, R_I, throughout [41]. The former has been taken here as reference, but it seems reasonable that both might be used without substantial differences, due to close numerical values.

$$F_z = \sum_{\varphi=0}^{2\pi} Q_\varphi \sin\varphi \cos\alpha \tag{2.19c}$$

$$M_y = F_z R_i \tan\alpha \tag{2.19d}$$

$$M_z = -F_y R_i \tan\alpha \tag{2.19e}$$

where the ball-raceway contact load distribution Q_φ has been introduced. By expressing it in a similar fashion to that in (2.5) allows to rearrange (2.19) in matrix format, in complete analogy with the described two-DOF bearing model. The load-displacement relationship becomes:

$$\begin{Bmatrix} F_x \\ F_y \\ F_z \\ M_y \\ M_z \end{Bmatrix} = \begin{bmatrix} K_{11} & K_{12} & K_{13} & K_{14} & K_{15} \\ & K_{22} & K_{23} & K_{24} & K_{25} \\ & & K_{33} & K_{34} & K_{35} \\ & \text{Sym} & & K_{44} & K_{45} \\ & & & & K_{55} \end{bmatrix} \begin{Bmatrix} \delta_x \\ \delta_y \\ \delta_z \\ \delta_{\theta y} \\ \delta_{\theta z} \end{Bmatrix} \tag{2.20}$$

with:

$$K_{11} = K_\varepsilon \sin^2\alpha \, J_{aa}(\varepsilon) \tag{2.21a}$$

$$K_{12} = K_\varepsilon \sin\alpha \cos\alpha \cos\varphi_r \, J_{ra}(\varepsilon) \tag{2.21b}$$

$$K_{13} = K_\varepsilon \sin\alpha \cos\alpha \sin\varphi_r \, J_{ra}(\varepsilon) \tag{2.21c}$$

$$K_{14} = K_{13} R_i \tan\alpha \tag{2.21d}$$

$$K_{15} = -K_{12} R_i \tan\alpha \tag{2.21e}$$

$$K_{22} = K_\varepsilon \cos^2\alpha \left[\sin^2\varphi_r \, J_{aa}(\varepsilon) + \cos 2\varphi_r \, J_{rr}(\varepsilon)\right] \tag{2.21f}$$

$$K_{23} = K_\varepsilon \cos^2\alpha \sin 2\varphi_r \left[J_{rr}(\varepsilon) - \frac{1}{2} J_{aa}(\varepsilon)\right] \tag{2.21g}$$

$$K_{24} = K_{23} R_i \tan\alpha \tag{2.21h}$$

$$K_{25} = -K_{22} R_i \tan\alpha \tag{2.21i}$$

$$K_{33} = K_\varepsilon \cos^2\alpha \left[\cos^2\varphi_r \, J_{aa}(\varepsilon) - \cos 2\varphi_r \, J_{rr}(\varepsilon)\right] \tag{2.21j}$$

$$K_{34} = K_{33} R_i \tan\alpha \tag{2.21k}$$

$$K_{35} = -K_{23} R_i \tan\alpha \tag{2.21l}$$

$$K_{44} = K_{33} R_i^2 \tan^2\alpha \tag{2.21m}$$

$$K_{45} = -K_{23} R_i^2 \tan^2\alpha \tag{2.21n}$$

$$K_{55} = K_{22} R_i^2 \tan^2\alpha \tag{2.21o}$$

The integral function expressions in (2.11) are still valid, as well as the stiffness dimensional factor in (2.10) and the load distribution factor in (2.13), provided

that the axial and radial displacements δ_a and δ_r are now replaced by the corresponding variables δ_x and Δ_r.

2.1.2 Model implementation

The described 5-DOF bearing model has been implemented in ADAMS by using the `field` element, which computes forces and moments acting between any two `markers`, i.e. reference frames, based upon their relative displacements and velocities. Full 6-by-6 stiffness and damping matrices can be defined for the purpose; preloads are allowed, as well.

In the present case, dealing with a nonlinear model, the mentioned matrices need to be computed by means of a `fiesub` user-written subroutine; this has been coded in Fortran, and its basic functioning is briefly depicted in the following.

Model parameters are the angular bearing contact angle α, the mean inner race radius R_i, obtained from pure geometrical considerations, the number of rolling elements Z, as from the bearing specifications, and the load-deflection factor k, which can be approximated as[2]:

$$k \approx 10^5 D^{1/2} \tag{2.22}$$

being D the rated ball diameter. The presented formulation has been enriched by adding damping, so that (2.20) becomes, using compact notation:

$$\mathbf{F} = \mathbf{K}\left(\boldsymbol{\delta} + c\dot{\boldsymbol{\delta}}\right) \tag{2.23}$$

resulting in a proportional damping formulation; the damping constant c is a user-defined parameter.

Model inputs are the relative displacements and velocities of the `markers` attached to the inner and outer rings[3], $\boldsymbol{\delta}$ and $\dot{\boldsymbol{\delta}}$, evaluated at each simulation timestep, from which the equivalent radial displacement Δ_r and its direction φ_r are readily computed, along with the load distribution factor ε. The stiffness dimensional factor and the load distribution integrals are then computed according to (2.10) and (2.11), respectively; attention has been paid to the definition of

[2] Such approximation holds true, according to [41], for 7200 and 7300 angular contact ball bearing series; for other bearing types information should be gathered from available literature, or directly from the manufacturer.

[3] The `field` element only allows the angle about the z axis to become arbitrarily large during a simulation, the others having to remain smaller than 10 degrees: to keep the original formulation as in [41], an input and output "switch" has been implemented, mapping the ADAMS model coordinates to the reference frame used in the bearing model definition, cf. Figure 2.2. Obviously, the `markers` in the model have to be oriented accordingly, i.e. z along the axial direction and x, y in the radial ones.

those cases which might give rise to numerical issues, e.g. $\Delta_r = 0$ or $\varepsilon \leq 0$, for which the proper values are simply assigned to the aforementioned variables. The stiffness matrix elements are eventually computed according to (2.21), and use to calculate the force vector $\mathbf{F}$. In addition to the force vector components, the `fiesub` element requires as output arguments the derivatives of those with respect to both the displacement variables in $\boldsymbol{\delta}$ and the velocity variables in $\dot{\boldsymbol{\delta}}$; these partial derivatives have been evaluated analytically with the aid of a symbolic math manipulation software, and included in the Fortran code.

2.2 Journal bearing modelling

Concerning journal bearings, their importance in rotating and reciprocating machine applications is proved by the huge number of papers published on this subject. Numerical methods, especially the Finite Element Method, are widely used to analyse journal bearings including oil feed holes and grooves, and geometry effects like taper and misalignment; such methods, see e.g. [6, 9, 27, 36, 56, 57], are probably the most accurate and versatile, but they tend to be expensive and not always practical. Often, designers use less expensive, approximate analytical methods, cf. [7, 8, 15, 35, 46]; amongst those, the *mobility* method and its dual counterpart, the *impedance* method, are the most popular.

The concept of mobility was introduced by Booker [7] to address the problem of determining the motion of the bearing journal given the applied force: such approach is applicable for bearings for which the external load is known and dominant with respect to the inertia effects of the rotor, and found its preferred field of application in the analysis of journal bearings employed in reciprocating machines, such as internal combustion engines. The dual concept of impedance was later introduced by Childs et al. [15] to solve the problem of determining the bearing reaction force given the position and velocity of the journal: this approach is more suited to those problems where the stiffness and inertia properties of the rotor must be accounted for, resulting preferred in rotordynamic analysis.

The impedance description as proposed in [15] for plain, circumferentially-symmetric fluid journal bearings is taken here as reference. Such a model provides a dynamic nonlinear definition of the bearing reaction force as a function of the journal motion, being particularly suited for transient simulation work. The adopted formulation is a combination of the two asymptotic short and long solutions [65], and performs well for general finite-length bearings at both large and small eccentricity ratios; furthermore, since the pressure distributions are not calculated, the method permits very efficient computation.

2.2.1 Theoretical background

This section briefly presents the theoretical development of the impedance method [15].

The hydrodynamic lubrication theory is based on the well-known Reynolds equation. If variations of viscosity are ignored, and if the lubricant is assumed as incompressible, such equation simplifies to:

$$\frac{\partial}{\partial\theta}\left(h^3\frac{\partial p}{\partial\theta}\right)+\mathrm{R}^2\frac{\partial}{\partial z}\left(h^3\frac{\partial p}{\partial z}\right)=\frac{12\mu\mathrm{R}^2}{\mathrm{C}^2}\left[\dot{\varepsilon}\cos\theta+\varepsilon\left(\dot{\beta}-\overline{\omega}\right)\sin\theta\right] \quad (2.24)$$

where θ and z are the angular and the axial cylindrical coordinates, respectively. R and C are the rated bearing radius and radial clearance, respectively, ε is the eccentricity ratio, i.e. the journal center eccentricity e normalized to the radial clearance, while h is the normalized film thickness defined as:

$$h=1+\varepsilon\cos\theta \quad (2.25)$$

The angle β defines the direction of eccentricity, see Figure 2.3, while $\overline{\omega}$ is the average angular velocity of journal and sleeve with respect to a grounded, stationary frame:

$$\overline{\omega}=\frac{1}{2}\left(\omega_j+\omega_s\right) \quad (2.26)$$

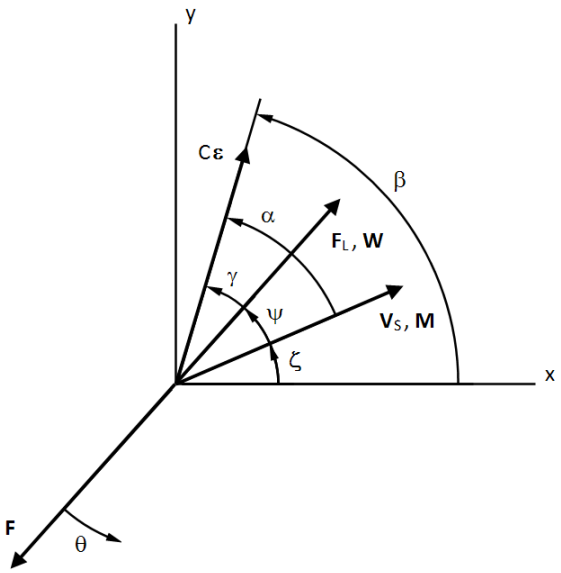

Figure 2.3 Kinematic variables for impedance and mobility definitions, adapted from [15]

Finally, μ and p are the fluid viscosity and film pressure, respectively.

Considering now an observer pinned to the sleeve center and rotating at the angular velocity $\overline{\boldsymbol{\omega}}$, the actual journal center velocity $\dot{\boldsymbol{e}}$ and the velocity $\mathbf{V}_s$ apparent to the observer are related by the simple kinematic expression:

$$\mathbf{V}_s = \dot{\boldsymbol{e}} - \overline{\boldsymbol{\omega}} \times \boldsymbol{e} \tag{2.27}$$

where the vector notation has been introduced; the symbol × indicates cross product. Since the average angular velocity of journal and sleeve apparent to the observer would vanish identically, the generation of pressure would seem to be related solely to the apparent velocity $\mathbf{V}_s$ in exactly the same way as for a non-rotating journal: such velocity $\mathbf{V}_s$ is henceforth called *effective squeeze velocity*, and the corresponding pressure equals the pressure generated by the combined effect of the actual *squeeze* velocity $\dot{\boldsymbol{e}}$ and the *wedge* effect due to the rotation of journal and sleeve, cf. Figure 2.4.

The Reynolds equation (2.24) might be rewritten in terms of the effective squeeze velocity as:

$$\frac{\partial}{\partial\theta}\left(h^3\frac{\partial p}{\partial\theta}\right) + \mathrm{R}^2\frac{\partial}{\partial z}\left(h^3\frac{\partial p}{\partial z}\right) = \frac{12\mu\mathrm{V}_s\mathrm{R}^2}{\mathrm{C}^3}\cos(\alpha+\theta) \tag{2.28}$$

where α represents the attitude angle of the eccentricity vector with respect to the effective squeeze velocity vector, see Figure 2.3. An analytical solution of (2.28) for arbitrary geometry cylindrical bearings is not feasible. Most frequently, numerical methods are employed to solve such equation and to obtain the performance characteristics of bearing configurations of particular interest. However, approximate analytical solutions can be obtained by a direct integration of (2.28) under different assumptions.

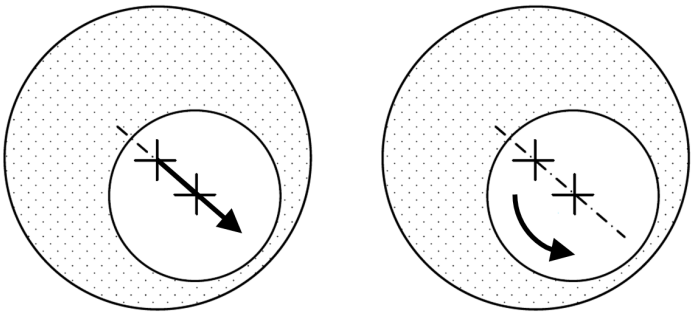

Figure 2.4 Squeeze (left) and wedge (right) fluid film effects, adapted from [30]

The Ocvirk solution is obtained by ignoring the pressure variations in the circumferential direction, and solving for $p(\theta, z)$ with the axial boundary condition of zero relative pressure at both bearing ends. Integrating axially yields the following average axial film pressure:

$$p(\theta) = -\frac{\mu V_s L^2}{h^3 C^3} \cos(\alpha + \theta) \tag{2.29}$$

being L the bearing axial length. The pressure is seen to be positive between the angles:

$$\theta_1 = \frac{\pi}{2} - \alpha \tag{2.30a}$$

$$\theta_2 = \theta_1 + \pi \tag{2.30b}$$

The assumption is made that the pressure gradient along θ is negligible with respect to that along z, which is equivalent to consider the bearing as infinitely short: the model is also referred to as *short bearing solution*, and is generally applicable for narrow bearings characterized by slenderness ratios, i.e. length-to-diameter, up to 0.5.

The Sommerfeld solution is obtained by neglecting the pressure variations in the axial direction, and solving for $p(\theta)$ with the boundary condition of 2π-periodicity with respect to θ and the requirement that the positive pressure sector extends over π radians, providing:

$$p(\theta) = -\frac{6\mu V_s R^2}{h^2 C^3} (\cos\alpha \cos\theta - b \sin\alpha \sin\theta)(2 + \varepsilon \cos\theta) \tag{2.31}$$

where

$$b = \frac{2}{2 + \varepsilon^2} \tag{2.32}$$

The positive pressure sector lies between the angles defined by:

$$\tan\theta_1 = \frac{1}{b \tan\alpha} \tag{2.33a}$$

$$\theta_2 = \theta_1 + \pi \tag{2.33b}$$

The assumption here is that the fluid pressure is constant along z and that leakage at bearing ends is negligible, which is equivalent to consider the bearing as infinitely long: the model is also referred to as *long bearing solution*, and applies for slenderness ratios greater than 2. An extension is provided by the Warner-Sommerfeld model, which is obtained by multiplying the Sommerfeld pressure

distribution by an end-leakage function varying only in the axial direction: the effects of both circumferential and axial pressure variations are considered, generally leading to more satisfactory results.

These asymptotic solutions have demonstrated a restricted range of application. For short bearings the Ocvirk solution has proven to be accurate in defining the direction of the bearing reaction, but predicts an erroneously large magnitude especially at large eccentricity ratios. The Sommerfeld model, as well as the Warner-Sommerfeld one, provides an improved definition of the bearing reaction magnitude for long bearings and high eccentricity ratios, but leads to inaccurate definition of its direction. The fact that their ranges of application do not coincide, allows the two models to be combined in such a way to obtain approximate solutions valid for general finite-length bearings at both small and large eccentricity ratios.

The forces acting on the journal can now be derived by integrating the obtained pressure distribution, e.g. (2.29, 2.31). This integration can be performed over the entire angular domain, leading to a *complete film* condition (*Sommerfeld*, or *full*, or 2π boundary condition) which justifies the presence of negative pressures within the fluid film, or only over the positive portion of the pressure distribution, leading to a *ruptured film* condition (*Gümbel*, or *half*, or π boundary condition) that prevents the development of negative pressures, see Figure 2.5: while the former neglects any phase effects, the latter provides an approximate model for cavitation and tends to be more generally applicable, leading to more realistic predictions. Actually, the π boundary condition is not correct as it violates the continuity of the flow across the cavitation boundary; other boundary condition sets which remove this inconsistency exist, see [79], but they tend to be much more sophisticated and cumbersome to implement in practice.

Integration of the pressure distribution yields the components of the force $\mathbf{F}$ acting from the fluid film on the journal. The impedance method permits

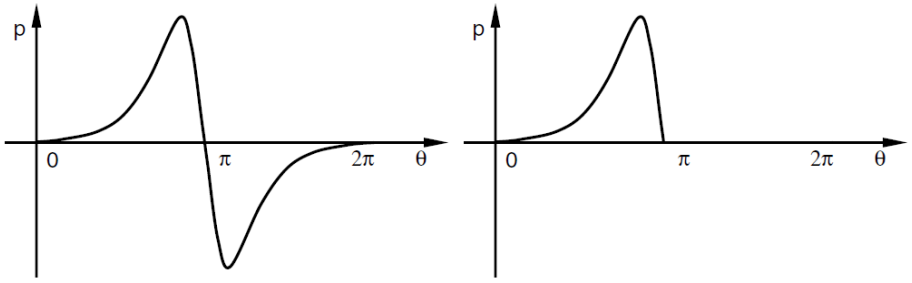

Figure 2.5 Complete (left) and ruptured (right) film conditions, adapted from [30]

to avoid such integration to compute the reaction force, removing the need of calculating the actual pressure distribution. The dimensionless impedance vector is defined by:

$$\mathbf{W} = \frac{(C/R)^3}{2\mu L}\frac{\mathbf{F}_L}{V_s} \tag{2.34}$$

where the vector $\mathbf{F}_L$ is the force applied from the journal to the fluid film, as opposed to the mentioned bearing reaction force, $\mathbf{F} = -\mathbf{F}_L$. For the sake of completeness, let's recall the mobility definition, as well:

$$\mathbf{M} = \frac{2\mu L}{(C/R)^3}\frac{\mathbf{V}_s}{F_L} \tag{2.35}$$

From the previous, impedance and mobility appear as the dimensionless counterparts of force and effective squeeze velocity, respectively; clearly, their magnitudes are reciprocal.

Several analytic mobility and impedance definitions were derived in the past, either analytically or by fitting numerical results, relating to either short, long or finite-length bearings under complete or ruptured fluid film conditions. By using these definitions, it is a simple matter to compute the journal velocity starting from the knowledge of applied force and eccentricity (mobility approach), or the bearing reaction force starting from journal position and velocity (impedance approach). Transformation from a mobility definition to an impedance definition can be carried out by the following relationships:

$$\tan\alpha = -\frac{M_\beta(\varepsilon,\gamma)}{M_\varepsilon(\varepsilon,\gamma)} \tag{2.36}$$

$$\tan\gamma = -\frac{W_\beta(\varepsilon,\alpha)}{W_\varepsilon(\varepsilon,\alpha)} \tag{2.37}$$

together with the reciprocity relation between mobility and impedance magnitudes. The angle γ defines the orientation of the eccentricity with respect to the impedance vector, see Figure 2.3.

In the present work, a π finite-lenght impedance description has been used [15], which is based on a mobility definition obtained as a weighted sum of the Ocvirk and Sommerfeld solutions, and which provides good approximation for all eccentricities and L/D ratios. The amplitude of the impedance vector is expressed as:

$$W = \left[0.15\left(E^2+G^2\right)^{1/2}(1-\varepsilon\cos\gamma)^{3/2}\right]^{-1} \tag{2.38}$$

where:

$$E = 1 + 2.12Q \tag{2.39a}$$

$$G = \frac{3\varepsilon \sin\gamma\,(1 + 3.6Q)}{4\,(1 - \varepsilon\cos\gamma)} \tag{2.39b}$$

$$Q = \frac{1 - \varepsilon\cos\gamma}{(L/D)^2} \tag{2.39c}$$

The angle γ can be obtained from the approximate solution:

$$\gamma \approx \left(1 - \frac{\varepsilon\cos\alpha}{\sqrt{1-\eta^2}}\right)\left(\arctan A + \arcsin\eta - \pi\frac{\eta}{2\,|\eta|}\right) - \arcsin\eta + \alpha \tag{2.40}$$

being:

$$\eta = \varepsilon\sin\alpha \tag{2.41a}$$

$$A = \frac{4\,(1 + 2.12B)\sqrt{1-\eta^2}}{3\eta\,(1 + 3.6B)} \tag{2.41b}$$

$$B = \frac{1 - \varepsilon^2}{(L/D)^2} \tag{2.41c}$$

Further details can be found in reference [15].

2.2.2 Model implementation

The described bearing model has been implemented in ADAMS by using the `gforce` element, which allows defining functions that represent the three translational and three rotational vector components of a generalized force vector acting between any two defined `markers`. Since, in the present case, the force expressions require a quite cumbersome definition, their computation is performed through a `gfosub` user-written subroutine; this has been coded in Fortran, and its basic functioning is briefly depicted in the following.

Model parameters are the bearing axial length L, the bearing diameter D and the radial clearance C, along with the dynamic viscosity of the lubricant μ evaluated at operating temperature (the algorithm neglects any thermal effects).

Inputs of the model are the displacements and velocities of the journal relative to the sleeve, evaluated at each integration step, as well as the angular velocities of both journal and sleeve, expressed with respect to a grounded, stationary reference `marker`.

The eccentricity vector in both magnitude ε and direction β is computed first, along with the average angular velocity $\overline{\omega}$. The effective squeeze velocity vector

is then computed according to (2.27), from which magnitude V_s and direction ζ are readily available. The angle defining the eccentricity vector with respect to the effective squeeze velocity vector can thus be evaluated according to Figure 2.3 as:

$$\alpha = \beta - \zeta \tag{2.42}$$

The angle γ defining the orientation of the eccentricity vector with respect to the impedance vector is now computed according to (2.40, 2.41), so that the impedance vector magnitude can now be derived as in (2.38, 2.39). The direction of the impedance vector with respect to the pure-squeeze-velocity vector is defined by the angle:

$$\psi = \alpha - \gamma \tag{2.43}$$

Now that the impedance vector is known in both magnitude and direction, the force on the journal can be computed according to (2.34).

It is worth mentioning that the described model cannot handle impacts between the journal and the bearing surface: if that circumstance occurs during the simulation run, the process is stopped and a warning message is issued. Such limitation could be overcome by implementing some dry contact model, along with a proper transition mechanism between that and the adopted hydrodynamic force model, see e.g. [29, 30].

Chapter 3

Component model reduction

In multibody systems, the inclusion of component flexibility is a necessary task if one wants to capture dynamic effects which arise in high-speed applications. According to the widespread *floating frame of reference* approach [76], the motion of each flexible body is subdivided into a reference motion, which can be described according to rigid multibody formalism, and a deformation. The Finite Element Method (FEM) is commonly used to describe such deformation; since small displacements and rotations are assumed to occur about the floating frame, linear methods borrowed from structural dynamics can be exploited, such as Component Mode Synthesis (CMS) techniques, in order to reduce the number of coordinates required to describe the component deformation. This task is accomplished by means of some coordinate transformation, from *physical* to *modal* domain, which involves the definition of proper component mode shapes; the reduction basis can include any sort of modes [16, 17], i.e. eigenmodes, constraint modes, attachment modes, etc., which were combined in several ways by a number of authors in the past [18, 42, 45, 50, 62, 73, 74]. Due to a simple, straightforward formulation of the reduction process, combined with good overall performance, the Craig-Bampton (CB) approach [18] has been widely used in structural dynamics, and is largely the most popular CMS method amongst the multibody dynamics community. This method is available in most commercial FE codes, and is generally considered as a standard for inclusion of component flexibility into multibody simulation work. Therefore, it has been employed as a general framework for component model reduction in the present study.

Until some kind of loading is applied, either transient or frequency response, it is very difficult to predict which modes will play a dominant role in the response of the structure. Model reduction, however, implies that the full set of physical coordinates is reduced to a smaller set of generalized coordinates, giving rise

to a *modal selection* problem. Clearly, the two most important aspects of such a problem are model order and model accuracy: an optimal reduction would result in the minimal set of component modes which ensures acceptable accuracy in the simulation results. Despite modal selection being an important concern in CMS techniques, and CB in particular, not many papers exist on the subject. Spanos et al. [78] developed a two-stage mode selection procedure derived from balanced realization theory [67]: the CB representation of the component is generated first, then brought to diagonal form and eventually further reduced via balancing; this is performed by using Gregory's [37] modal ranking criterion derived for lightly damped structures with well separated modal frequencies. In the present work, a selection procedure carried out in accordance with a modal ordering scheme based on Effective Interface Mass (EIM) is adopted. The EIM approach was introduced by Kammer et al. [54] in the mid-nineties, with main focus on dynamic substructuring and control-structure interaction applications; an extension towards multibody dynamics is proposed here.

The dual aspect of modal selection is *modal truncation*: component modes which are not retained in the reduced representation are simply discarded. This might lead to inaccurate representation of the applied loading, both concerning its time dependency and its spatial dependency [21]: while the first concern is usually addressed by including in the reduced representation a number of modes spanning a multiple of the frequency range of interest, the latter is often ignored. Some techniques were proposed in the past to tackle this problem, being the Mode Acceleration (MA) method [19] the most popular one: such method, however, acts only at the physical response recovery stage, and does not provide any enhancement to the modal representation of the component. In the present study, the Modal Truncation Augmentation (MTA) technique [21, 23, 31] is adopted to augment the CB reduction transformation matrix with a set of pseudo-eigenvectors, which provide a quasi-static correction for low-frequency excitation, as well as a dynamic correction for high-frequency excitation. Unlike MA, the enhancement impacts the dynamic characteristics of the reduced component, thus resulting attractive for multibody dynamics applications.

3.1 Theoretical background

3.1.1 The Craig-Bampton approach

This section briefly presents the theoretical development of the Craig-Bampton (CB) reduction method [18].

The equilibrium equation for the free-free, undamped structure holds:

$$\mathbf{M}\,\ddot{\mathbf{u}} + \mathbf{K}\,\mathbf{u} = \mathbf{f} \tag{3.1}$$

where $\mathbf{M}$ and $\mathbf{K}$ are the FE mass and stiffness matrices, respectively, and $\mathbf{f}$ is the external force vector. The physical degrees of freedom (DOFs) are partitioned into two complementary sets, the interface DOFs (subscript a, "active") and the interior DOFs (subscript o, "omitted"):

$$\begin{bmatrix} \mathbf{M}_{aa} & \mathbf{M}_{ao} \\ \mathbf{M}_{oa} & \mathbf{M}_{oo} \end{bmatrix} \begin{Bmatrix} \ddot{\mathbf{u}}_a \\ \ddot{\mathbf{u}}_o \end{Bmatrix} + \begin{bmatrix} \mathbf{K}_{aa} & \mathbf{K}_{ao} \\ \mathbf{K}_{oa} & \mathbf{K}_{oo} \end{bmatrix} \begin{Bmatrix} \mathbf{u}_a \\ \mathbf{u}_o \end{Bmatrix} = \begin{Bmatrix} \mathbf{f}_a \\ \mathbf{0} \end{Bmatrix} \tag{3.2}$$

Here, it has been assumed that external loads, i.e. external forces/torques, are applied only at the interface DOFs; clearly this requires a proper a-set definition. The following coordinate transformation is then introduced:

$$\begin{Bmatrix} \mathbf{u}_a \\ \mathbf{u}_o \end{Bmatrix} = \begin{bmatrix} \mathbf{I} & \mathbf{0} \\ \boldsymbol{\psi}_{oa} & \boldsymbol{\phi}_{oq} \end{bmatrix} \begin{Bmatrix} \mathbf{u}_a \\ \mathbf{q} \end{Bmatrix} \tag{3.3}$$

in which $\boldsymbol{\psi}_{oa}$ is a matrix of shapes obtained considering the lower partition of the static portion of (3.2) and solving for the o-set displacements:

$$\mathbf{u}_o = -\,\mathbf{K}_{oo}^{-1}\,\mathbf{K}_{oa}\,\mathbf{u}_a = \boldsymbol{\psi}_{oa}\,\mathbf{u}_a \tag{3.4}$$

while $\boldsymbol{\phi}_{oq}$ is a matrix of shape vectors satisfying the o-set eigenproblem:

$$\mathbf{K}_{oo}\,\boldsymbol{\phi}_{oq} = \mathbf{M}_{oo}\,\boldsymbol{\phi}_{oq}\,\boldsymbol{\Omega} \tag{3.5}$$

For the sake of compactness, we are now dropping the subscripts defining the dimensions of the matrices $\boldsymbol{\psi}_{oa}$ and $\boldsymbol{\phi}_{oq}$, which will be simply identified by $\boldsymbol{\psi}$ and $\boldsymbol{\phi}$, respectively, in the following.

The first N_a columns of the transformation matrix in (3.3) represent the static deformation shapes of the component when subjected to unit displacements at each of the a-set DOFs, the other being restrained; these are termed *constraint modes* in literature, and constitute the basis for the Guyan static condensation technique [38]. The last N_o columns are fixed-interface *normal modes*, i.e. eigenvectors, representing the dynamics of the substructure interior relative to the interface; the corresponding eigenvalues, i.e. the squared eigenfrequencies, are collected in the diagonal matrix $\boldsymbol{\Omega}$. As one might notice, the generalized coordinate vector comprises both physical displacements, $\mathbf{u}_a$, and modal displacements, $\mathbf{q}$; the fact that interface DOFs are retained in the reduced representation greatly facilitates component coupling, this being probably a major reason for the success of the CB method.

Introducing the transformation (3.3) into (3.2), and pre-multiplying by the transpose of the transformation matrix, the CB substructure representation is obtained:

$$\begin{bmatrix} \mathbf{M}_s & -\mathbf{P}^{\mathrm{T}} \\ -\mathbf{P} & \mathbf{I} \end{bmatrix} \begin{Bmatrix} \ddot{\mathbf{u}}_a \\ \ddot{\mathbf{q}} \end{Bmatrix} + \begin{bmatrix} \mathbf{K}_s & \mathbf{0} \\ \mathbf{0} & \boldsymbol{\Omega} \end{bmatrix} \begin{Bmatrix} \mathbf{u}_a \\ \mathbf{q} \end{Bmatrix} = \begin{Bmatrix} \mathbf{f}_a \\ \mathbf{0} \end{Bmatrix} \tag{3.6}$$

where the fixed-interface modes have been normalized with respect to the o-set mass matrix. The following positions hold:

$$\mathbf{M}_s = \mathbf{M}_{aa} + \mathbf{M}_{ao}\,\boldsymbol{\psi} + \boldsymbol{\psi}^{\mathrm{T}}\,\mathbf{M}_{oa} + \boldsymbol{\psi}^{\mathrm{T}}\,\mathbf{M}_{oo}\,\boldsymbol{\psi} \tag{3.7a}$$

$$\mathbf{K}_s = \mathbf{K}_{aa} + \mathbf{K}_{ao}\,\boldsymbol{\psi} \tag{3.7b}$$

$$\mathbf{P} = -\boldsymbol{\phi}^{\mathrm{T}}\left(\mathbf{M}_{oo}\,\boldsymbol{\psi} + \mathbf{M}_{oa}\right) \tag{3.7c}$$

being $\mathbf{M}_s$ and $\mathbf{K}_s$ the statically reduced mass and stiffness matrices, respectively; the matrix $\mathbf{P}$ is a modal participation factor matrix, containing the multiplication factors for the acceleration inputs at the interface DOFs governing the response of the fixed interface modal coordinates, cf. (3.8).

Most often, the dynamic behaviour of the FE component in a certain frequency range of interest can be captured using a much smaller number of generalized coordinates compared with the original number of physical coordinates: there lies model reduction. The selection of modes to include in the CB transformation matrix (3.3) plays a central role in the application of the method. The definition of the constraint modes directly comes from the coordinate partitioning process, which in turn is dependent upon the choice of interface DOFs; usually, these are selected as those where constraints or external loads are applied. On the other hand, the choice of fixed-interface normal modes to retain in the reduced representation is somewhat arbitrary, the standard practice consisting in truncating the solution at a certain cut-off frequency, defined as a multiple of the maximum frequency of interest. A different approach is used here, and will be reviewed in the next section.

3.1.2 The Effective Interface Mass concept

As mentioned, one of the key problems associated with CMS techniques is the determination of which mode shapes are dynamically important. A measure which is of great interest in structural dynamics is the contribution of each mode shape to the dynamic loads at the substructure interfaces: dynamically important modes contribute significantly to the interface loads and should then be retained in the reduced representation of the component.

The Effective Mass (EM) concept has been extensively used in structural dynamics to identify the important modes, based upon how much the mass associated with each mode contributes to the rigid body mass properties of the structure: it tends to spot global, low-frequency modes involving a substantial part of the structural mass. The Effective Interface Mass (EIM) constitutes a generalization of the EM: unlike EM, which determines the contribution of each mode shape to the resultant loads at the interface when the interior of the structure is given a rigid body displacement, the EIM determines modal contributions to interface loads under more general displacements of the interior, providing a more complete measure of dynamic importance.

Both techniques only work for constrained structures, and thus fixed-interface mode shapes; in the case where the interface DOFs are just sufficient to restrain rigid-body motion, i.e. statically determinate, the EIM reduces to the EM measure. A generalization of EM for free structures can be found in [52, 53].

Let's now provide a brief overview about the EIM concept, redirecting to [54, 55] for a more in-depth explanation. Recalling the CB equation of motion (3.6), its lower partition holds:

$$\ddot{\mathbf{q}} + \boldsymbol{\Omega}\,\mathbf{q} = \mathbf{P}\,\ddot{\mathbf{u}}_a \tag{3.8}$$

Considering a generic row-partition of (3.8), the time-domain response of the i-th fixed-interface mode to the a-set inputs can be computed as:

$$q_i = \omega_i^{-1}\,\mathbf{P}_i \int_0^t \ddot{\mathbf{u}}_a\,(\tau)\,\sin\left[\omega_i\,(t-\tau)\right]\,d\tau = \omega_i^{-1}\,\mathbf{P}_i\,\mathbf{v}_i \tag{3.9}$$

being ω_i the i-th mode eigenfrequency; the convolution integral has been denoted here as $\mathbf{v}_i$. The corresponding modal acceleration holds:

$$\ddot{q}_i = \omega_i^{-1}\,\mathbf{P}_i\,\ddot{\mathbf{v}}_i \tag{3.10}$$

Now considering the upper partition of (3.6),

$$\mathbf{M}_s\,\ddot{\mathbf{u}}_a + \mathbf{K}_s\,\mathbf{u}_a = \mathbf{f}_a + \mathbf{P}^{\mathrm{T}}\,\ddot{\mathbf{q}} \tag{3.11}$$

one recognizes the product $\mathbf{P}^{\mathrm{T}}\,\ddot{\mathbf{q}}$ as representing the portion of the load at the interface due to the response of the fixed-interface modes. Using (3.10), this can be expressed as:

$$\mathbf{P}^{\mathrm{T}}\,\ddot{\mathbf{q}} = \sum_{i=1}^{\mathrm{N}_o} \mathbf{P}_i^{\mathrm{T}}\,\ddot{q}_i = \sum_{i=1}^{\mathrm{N}_o} \omega_i^{-1}\,\mathbf{P}_i^{\mathrm{T}}\,\mathbf{P}_i\,\ddot{\mathbf{v}}_i \tag{3.12}$$

The norm of the matrix product $\mathbf{P}_i^{\mathrm{T}}\,\mathbf{P}_i$ gives thus a relative measure of the contribution of the i-th fixed-interface mode to the loads at the interface; summing *all* the contributions produces the so-called Reduced Interior Mass (RIM) matrix:

$$\overline{\mathbf{M}} = \sum_{i=1}^{\mathrm{N}_o} \overline{\mathbf{M}}_i = \sum_{i=1}^{\mathrm{N}_o} \mathbf{P}_i^{\mathrm{T}}\,\mathbf{P}_i = \mathbf{P}^{\mathrm{T}}\,\mathbf{P} \tag{3.13}$$

Substituting (3.7c) into (3.13) and bearing in mind that mass-normalization has been enforced, provides after some simple manipulation a closed form relation for the RIM matrix:

$$\overline{\mathbf{M}} = \mathbf{M}_{ao}\,\boldsymbol{\psi} + \boldsymbol{\psi}^{\mathrm{T}}\,\mathbf{M}_{oa} + \boldsymbol{\psi}^{\mathrm{T}}\,\mathbf{M}_{oo}\,\boldsymbol{\psi} + \mathbf{M}_{ao}\,\mathbf{M}_{oo}^{-1}\,\mathbf{M}_{oa} \tag{3.14}$$

It is worth noting that such expression can be computed based solely upon the partitioned FE mass and stiffness matrices, and is thus totally independent of any eigenvalue solution. By using some appropriate matrix norm, e.g. the trace norm, it can be used as an absolute reference with respect to which the dynamic importance of each mode shape can be computed.

The EIM value of the i-th fixed-interface mode is hence introduced:

$$\mathrm{E}_i = \frac{\mathrm{Tr}\left(\overline{\mathbf{M}}_i\right)}{\mathrm{Tr}\left(\overline{\mathbf{M}}\right)} \tag{3.15}$$

In order to avoid misleading results due to the usage of different units corresponding to the translational and rotational terms of the RIM matrix diagonal, it is suggested to always partition both $\mathbf{P}$ and $\overline{\mathbf{M}}$ according to the defined translational and rotational interface DOFs (a-set), and to apply (3.15) separately for each partition, then averaging the results to obtain a proper, single EIM value for each fixed-interface mode.

By summing the so-obtained values, a measure of dynamic completeness of a reduced representation in which N_k normal modes are retained is given by:

$$\tilde{\mathrm{E}}_k = \sum_{i=1}^{\mathrm{N}_k} \mathrm{E}_i \tag{3.16}$$

This provides a very useful guideline for mode selection: in fact, one can set a required level of dynamic completeness for the reduced model by simply specifying a threshold value for the EIM cumulative sum (3.16); this implicitly defines how many normal modes, and possibly which ones, should be retained, thus completing the CB mode set selection procedure.

In addition, a normalized EIM distribution matrix [54], representing the contribution of each fixed-interface mode to the loads at each interface DOF, can be computed as:

$$\bar{\mathbf{E}} = \mathbf{P}^2 \left[\mathbf{I}\, \mathrm{Diag}\left(\overline{\mathbf{M}}\right) \right]^{-1} \tag{3.17}$$

Here, $\mathbf{P}^2$ indicates a term-by-term square of the modal participation factor matrix, while the Diag operator returns a column vector holding the diagonal elements of the argument matrix: the term in square brackets actually represents the inverse of the diagonal matrix containing the terms from the diagonal of $\overline{\mathbf{M}}$.

3.1.3 The Modal Truncation Augmentation technique

In this section, a brief explanation is provided about the application of the Modal Truncation Augmentation (MTA) technique to the CB reduction method [23, 31].

Let's first recall the fixed-interface eigenvalue problem mentioned in (3.5):

$$\mathbf{K}_{oo}\, \boldsymbol{\phi} = \mathbf{M}_{oo}\, \boldsymbol{\phi}\, \boldsymbol{\Omega} \tag{3.18}$$

When normal modes are mass-normalized, the flexibility matrix associated to the structure interior can be expressed as:

$$\mathbf{G} = \mathbf{K}_{oo}^{-1} = \boldsymbol{\phi}\, \boldsymbol{\Omega}^{-1}\, \boldsymbol{\phi}^{\mathrm{T}} \tag{3.19}$$

Since not *all* modes are retained in the reduced component representation, the complete modal basis can be divided into *kept* modes (subscript k) and *deleted*, or truncated, modes (subscript d). Equation (3.19) can thus be expressed as:

$$\mathbf{G} = \mathbf{G}_k + \mathbf{G}_d = \boldsymbol{\phi}_k\, \boldsymbol{\Omega}_k^{-1}\, \boldsymbol{\phi}_k^{\mathrm{T}} + \boldsymbol{\phi}_d\, \boldsymbol{\Omega}_d^{-1}\, \boldsymbol{\phi}_d^{\mathrm{T}} \tag{3.20}$$

The portion of the flexibility matrix not represented by the kept modes is called the *residual flexibility matrix*; combining (3.18, 3.19, 3.20) that can be obtained as:

$$\mathbf{G}_d = \mathbf{G} - \mathbf{G}_k = \mathbf{K}_{oo}^{-1} \left(\mathbf{I} - \mathbf{M}_{oo}\, \boldsymbol{\phi}_k\, \boldsymbol{\phi}_k^{\mathrm{T}} \right) \tag{3.21}$$

Let's now consider the CB transformation equation (3.3). The interior accelerations are simply obtained by taking the second time derivative of the corresponding displacements:

$$\ddot{\mathbf{u}}_o = \boldsymbol{\psi}\, \ddot{\mathbf{u}}_a + \boldsymbol{\phi}_k\, \ddot{\mathbf{q}}_k \tag{3.22}$$

Using (3.8) this can be expressed as:

$$\ddot{\mathbf{u}}_o = \boldsymbol{\psi}\,\ddot{\mathbf{u}}_a + \boldsymbol{\phi}_k\,\mathbf{P}\,\ddot{\mathbf{u}}_a - \boldsymbol{\phi}_k\,\boldsymbol{\Omega}_k\,\mathbf{q}_k \tag{3.23}$$

Going back to the equation of motion in physical coordinates as expressed in (3.2), considering the second row partition and solving for the interior-DOF displacements one obtains:

$$\mathbf{u}_o = -\,\mathbf{K}_{oo}^{-1}\left(\mathbf{M}_{oa}\,\ddot{\mathbf{u}}_a + \mathbf{M}_{oo}\,\ddot{\mathbf{u}}_o + \mathbf{K}_{oa}\,\mathbf{u}_a\right) \tag{3.24}$$

Substituting (3.23) into (3.24) and using (3.7c, 3.21) gives after some simple manipulation:

$$\mathbf{u}_o = \boldsymbol{\psi}\,\mathbf{u}_a + \boldsymbol{\phi}_k\,\mathbf{q}_k + \boldsymbol{\chi}\,\ddot{\mathbf{u}}_a \tag{3.25}$$

where the matrix $\boldsymbol{\chi}$ is a matrix of static displacement vectors associated with the internal inertia loads due to unit accelerations at each interface DOF while keeping the other interface DOFs constrained:

$$\boldsymbol{\chi} = -\mathbf{G}_d\left(\mathbf{M}_{oo}\,\boldsymbol{\psi} + \mathbf{M}_{oa}\right) \tag{3.26}$$

These vectors are finally orthogonalized with respect to the interior mass and stiffness matrices by solving an eigenvalue problem:

$$\mathbf{K}_\chi\,\boldsymbol{\mu} = \mathbf{M}_\chi\,\boldsymbol{\mu}\,\boldsymbol{\Lambda} \tag{3.27}$$

where $\mathbf{M}_\chi$ and $\mathbf{K}_\chi$ are computed ahead as:

$$\mathbf{M}_\chi = \boldsymbol{\chi}^{\mathrm{T}}\,\mathbf{M}_{oo}\,\boldsymbol{\chi} \tag{3.28a}$$

$$\mathbf{K}_\chi = \boldsymbol{\chi}^{\mathrm{T}}\,\mathbf{K}_{oo}\,\boldsymbol{\chi} \tag{3.28b}$$

The matrix holding the Modal Truncation Vectors (MTV) can now be defined:

$$\boldsymbol{\gamma} = \boldsymbol{\chi}\,\boldsymbol{\mu} \tag{3.29}$$

If mass normalization is enforced for the eigenvectors $\boldsymbol{\mu}$ in (3.27), then the following holds:

$$\boldsymbol{\gamma}^{\mathrm{T}}\,\mathbf{M}_{oo}\,\boldsymbol{\gamma} = \boldsymbol{\mu}^{\mathrm{T}}\,\boldsymbol{\chi}^{\mathrm{T}}\,\mathbf{M}_{oo}\,\boldsymbol{\chi}\,\boldsymbol{\mu} = \boldsymbol{\mu}^{\mathrm{T}}\,\mathbf{M}_\chi\,\boldsymbol{\mu} = \mathbf{I} \tag{3.30a}$$

$$\boldsymbol{\gamma}^{\mathrm{T}}\,\mathbf{K}_{oo}\,\boldsymbol{\gamma} = \boldsymbol{\mu}^{\mathrm{T}}\,\boldsymbol{\chi}^{\mathrm{T}}\,\mathbf{K}_{oo}\,\boldsymbol{\chi}\,\boldsymbol{\mu} = \boldsymbol{\mu}^{\mathrm{T}}\,\mathbf{K}_\chi\,\boldsymbol{\mu} = \boldsymbol{\Lambda} \tag{3.30b}$$

The MTVs in $\boldsymbol{\gamma}$ can then be depicted as pseudo-eigenvectors associated with the squared pseudo-eigenfrequencies in $\boldsymbol{\Lambda}$. They are consistent with the mass-normalized eigenmodes in $\boldsymbol{\phi}_k$, cfr. (3.18), and orthogonal to those with respect

to the interior mass and stiffness matrices, being related to the deleted modes $\boldsymbol{\phi}_d$: they can thus be regarded as high-frequency fixed-interface correction modes.

The augmented CB coordinate transformation can then be written as:

$$\begin{Bmatrix} \mathbf{u}_a \\ \mathbf{u}_o \end{Bmatrix} = \begin{bmatrix} \mathbf{I} & \mathbf{0} & \mathbf{0} \\ \boldsymbol{\psi} & \boldsymbol{\phi}_k & \boldsymbol{\gamma} \end{bmatrix} \begin{Bmatrix} \mathbf{u}_a \\ \mathbf{q}_k \\ \mathbf{q}_\gamma \end{Bmatrix} \tag{3.31}$$

Note that, while the size of the problem has increased by the number of additional modal coordinates $\mathbf{q}_\gamma$, its topology is completely unaltered, cfr. (3.3): that makes the method quite appealing, since the only additional effort is represented by the computation of the truncated displacement vector matrix $\boldsymbol{\chi}$, according to (3.26), and the subsequent solving of the eigenvalue problem in (3.27). Concerning the latter, it is worth clarifying that the number of MTVs is, in general, equal to the number of the interface DOFs defined for the structure: usually, especially in multibody dynamics applications, these are much fewer than the interior DOFs, so that solving the problem defined in (3.27) normally requires a small computational effort when compared to the eigenproblem related to the structure interior, cf. (3.18).

3.2 Model reduction implementation

3.2.1 Preprocessing

Finite Element models of the crankshaft and the connecting rod have been produced first, these representing the major components in the system. Since Nastran has been employed as FE software, Nastran terminology will be used in the following.

In both cases, the geometry has been simplified at the beginning of the process by removing all those features, as small fillets, which do not contribute significantly to the dynamic behaviour of the components, in order to make the meshing process as simple as possible and to speed up the modal reduction phase, by limiting the involved number of elements. Such a step is crucial when several modal reduction alternatives need to be investigated, as in the present research work, but should be avoided whenever the objective of the multibody modelling activity is to evaluate stresses on the components: in fact, this could be performed soon after the nonlinear simulation stage on the same component models by using modal-based stress recovery methodologies.

Second order tetrahedral elements (TET10) have been used for meshing purposes, those leading to better stiffness estimation with respect to their first order counterparts (TET4).

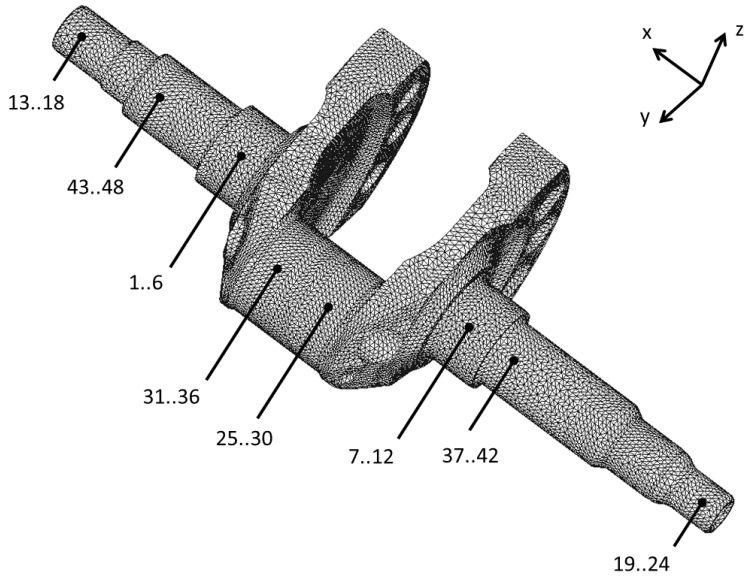

Figure 3.1 Crankshaft FE model. Interface DOF numbering is evidenced.

Particular care has been taken in the definition of interface DOFs. As discussed, in the CB technique a constraint mode is added to the reduced model representation for each of those DOFs: if all DOFs associated to all nodes lying on the interface surfaces of the considered component were placed in the *a*-set, then the dimension of the reduced solution would become unsuitable for nonlinear simulation purposes. Some sort of interface reduction is then required in order to minimize the total number of constraint modes. A common solution to this problem is based on the definition of *condensation nodes*, whose DOFs are placed in the *a*-set, which are linked to their corresponding interface surface nodes by means of multipoint constraint elements. Two kind of such elements are available in Nastran: RBE2 are *rigid* multipoint constraints which connect the interface surface nodes to the condensation node such that they are constrained to move as a rigid system, while RBE3 are *interpolation* multipoint constraints which define the displacement and the rotation of the condensation node as a weighted average of the motion of the interface surface nodes. Whereas RBE2, introducing artificial numerical stiffness, might result in an overestimation of the stiffness associated to the interface boundary conditions, RBE3 might lead to an underestimation, since interface surface deformation is permitted: the analyst is then required to properly choose between the two based upon the nature of

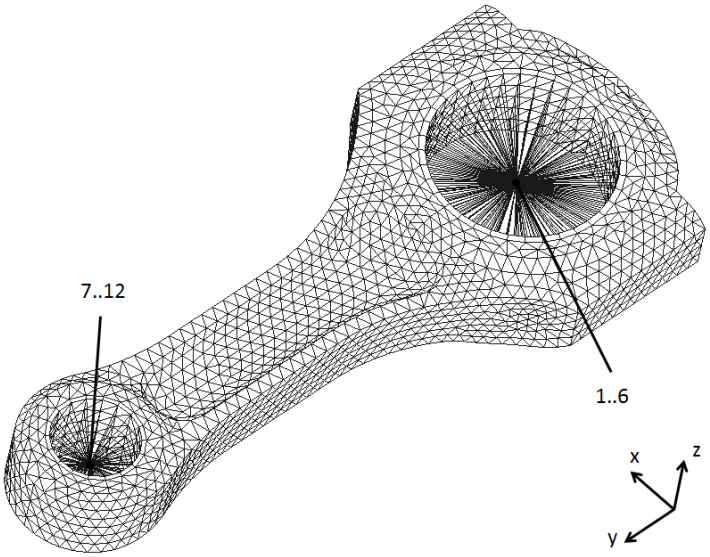

Figure 3.2 Connecting rod FE model. Interface DOF numbering is evidenced.

the various interfaces in the system.

In the present work, a total of eight condensation nodes were defined for the crankshaft, while two were identified for the connecting rod, see Figures 3.1, 3.2. RBE2 were used at the main bearing interfaces, since the crankshaft is somehow stiffened at those locations by the presence of the ball bearing inner rings. RBE2 were also used at the interfaces between the crankshaft and the two pinions, as well as at the crankshaft-flywheel interface, since pre-stressed contacts increase the stiffness at those locations[1]. On the other hand, RBE3 were adopted at the big end and small end interfaces, both on the crankshaft and on the conrod, since the clearance there allows considering the interface surfaces to deform almost independently from each other.

In each case, the condensation node has been placed at the center of the corresponding interface surface. For RBE3, the user is required to provide weighting factors for each interface surface node, which should be proportional to the part of the interface surface represented by each of those nodes. In order to avoid this time-consuming and mistake-prone activity, the interface surfaces have been meshed regularly, so that a unitary weighting factor can simply be assigned to

[1]Such behaviour has been evidenced by performing experimental modal analysis on a similar crankshaft, in several configurations, and by comparing the results with the corresponding numerical ones.

all interface grid points connected to the same condensation node.

It is worth mentioning that each condensation node should be chosen to be independent in order to allow for component coupling once model reduction is performed; while being standard for RBE2, in case of an RBE3 the user is required to explicitly define the element dependent DOFs, via the UM option, which allow to fully describe the rigid body motion of the interface surface [40]. In the present work, this task has been addressed by using the AUTOMSET parameter, which on one hand prevents the user to have full control on the multipoint constraint definition, on the other allowing a much easier implementation with satisfactory results.

Lumped inertia elements (CONM2) have been employed to model the flywheel and the two pinions attached to the crankshaft; mass properties of these components have been retrieved from their corresponding CAD representations. The same elements have been employed to model the balancing pads on the crankshaft, whose masses have been assigned so as to obtain a primary balance for the L-twin cranktrain under analysis.

Figures 3.1, 3.2 show the obtained crankshaft and conrod models, respectively, along with an indication of the interface DOF numbering[2], which will be useful in the remainder of the chapter.

3.2.2 The Craig-Bampton method in Nastran

Nastran provides an easy method to generate a reduced representation required by the ADAMS solver, namely a Modal Neutral File (MNF), starting from a FE model. A standard normal modes analysis solution sequence (SOL 103) is normally used, which needs to be complemented with two specific entries: the ADAMSMNF FLEXBODY=YES in the case control section causes the MNF file to be generated, while the DTI,UNITS in the bulk data section is used to specify the unit system to be used within the ADAMS environment.

An EIGRL card has to be specified with the required number of normal modes to include in the CB solution. An equal number of scalar points (SPOINT) are usually defined[3], and referenced by a QSET1 entry. An ASET1 entry specifies

[2] In Nastran, DOFs 1, 2, 3 represent translations along the x, y, z axes, respectively, while DOFs 4, 5, 6 represent rotations about those.

[3] Nastran recommends to specify 6 more scalar points with respect to the desired number of normal modes [64]: this causes 6 additional modes, which are referred to as *inertia-relief modes* or *residual vectors*, to be included in the coordinate transformation matrix used for model reduction. The process, however, is not very well documented and the mentioned modes are not directly recognizable as *inertia-relief modes*, *inertia-relief attachment modes*, or *residual inertia-relief attachment modes* as described in [16, 17]. These modes have not been employed in the present work.

which DOFs of which nodes are defined as interface DOFs, so that both constraint modes and fixed-interface normal modes can be computed (see Section 3.1.1); for both the crankshaft and the conrod models, all DOFs associated to each condensation node have been referenced by such entry.

It is worth mentioning that, in order to obtain a simplified representation for the mass matrix of the generic flexible component, which is based on the definition of nine inertia invariants computed before integrating the equations of motion, ADAMS requires the adoption of a lumped mass formulation for the starting FE model [63, 64]. This assumption will be used in the remainder of the chapter.

It is important to consider that the CB mode set obtained by the raw union of the N_a constraint modes and the N_k selected normal modes is not suitable for direct use in a multibody system simulation performed with ADAMS [63]: the CB modes are not an orthogonal set of modes, as evidenced by the fact that the reduced mass and stiffness matrices in (3.6) are not diagonal, so that coupling between the reduced model coordinates exists. Furthermore, since rigid-body modes are a special case of constraint modes, obtained when the interface DOFs are just sufficient to restrain rigid-body motion, embedded in the CB transformation matrix (3.3) are 6 rigid-body modes, which should be removed since ADAMS provides its own large-motion DOFs. An orthogonalization of the CB mode set is hence applied, by solving the eigenvector problem:

$$\mathbf{K}_{CB}\,\boldsymbol{\tau} = \mathbf{M}_{CB}\,\boldsymbol{\tau}\,\boldsymbol{\Theta} \tag{3.32}$$

where the new $N_a + N_k$ *orthogonal modes* and the associated eigenfrequencies squared are collected in the matrices $\boldsymbol{\tau}$ and $\boldsymbol{\Theta}$, respectively. The 6 rigid-body modes now explicitly appear in $\boldsymbol{\tau}$ and can be easily disabled.

The resulting generalized coordinates are no more directly split into the physical displacements related to the constraint modes and the modal displacements associated with the normal modes. A physical description of the modes in $\boldsymbol{\tau}$ is difficult: the physical meaning of the constraint modes is lost, but it can generally be observed that the first elastic mode shapes and their corresponding natural frequencies are basically identical to the mode shapes and natural frequencies of the original system analysed in free-free boundary conditions.

3.2.3 Implementation of the EIM concept

Nastran provides the user with a variety of solution sequences, as the mentioned `SOL 103`, consisting of a series of statements written in a proprietary language with its own compiler and grammatical rules, known as Direct Matrix Abstraction Program (DMAP). Each solution sequence consists of a series of functional

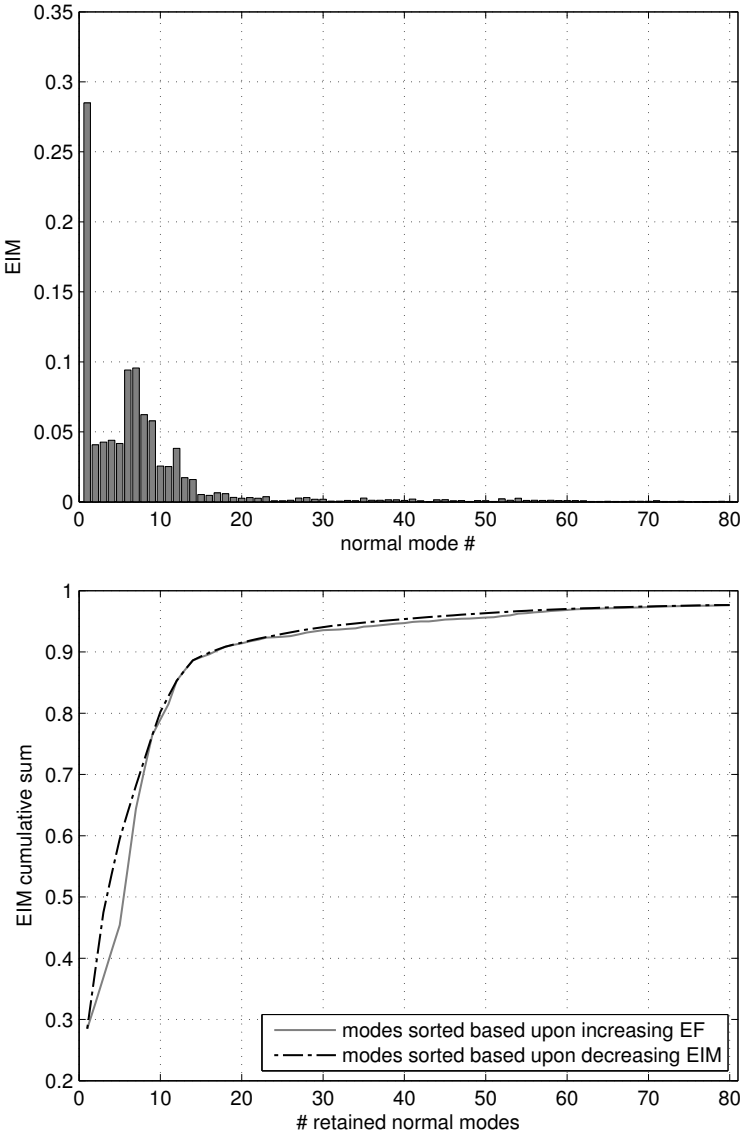

Figure 3.3 EIM values and EIM cumulative sum curves related to the fixed-interface normal modes of the crankshaft model.

modules, each having a unique name and a specific function, which are executed sequentially and which perform the operations required by the type of analysis the solution sequence relates to. The user is allowed to modify prewritten solution sequences using DMAP, by introducing scripts which are normally referred

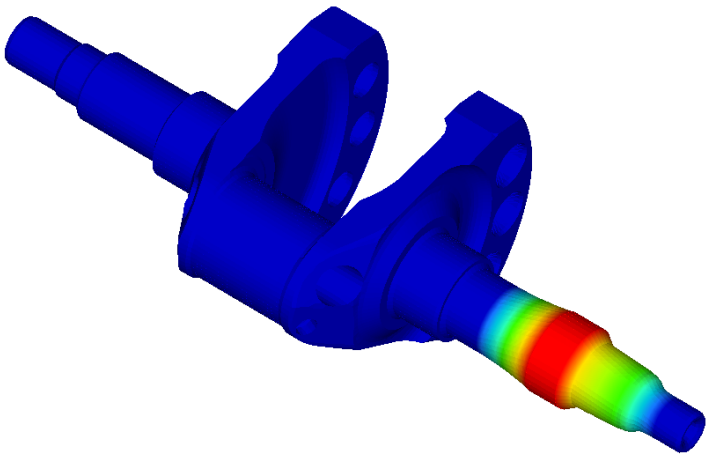

Figure 3.4 The crankshaft fixed-interface mode shape #1, holding the largest EIM value: torsional mode involving the flywheel (not shown).

to as *alters*.

In the present work, the discussed modal selection procedure based upon EIM was accomplished by exploiting this particular feature.

A first `SOL 103` run is used to compute and export the modal participation factor $\mathbf{P}$ and RIM matrices: this has been obtained by altering the subDMAP `SEMR3` to compute the RIM according to (3.14), by using the `MPYAD` module, then printing both matrices in ASCII format via the `OUTPUT4` statement.

These matrices are loaded by a Matlab script and used to compute the EIM values. Both $\mathbf{P}$ and $\overline{\mathbf{M}}$ are partitioned according to the defined translational (subscript t) and rotational (subscript r) interface DOFs; recalling (3.15), two vectors containing the EIM values are simply computed as:

$$\mathbf{E}_t = \frac{1}{\mathrm{Tr}\left(\overline{\mathbf{M}}_t\right)} \mathrm{Diag}\left(\mathbf{P}_t \, \mathbf{P}_t^{\mathrm{T}}\right) \tag{3.33a}$$

$$\mathbf{E}_r = \frac{1}{\mathrm{Tr}\left(\overline{\mathbf{M}}_r\right)} \mathrm{Diag}\left(\mathbf{P}_r \, \mathbf{P}_r^{\mathrm{T}}\right) \tag{3.33b}$$

An average of translational and rotational results is then computed, providing a single EIM value for each fixed-interface mode:

$$\mathbf{E} = \frac{1}{2}\mathbf{E}_t + \frac{1}{2}\mathbf{E}_r \tag{3.34}$$

An equal weight has been assigned to translational and rotational interface

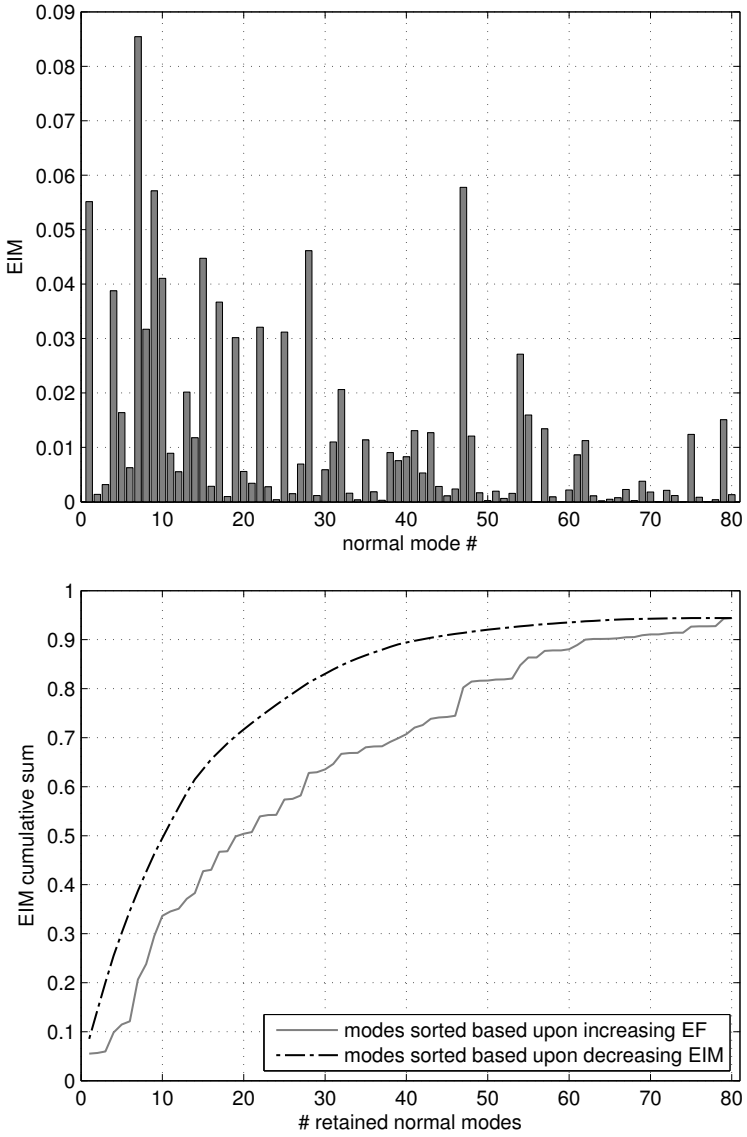

Figure 3.5 EIM values and EIM cumulative sum curves related to the fixed-interface normal modes of the conrod model.

DOFs; if needed, this can be easily modified by changing the weighting factors appearing in the previous equation.

A cumulative sum of the obtained EIM values is then computed and plotted by considering different modal ordering schemes, based upon *increasing* eigen-

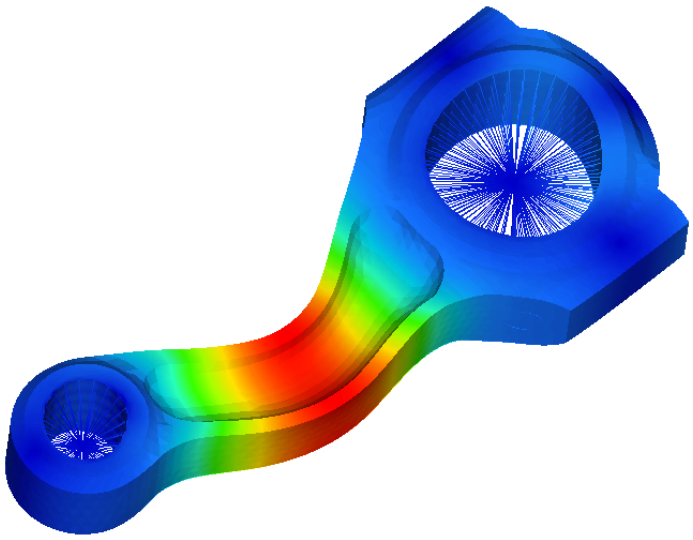

Figure 3.6 The conrod fixed-interface mode shape #7, holding the largest EIM value: flexural mode.

frequency (EF) and *decreasing* EIM value, respectively. This results very useful in determining a dynamic completeness level associated to a certain number of retained normal modes: by defining a target level of such dynamic completeness, e.g. 90%, the analyst has a direct indication of how many normal modes to include in the reduced component representation, for either chosen modal ordering scheme.

The EIM normalized distribution is computed according to (3.17), as well, and plotted as colormap plots: this helps the analyst in visualizing which modes contribute significantly to the loads at each interface DOF.

Figures 3.3, 3.5 show the EIM values related to 80 fixed-interface normal modes as computed for both the described crankshaft and connecting rod models, along with the associated cumulative sum curves; Figures 3.7, 3.8 show the related EIM distribution matrices.

For the crankshaft model, one can observe that the first 18 modes in terms of EF are also those holding the highest EIM values, at the same time contributing a level of EIM cumulative sum approximately equal to 90%: for such level of dynamic completeness, thus, both the EIM-based and the EF-based modal selection criteria eventually lead to the same modal base. The computation of the EIM values is not useless in such a case, since the EIM cumulative sum can be used as a general modal completeness indicator whether the EIM-based mode

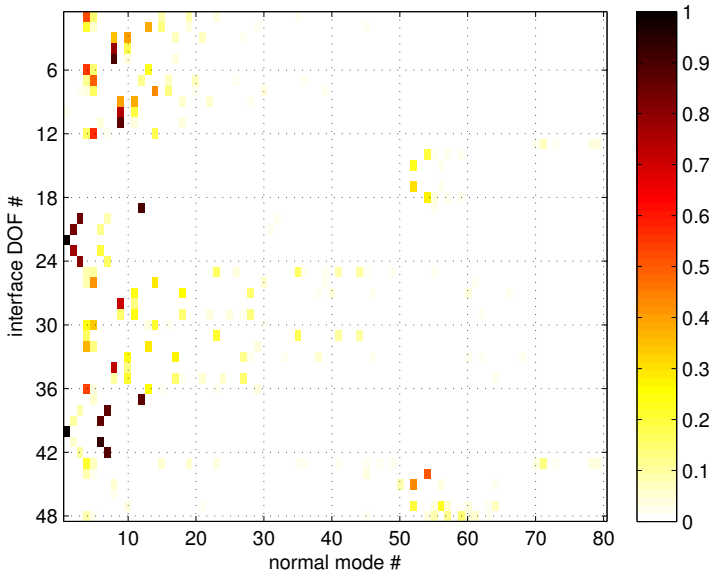

Figure 3.7 Normalized EIM distribution related to the fixed-interface normal modes of the crankshaft model.

selection criterion is adopted or not.

From a practical point of view, a second, standard Nastran run is enough, in such a case, to obtain the desired MNF: the user is only required to specify the number of roots resulting from the chosen threshold of dynamic completeness.

Regarding the connecting rod, the desired 90% level in terms of EIM cumulative sum is achieved by including the 42 highest EIM-valued modes in the modal base. An equal number of modes sorted based upon increasing EF contribute a significantly lower percentage of EIM cumulative sum in this case, namely 72%; on the other hand, one should retain a significantly larger number of modes, namely 62, in order to reach the specified target when adopting an EF-based selection: it is evident that the mode set chosen based upon EIM values constitutes the minimal set providing any specified dynamic completeness level expressed in terms of EIM cumulative sum. The computation of the EIM values is very useful in such a case, providing the analyst a way to identify specific modes to be retained and allowing a first assessment of the reduced component performance prior to the multibody simulation phase.

Whenever the EIM-based mode selection is employed, the chosen modes are processed by another Matlab script that creates a partitioning vector in ASCII format used in the subsequent Nastran run. This run is characterized by a dif-

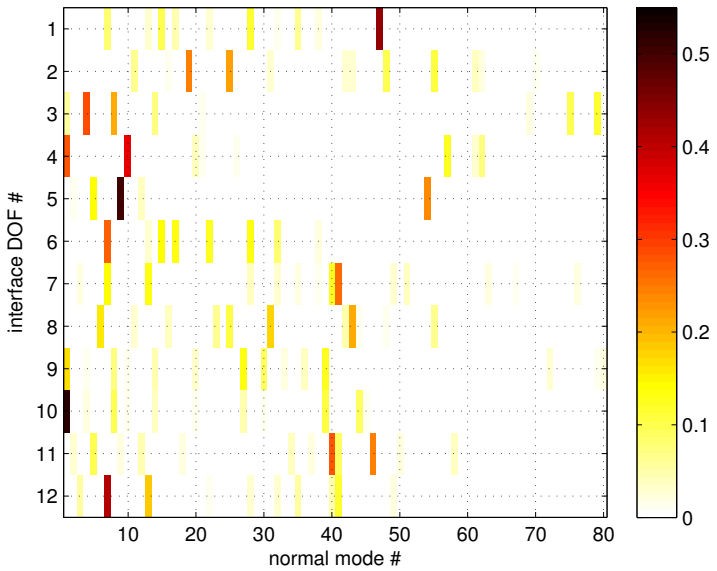

Figure 3.8 Normalized EIM distribution related to the fixed-interface normal modes of the conrod model.

ferent setup with respect to the former: the number of SPOINT, which is still equal to the number of modes specified in the EIGRL card, is determined by the highest mode, in terms of EF, which has to be retained, while a number of SPOINT equal to the required modes only is referenced now by the QSET1 entry. A DMAP alter has been written, and is called by this Nastran run, which alters the CMPMODE subDMAP by partitioning, via PARTN, the computed eigenvector and eigenvalue matrices $\boldsymbol{\phi}$ and $\boldsymbol{\Omega}$, see (3.5), with the supplied partitioning vector, and by equivalencing the original matrices to the partitions which have to be retained through EQUIVX: such operation basically removes those modes characterized by low EIM values, as computed in the previous steps, as well as the corresponding frequencies. Other minor modifications are made, in order to make the dimensions of all the involved matrices consistent.

3.2.4 Implementation of the MTA concept

In order to investigate the dynamic performances of the MTA approach, a procedure to complement a standard CB reduced solution with MTVs has been implemented, as well.

A first, standard SOL 103 run is used to compute and export the matrices holding the MTVs and their corresponding frequencies. This has been obtained

by altering the subDMAP SEMR3, where the required matrices are available. Recalling equations (3.21, 3.26), the matrix of static truncated displacement vectors can be rearranged as:

$$\boldsymbol{\chi} = -\mathbf{K}_{oo}^{-1}\,\mathbf{M}_{oo}\,\boldsymbol{\psi} - \mathbf{K}_{oo}^{-1}\,\mathbf{M}_{oo}\,\boldsymbol{\phi}_k\,\mathbf{P} \tag{3.35}$$

where the hypothesis of lumped mass has been made. Both terms on the right-hand-side of (3.35) are computed by using the FBS and MPYAD modules, since the needed matrices are already being used within the subDMAP and do not need any further effort. Once $\boldsymbol{\chi}$ has been computed, the matrices $\mathbf{M}_\chi$ and $\mathbf{K}_\chi$ are obtained according to (3.28) through SMPYAD; these matrices are then used to solve the eigenvalue problem in (3.27) via the LANCZOS module, obtaining the eigenvector and eigenvalue matrices $\boldsymbol{\mu}$ and $\boldsymbol{\Lambda}$, respectively. The MPYAD statement is again used to compute the matrix $\boldsymbol{\gamma}$ holding the MTVs, see (3.29).

Both $\boldsymbol{\gamma}$ and $\boldsymbol{\Lambda}$ matrices are then printed onto an ASCII file, via OUTPUT4, which is required as the input of a second Nastran run. In this case, the number of SPOINT, which are all referenced by the QSET1 entry, are set as the sum of the required number of normal modes in EIGRL and the desired number of MTVs. Note that the full set of MTVs, i.e. the matrix $\boldsymbol{\gamma}$, is made up by a number of vectors which equals the number of interface DOFs defined for the structure, while the analyst might want to complement the standard CB reduced representation of a component with a smaller number of vectors. In this respect, Fransen [31] proposed an interface reduction method based on solving the eigenvalue problem associated to the static (Guyan) partition of the CB representation (3.6). A simpler approach is adopted here: an alter to the subDMAP CMPMODE is provided, which, after having loaded the computed matrices via INPUTT4, appends $\boldsymbol{\gamma}$ to $\boldsymbol{\phi}_k$ through APPEND, and truncates the resulting matrix to the previously defined number of scalar points by means of the MATMOD module. The same principle is used to obtain the augmented eigenvalue matrix, but the process is made slightly more intricate in this case by the fact that both $\boldsymbol{\Omega}$ and $\boldsymbol{\Lambda}$ are diagonal matrices, so the latter one cannot just be appended to the former as done for the eigenvectors: the statements DIAGONAL, TRNSP, APPEND and MATMOD have been employed to obtain a correct solution. Only the specified number of MTVs, associated to the lowest pseudo-eigenfrequencies, are retained in this manner. The augmented matrices are assigned the native names by the EQUIVX statement, so that Nastran solver can recognize them in the remainder of the reduction process. Other minor operations are also performed, in order to make the dimensions of all relevant matrices consistent.

3.3 Assessment of the reduced component models

3.3.1 Validation in the frequency domain

In order to compare models obtained by using the described approaches, some numerical investigations have been performed prior to the multibody simulation phase onto the component models obtained in the previous steps.

The first step in the process has consisted in the implementation of a Matlab script used to convert the CB representation of a model to its *state-space* counterpart, this resulting very convenient for the subsequent frequency domain analyses. The state-space representation of a generic dynamic system holds:

$$\dot{\mathbf{x}} = \mathbf{A}\,\mathbf{x} + \mathbf{B}\,\mathbf{u} \tag{3.36a}$$

$$\mathbf{y} = \mathbf{C}\,\mathbf{x} + \mathbf{D}\,\mathbf{u} \tag{3.36b}$$

in which the output vector $\mathbf{y}$ is linked to the input vector $\mathbf{u}$ through a number of state variables collected in the vector $\mathbf{x}$, which represent the entire state of the system at any given time. Matrices $\mathbf{A}$ and $\mathbf{B}$ are the *state* and the *input* matrices, respectively, while $\mathbf{C}$ and $\mathbf{D}$ are the *output* and the *feedthrough* matrices.

Let's now recall the CB equation of motion (3.6):

$$\begin{bmatrix} \mathbf{M}_s & -\mathbf{P}^{\mathrm{T}} \\ -\mathbf{P} & \mathbf{I} \end{bmatrix} \begin{Bmatrix} \ddot{\mathbf{u}}_a \\ \ddot{\mathbf{q}} \end{Bmatrix} + \begin{bmatrix} \mathbf{0} & \mathbf{0} \\ \mathbf{0} & 2\boldsymbol{\zeta}\,\boldsymbol{\Omega}^{1/2} \end{bmatrix} \begin{Bmatrix} \dot{\mathbf{u}}_a \\ \dot{\mathbf{q}} \end{Bmatrix} + \begin{bmatrix} \mathbf{K}_s & \mathbf{0} \\ \mathbf{0} & \boldsymbol{\Omega} \end{bmatrix} \begin{Bmatrix} \mathbf{u}_a \\ \mathbf{q} \end{Bmatrix} = \begin{bmatrix} \mathbf{I} \\ \mathbf{0} \end{bmatrix} \mathbf{f}_a \tag{3.37}$$

which has been enriched here by introducing modal damping. The diagonal matrix $\boldsymbol{\zeta}$ collects the modal damping coefficients associated to the retained modes; a scalar could also be employed in the case of constant modal damping.

Equation (3.37) can be synthesized as follows:

$$\mathbf{M}_{\mathrm{CB}}\,\ddot{\mathbf{x}} + \mathbf{C}_{\mathrm{CB}}\,\dot{\mathbf{x}} + \mathbf{K}_{\mathrm{CB}}\,\mathbf{x} = \mathbf{L}_1\,\mathbf{f}_a \tag{3.38}$$

from which the *state equation* (3.36a) is readily obtained as:

$$\begin{Bmatrix} \dot{\mathbf{x}} \\ \ddot{\mathbf{x}} \end{Bmatrix} = \begin{bmatrix} \mathbf{0} & \mathbf{I} \\ -\mathbf{M}_{\mathrm{CB}}^{-1}\,\mathbf{K}_{\mathrm{CB}} & -\mathbf{M}_{\mathrm{CB}}^{-1}\,\mathbf{C}_{\mathrm{CB}} \end{bmatrix} \begin{Bmatrix} \mathbf{x} \\ \dot{\mathbf{x}} \end{Bmatrix} + \begin{bmatrix} \mathbf{0} \\ \mathbf{M}_{\mathrm{CB}}^{-1}\,\mathbf{L}_1 \end{bmatrix} \mathbf{f}_a \tag{3.39}$$

The *observation equation* (3.36b) can be written in a general form as:

$$\begin{Bmatrix} \mathbf{y}_1 \\ \mathbf{y}_2 \\ \mathbf{y}_3 \end{Bmatrix} = \begin{bmatrix} \mathbf{L}_2 & \mathbf{0} \\ \mathbf{0} & \mathbf{L}_2 \\ -\mathbf{L}_2\,\mathbf{M}_{\mathrm{CB}}^{-1}\,\mathbf{K}_{\mathrm{CB}} & -\mathbf{L}_2\,\mathbf{M}_{\mathrm{CB}}^{-1}\,\mathbf{C}_{\mathrm{CB}} \end{bmatrix} \begin{Bmatrix} \mathbf{x} \\ \dot{\mathbf{x}} \end{Bmatrix} + \begin{bmatrix} \mathbf{0} \\ \mathbf{0} \\ \mathbf{L}_2\,\mathbf{M}_{\mathrm{CB}}^{-1}\,\mathbf{L}_1 \end{bmatrix} \mathbf{f}_a \tag{3.40}$$

in which $\mathbf{y}_1$ is the displacement-based output, $\mathbf{y}_2$ is the velocity-based output, $\mathbf{y}_3$ is the acceleration-based output. The matrix $\mathbf{L}_2$ is a Boolean matrix defining whether physical, modal, or both kind of coordinates are desired in output.

Taking the Laplace transform of (3.36) gives after some simple manipulation the following expression for the Transfer Function (TF) matrix:

$$\mathbf{H}(s) = \mathbf{C}(s\mathbf{I} - \mathbf{A})^{-1}\mathbf{B} + \mathbf{D} \tag{3.41}$$

being s the Laplace variable. The TF evaluated along the frequency axis ($s = j\omega$) is the well-known Frequency Response Function (FRF).

The desired state-space matrices have been computed according to (3.39, 3.40), starting from the CB matrices exported in ASCII format by a former Nastran run. After the continuous-time state-space model has been created via the Matlab function `ss`, the desired FRF matrix can be easily computed through the `freqresp` command, upon the definition of the frequency band of interest.

In the present work, the whole FRF matrices for interface force input and interface acceleration output have been synthesized for both the crankshaft and the connecting rod models. In both cases, several models, each obtained by using a specific reduction strategy, have been tested against a reference model including a large modal base.

In order to retrieve the necessary quantitative information, a standard correlation index, namely the Frequency Response Assurance Criterion (FRAC) [43, 44], has been employed to compare the synthesized FRFs:

$$\mathrm{FRAC}_{ij} = \frac{\left|\mathbf{H}_{ij}^{\mathrm{T}}(\omega)\widehat{\mathbf{H}}_{ij}^{*}(\omega)\right|^2}{\left(\mathbf{H}_{ij}^{\mathrm{T}}(\omega)\mathbf{H}_{ij}^{*}(\omega)\right)\left(\widehat{\mathbf{H}}_{ij}^{\mathrm{T}}(\omega)\widehat{\mathbf{H}}_{ij}^{*}(\omega)\right)} \tag{3.42}$$

Here, $\mathbf{H}_{ij}$ and $\widehat{\mathbf{H}}_{ij}$ are column vectors, whose length equals the number of spectral lines, representing the FRFs between any output-input DOF couple ij, associated to different reduced models; both are evaluated over the same frequency range

Model	A_s	B_s	C_s
Normal modes	80 EF-sorted	18 EIM-sorted	12 EF-sorted
MTVs	-	-	6
Constraint modes	48	48	48
Total CB modes	128	66	66

Table 3.1 Features of the tested crankshaft models.

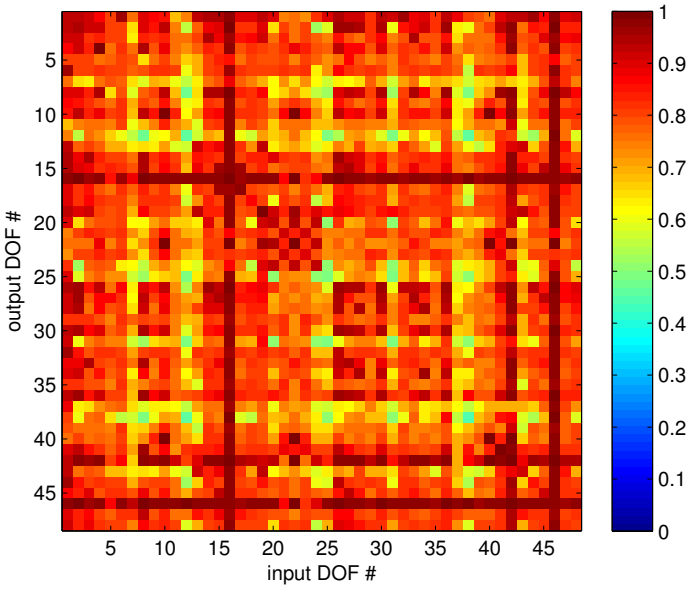

(a)

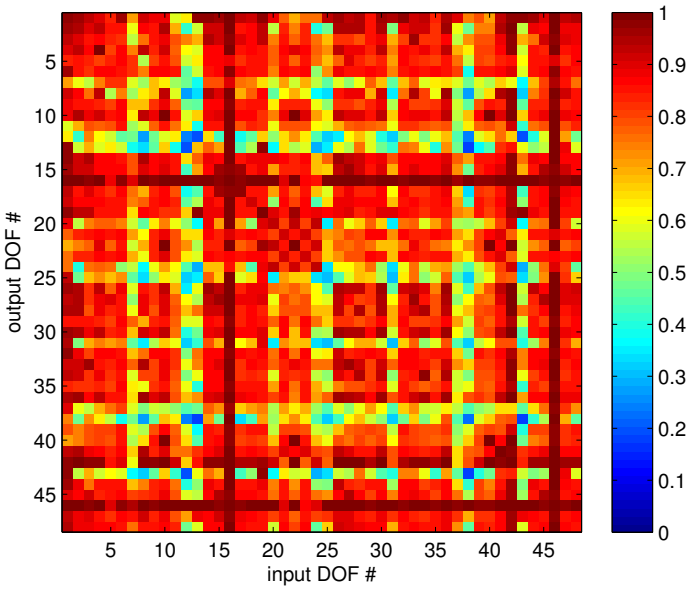

(b)

Figure 3.9 FRAC matrices as computed in the frequency range 0-10 kHz, related to the reduced crankshaft models B_s (a), and C_s (b).

with the same frequency resolution. The asterisk represents complex conjugate, while, as usual, the capital T indicates transpose. A FRAC value of 1 indicates

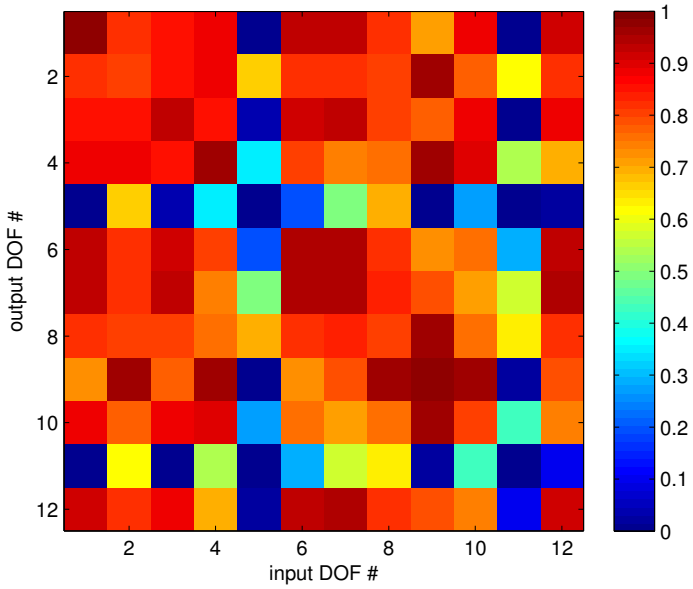

(a)

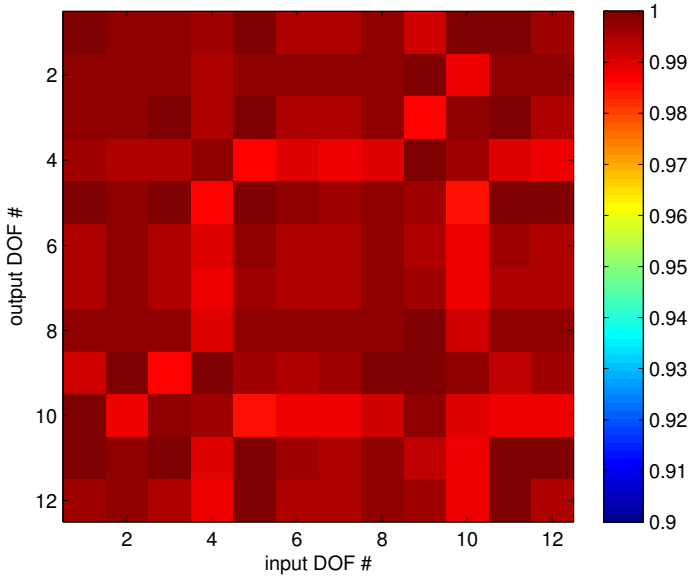

(b)

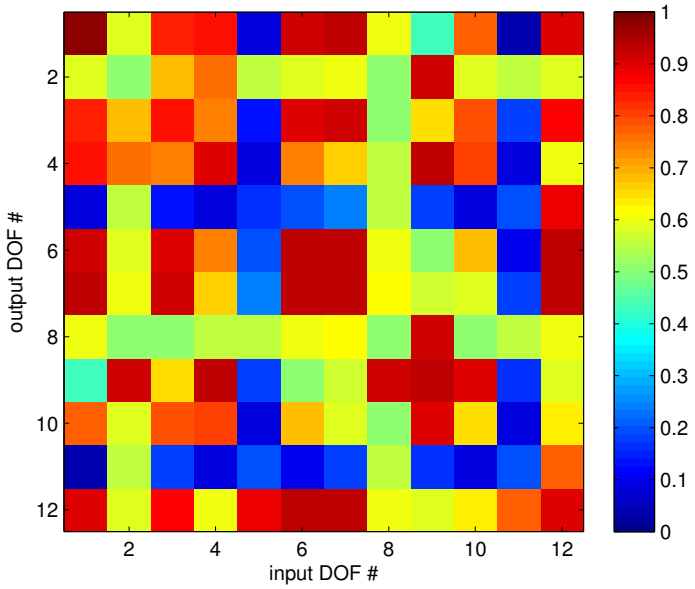

(c)

Figure 3.10 FRAC matrices computed in the frequency range 0-10 kHz, related to the reduced conrod models B_r (a), C_r (b), and D_r (c); note the different color scale.

identical FRFs; on the other hand, the FRAC will approach 0 in case of significantly different FRFs, expressing that there is little correlation between the two functions. Computing such correlation index for each couple of FRFs, one ends up with a square matrix of FRAC values having as much rows and columns as the number of interface DOFs, i.e. the size of the FRF matrices.

Concerning the crankshaft, two different models, including 18 between eigenmodes and pseudo-eigenmodes, and denoted as B_s, C_s, were tested against a reference model, A_s, including 80 normal modes; model features are reported

Model	A_r	B_r	C_r	D_r
Normal modes	80 EF-sorted	42 EIM-sorted	30 EF-sorted	42 EF-sorted
MTVs	-	-	12	-
Constraint modes	12	12	12	12
Total CB modes	92	54	54	54

Table 3.2 Features of the tested conrod models.

in Table 3.1. It is worth recalling that, for this particular model, having chosen a target level of dynamic completeness of 90% in terms of EIM cumulative sum, both the EIM-based and the EF-based modal selection criteria lead to the same modal base, the 18 highest EIM-valued modes being at the same time the lowest-EF ones, see Figure 3.3.

Figure 3.9 shows the computed FRAC matrices, related to the mentioned reduced crankshaft models, for FRFs evaluated in the frequency range 0 – 10 kHz. Both models exhibit a good correspondence with the reference in this frequency range, being model B_s slightly superior to model C_s.

As for the conrod, three models, including 42 between eigenmodes and pseudo-eigenmodes, and denoted as B_r, C_r, D_r, were tested against a reference model, A_r, including 80 normal modes; model features are summarized in Table 3.2.

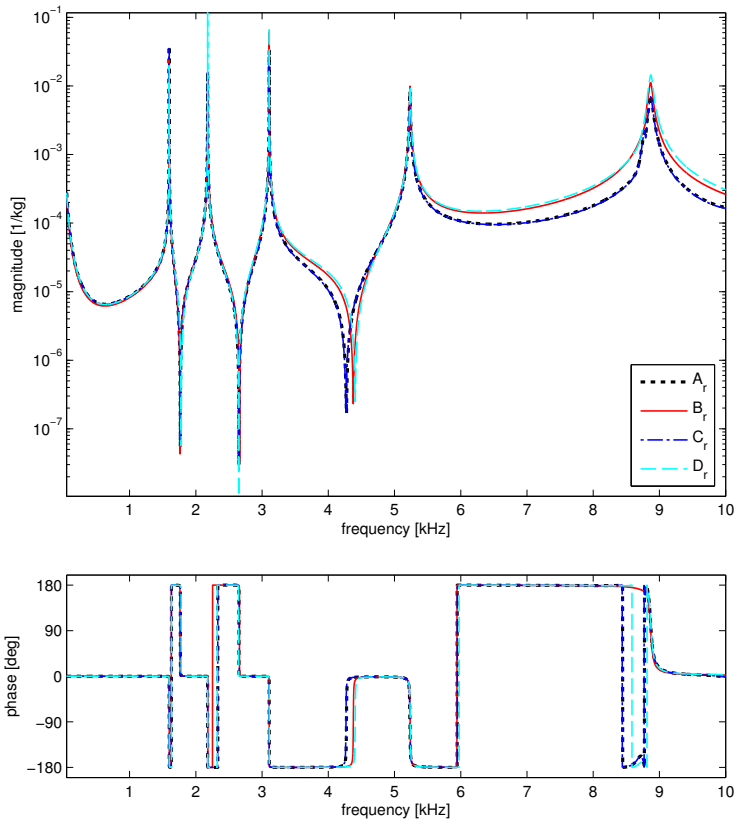

Figure 3.11 Comparison between FRFs corresponding to the different conrod models.

Figure 3.10 presents the computed FRAC matrices, related to the mentioned reduced conrod models, for FRFs evaluated in the frequency range 0 – 10 kHz. While model B_r shows acceptable correspondence with model A_r, model C_r fits almost perfectly the reference, with FRAC values far above 0.9 for every input-output couple. Model B_r demonstrates superior performance in comparison with model D_r, as a consequence of the fact that the most dynamically important modes with respect to interface forces are retained. As an example, the synthesized FRFs for input-output DOF couple 9-1 are shown in Figure 3.11.

3.3.2 Validation in the modal domain

Another kind of test has been performed onto the aforementioned reduced models of the crankshaft and the connecting rod, in order to evaluate the correspondence of the associated orthogonalized CB modes, and related eigenfrequencies, to those of the two models chosen as reference. A standard shape correlation index, namely the Modal Assurance Criterion (MAC) [1, 44], has been employed for the purpose:

$$\mathrm{MAC}_{ij} = \frac{\left|\boldsymbol{\Phi}_i^{\mathrm{T}} \widehat{\boldsymbol{\Phi}}_j\right|^2}{\left(\boldsymbol{\Phi}_i^{\mathrm{T}} \boldsymbol{\Phi}_i\right)\left(\widehat{\boldsymbol{\Phi}}_j^{\mathrm{T}} \widehat{\boldsymbol{\Phi}}_j\right)} \tag{3.43}$$

where $\boldsymbol{\Phi}$ and $\widehat{\boldsymbol{\Phi}}$ are the modal matrices having as columns the deformation shapes obtained by expanding the associated orthogonalized CB modes (3.32) back to physical coordinates. The MAC takes values from 0, representing no correspondence between the compared shapes, to 1, representing a perfect correspondence. Computing such correlation index for each mode couple ij, one ends up with a matrix of MAC values, whose dimensions equal the number of modes of the compared models, showing which shape vectors in $\widehat{\boldsymbol{\Phi}}$, associated to the reference model in this case, are preserved in $\boldsymbol{\Phi}$, representing the reduced model.

The MAC alone does not provide any indication about the frequency of the compared modes; therefore, it has been complemented here with a simple eigenfrequency correlation index, sometimes referred to as Natural Frequency Difference (NFD), defined as:

$$\mathrm{NFD}_{ij} = \frac{\left|\omega_i - \widehat{\omega}_j\right|}{\widehat{\omega}_j} \tag{3.44}$$

where ω_i and $\widehat{\omega}_j$ are the two eigenfrequencies corresponding to the eigenmodes $\boldsymbol{\Phi}_i$ and $\widehat{\boldsymbol{\Phi}}_j$. Obviously, the lower the NFD, the higher the correspondence between eigenfrequencies. In order to allow for a correct interpretation of the

results, the NFD has been computed only for correlated mode pairs whose MAC exceeds 0.8: the analyst has thus a clear indication about frequency shifts occurring due to reduced model completeness.

Figures 3.12 and 3.13 show the MAC and NFD matrices related to the crankshaft models B_s and C_s, respectively, computed by taking model A_s as reference; matrices shown here are truncated, due to poor correlation concerning the highest modes of reference model A_s. Again, model B_s appears to be slightly superior with respect to model C_s, even if the two look indeed very close: this is proved by the large correspondence evidenced by MAC and NFD values obtained through a direct comparison of the two models, see Figure 3.14.

Concerning the connecting rod models, the MAC and NFD matrices computed for models B_r, C_r and D_r with model A_r as reference, are shown in Figures 3.15, 3.16 and 3.17, respectively. Model D_r keeps acceptable correspondence with the reference for approximately the first 50 modes, even if some lower frequency ones are clearly missing and some eigenfrequency differences are evidenced by the NFD, as well. Model C_r shows a much improved low frequency behaviour, with very high MAC and low NFD values for the first 40 orthogonal modes, approximately. While both models C_r and D_r tend to emphasize low frequency modes, model B_r exhibits a clear deviation towards higher frequency ones, some of which are preserved at the expense of some lower frequency lack; in addition, unlike model D_r, most of the correlated mode pairs have very low NFD values.

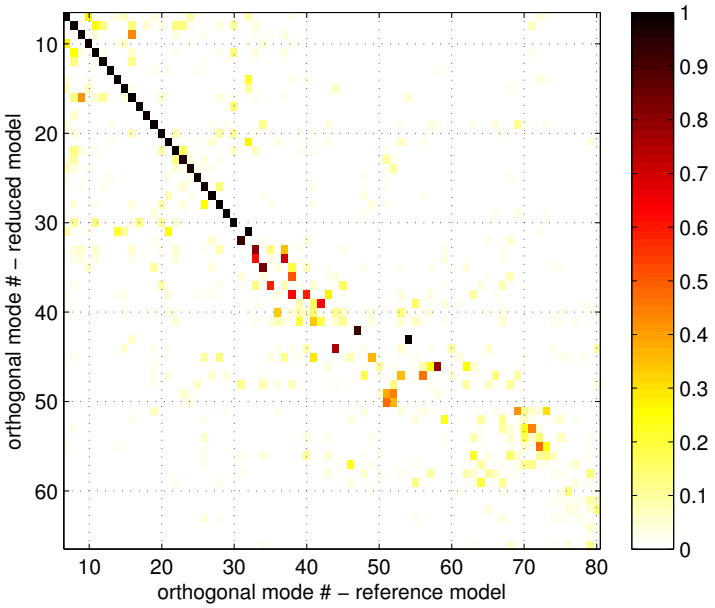

(a)

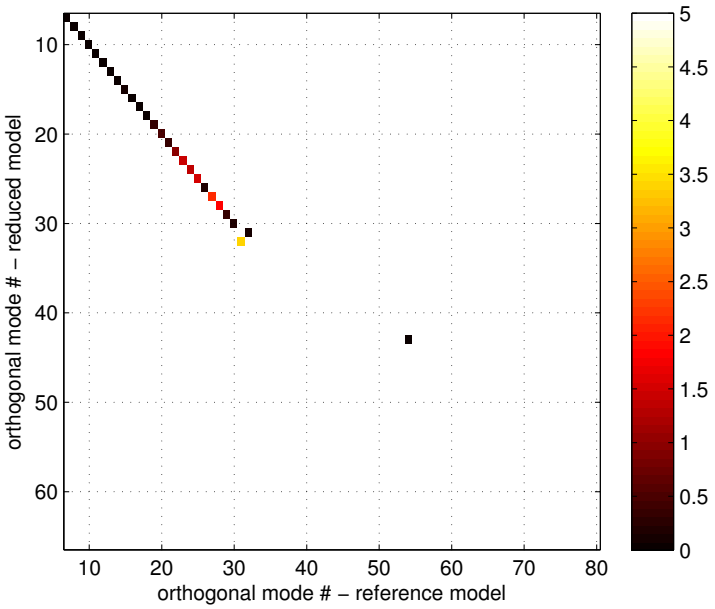

(b)

Figure 3.12 MAC (a) and percentage NFD (b) matrices related to crankshaft models A_s, B_s. Rigid-body modes (1-6) are excluded from the comparison.

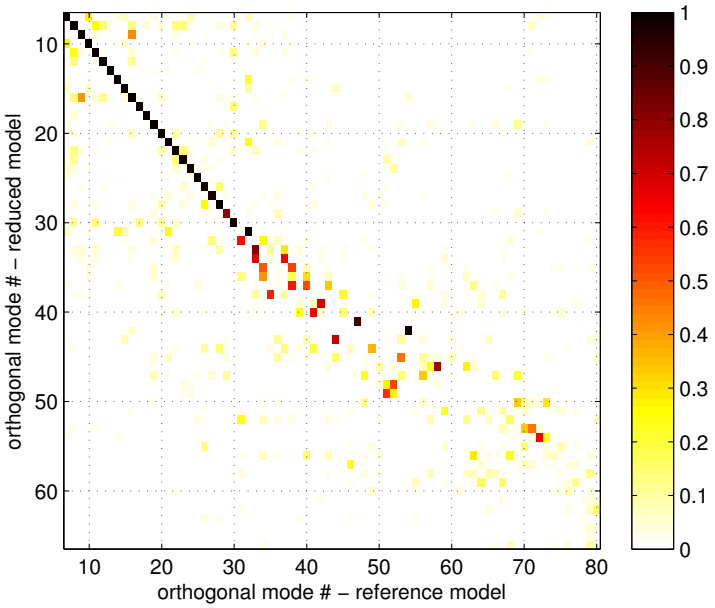

(a)

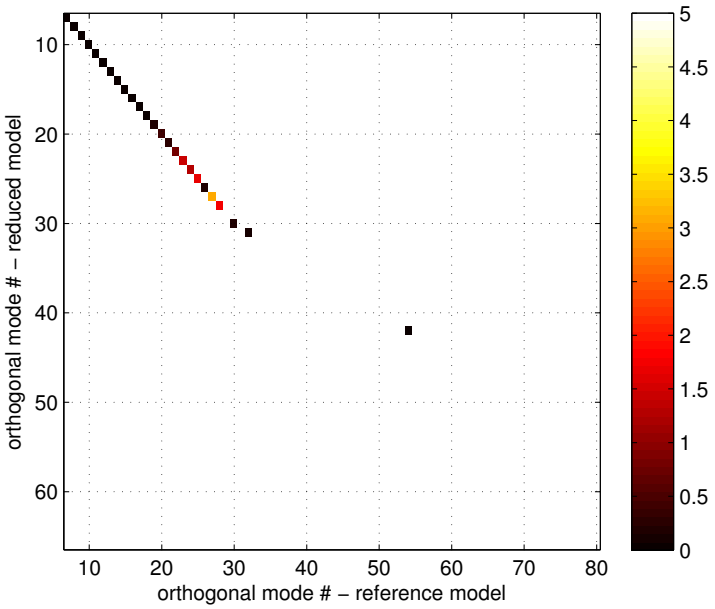

(b)

Figure 3.13 MAC (a) and percentage NFD (b) matrices related to crankshaft models A_s, C_s. Rigid-body modes (1-6) are excluded from the comparison.

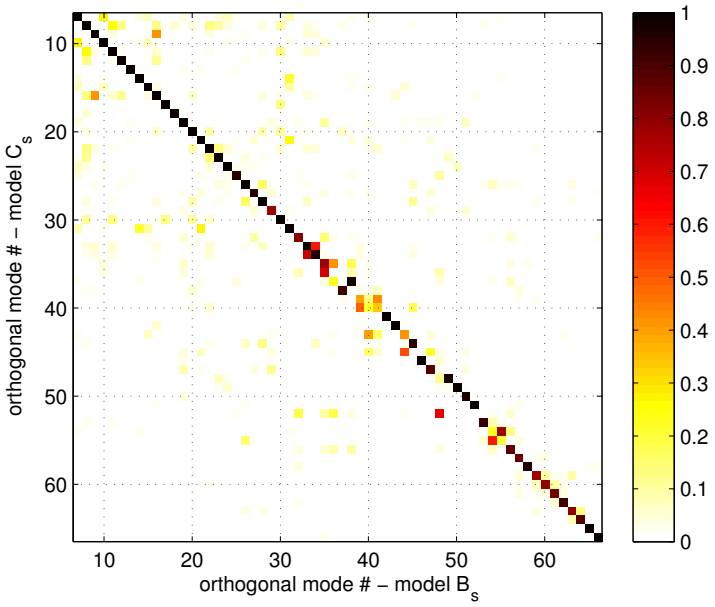

(a)

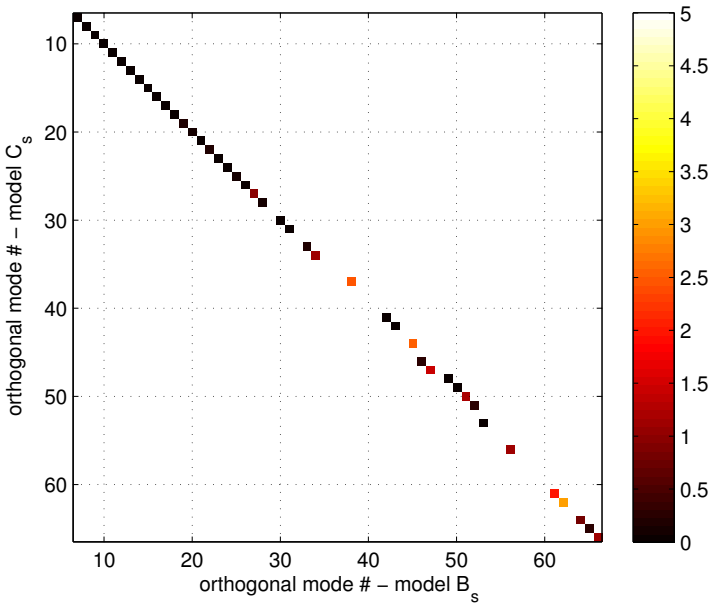

(b)

Figure 3.14 MAC (a) and percentage NFD (b) matrices related to crankshaft models B_s, C_s. Rigid-body modes (1-6) are excluded from the comparison.

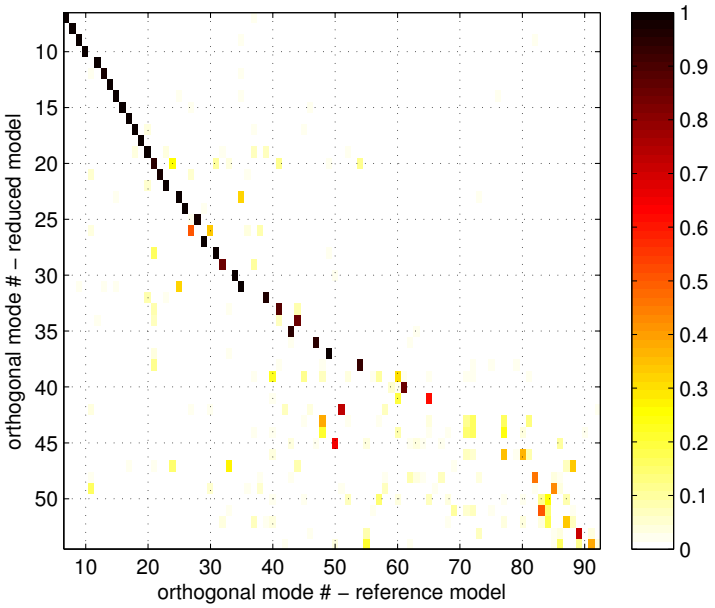

(a)

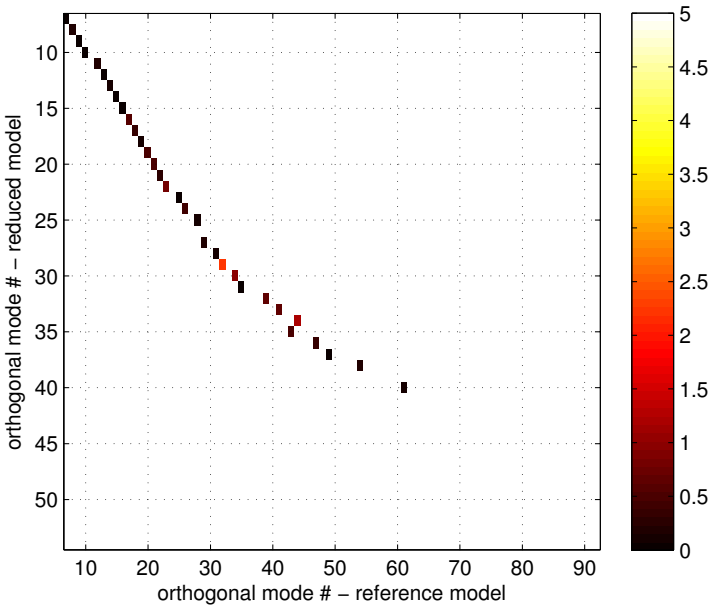

(b)

Figure 3.15 MAC (a) and percentage NFD (b) matrices related to conrod models A_r, B_r. Rigid-body modes (1-6) are excluded from the comparison.

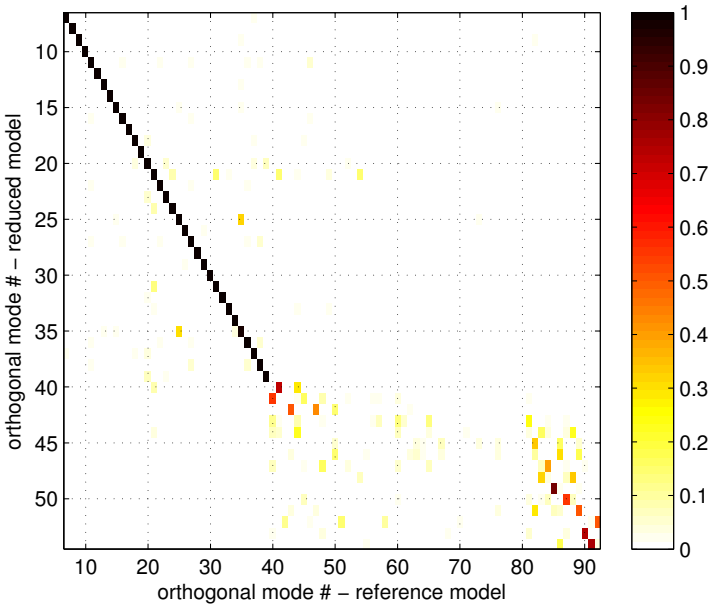

(a)

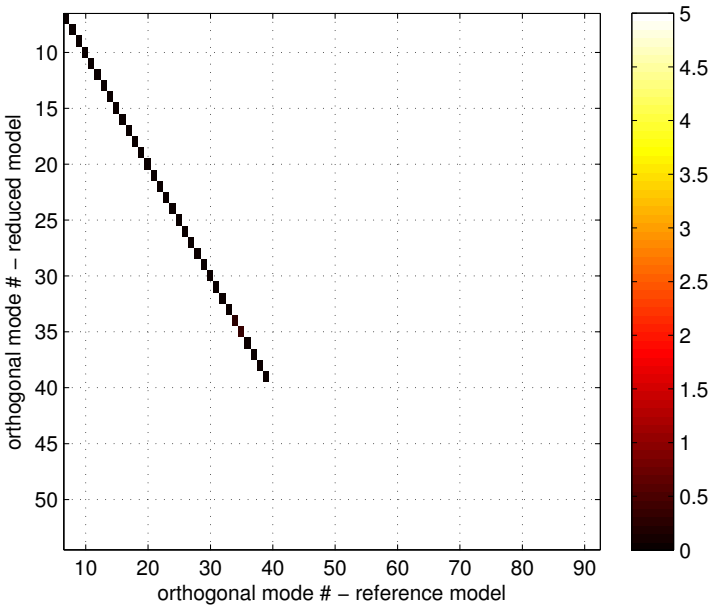

(b)

Figure 3.16 MAC (a) and percentage NFD (b) matrices related to conrod models A_r, C_r. Rigid-body modes (1-6) are excluded from the comparison.

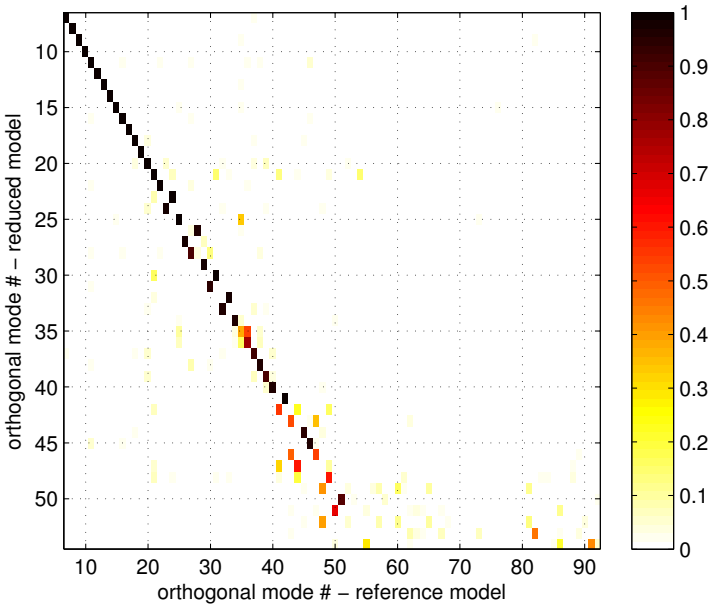

(a)

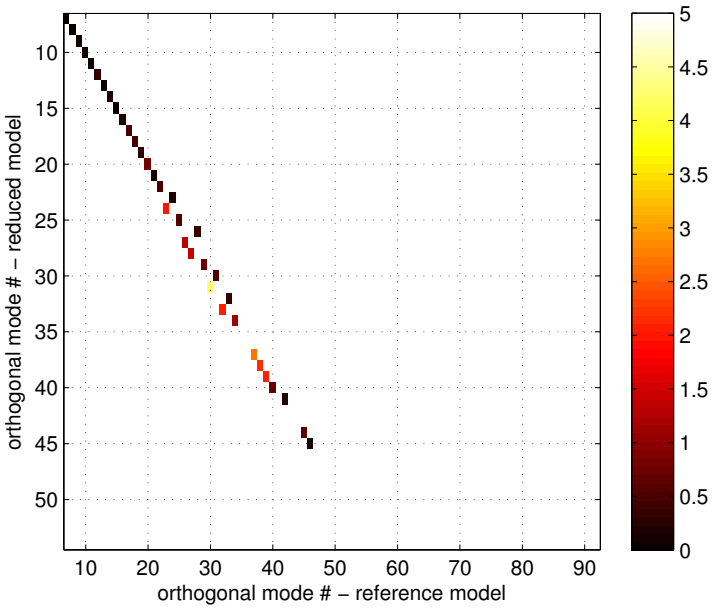

(b)

Figure 3.17 MAC (a) and percentage NFD (b) matrices related to conrod models A_r, D_r. Rigid-body modes (1-6) are excluded from the comparison.

Chapter 4

Flexible multibody modelling

Modern powertrain design is facing increasingly strict requirements in terms of emissions, fuel consumption, noise and vibration levels. In recent years, this trend is extending towards the motorcycle industry, in which competitive design focused on achieving a high power-to-weight ratio calls for optimized engine components. This in turn requires the adoption of a multidisciplinary approach early in the conception phase, and the use of advanced simulation tools which help the analyst in gaining a deeper insight into the physical phenomena associated with the engine operation. Concerning structural design aspects, modern analysis techniques involve the adoption of multibody simulation tools, which allow an accurate prediction of loads acting on the system components at operational speed, thus improving the subsequent stress and fatigue life analysis.

Several approaches are described in literature dealing with multibody modelling of internal combustion (IC) engine powertrains. Some papers deal with the construction of fully coupled cranktrain models through the use of commercial multibody dynamics codes, which provide a general modelling platform for mechanical systems, see e.g. [10, 12, 25, 26, 28, 66, 71, 72, 82, 83]: the system equations of motion are in this case automatically generated by the software kernel, and solved by means of some standard integration scheme. As an alternative, some studies describe the development of specialized modelling codes, see [14, 24, 27, 47, 58, 61, 68, 69, 70]: the system equations of motion are retrieved analytically and implemented in specific computational algorithms. In this work, the former approach has been followed to investigate the elastodynamic behaviour of a motorbike engine cranktrain. The modelling activity is supported by means of ADAMS multibody simulation software: this package offers standard performance in terms of results accuracy versus simulation time, also allowing for a seamless integration with other simulation tools, e.g. Finite Element (FE)

codes, and a straightforward procedure in defining customized subroutines.

In the context of multibody modelling, the definition of a system made up of rigid links connected to each other via kinematic joints typically represents the first step in the process; in fact, commercial multibody software platforms offer both CAD interfaces and joint libraries, permitting the analyst to set up a basic dynamic model with little time and effort. Clearly, this modelling approach is affected by some important limitations: first of all, the adoption of rigid bodies in combination with kinematic joints prevents some interface loads to be evaluated whenever the mechanism under study exhibits some static indeterminacy; furthermore, any dynamic amplification effect, which might significantly affect the actual loads, is evidently lost. These shortcomings can be eliminated by embracing a refined modelling methodology, based upon the introduction of non-ideal joints at interface locations, and the inclusion of component flexibility. Both strategies have been implemented in the present simulation work, adopting the bearing models and the flexible component reduction schemes depicted in the previous chapters.

4.1 Theoretical background

4.1.1 Flexible body kinematics

Among the methods available for the description of motion of flexible multibody systems [75, 80], the *floating frame of reference* formulation is certainly the most widely used, and is currently implemented in several commercial multibody dynamics software packages. Since ADAMS has been used for the present simulation work, this section briefly describes how the equations of motion are retrieved by using such formulation [63, 76].

The basic idea behind the floating frame of reference formulation is that the configuration of the generic deformable body within the multibody system can be described by separating the *large*, nonlinear displacement of a coordinate system attached to the body, and the *small*, linear deformations occurring about that reference frame. Location and orientation of such frame with respect to the global coordinate system are defined by:

$$\mathbf{q}_r^b = \begin{Bmatrix} \mathbf{R}^b \\ \boldsymbol{\theta}^b \end{Bmatrix} \tag{4.1}$$

where $\mathbf{R}^b$ is a set of Cartesian coordinates that define the location of the body reference frame, expressed in the *global* coordinate system, and $\boldsymbol{\theta}^b$ is a set of rotational coordinates that describe the orientation of the selected body. We

are now dropping the superscript identifying body b; we will refer to the same flexible body in the remainder, unless specified.

The global position of the i-th arbitrary grid point on the body can be written as:

$$\mathbf{r}_i = \mathbf{R} + \mathbf{A}\,\underline{\mathbf{u}} \tag{4.2}$$

where $\underline{\mathbf{u}}$ is the vector representing the local position of the point, expressed in the *local* reference frame; for the sake of clarity, vectors whose components are expressed in the local reference frame are underlined in this section. Matrix $\mathbf{A}$ is the transformation matrix from the local reference frame to ground; this can be expressed by using different orientation parameter sets, such as *Euler angles*, *Euler parameters*, or *Rodriguez parameters* [76]. Since the considered body is flexible, the local position of the generic grid point i can in turn be expressed as:

$$\underline{\mathbf{u}} = \underline{\mathbf{u}}_o + \underline{\mathbf{u}}_f = \underline{\mathbf{u}}_o + \boldsymbol{\Phi}_{\mathrm{R}i}\,\mathbf{q}_f \tag{4.3}$$

being $\underline{\mathbf{u}}_o$ the position of the point in the undeformed state and $\underline{\mathbf{u}}_f$ the translational deformation vector; this latter is the product of $\boldsymbol{\Phi}_{\mathrm{R}i}$, which is a slice of the modal matrix which corresponds to the translational DOFs associated to the node, and the vector of generalized elastic coordinates $\mathbf{q}_f$. This latter is added to the generalized reference coordinates in (4.1) to obtain the flexible body *generalized coordinates*:

$$\mathbf{q} = \begin{Bmatrix} \mathbf{q}_r \\ \mathbf{q}_f \end{Bmatrix} = \begin{Bmatrix} \mathbf{R} \\ \boldsymbol{\theta} \\ \mathbf{q}_f \end{Bmatrix} \tag{4.4}$$

Combining (4.2, 4.3) the global position of the considered point holds:

$$\mathbf{r}_i = \mathbf{R} + \mathbf{A}\left(\underline{\mathbf{u}}_o + \underline{\mathbf{u}}_f\right) \tag{4.5}$$

which differentiated with respect to time yields its global velocity:

$$\dot{\mathbf{r}}_i = \dot{\mathbf{R}} + \dot{\mathbf{A}}\underline{\mathbf{u}} + \mathbf{A}\,\dot{\underline{\mathbf{u}}}_f \tag{4.6}$$

Introducing the angular velocity of the body, the time derivative of the rotation matrix can be expressed as:

$$\dot{\mathbf{A}} = \mathbf{A}\,\tilde{\underline{\boldsymbol{\omega}}} \tag{4.7}$$

where $\underline{\boldsymbol{\omega}}$ is the angular velocity vector defined in the local coordinate system, and the tilde denotes the skew operator:

$$\tilde{\underline{\boldsymbol{\omega}}} = \begin{bmatrix} 0 & -\underline{\omega}_z & \underline{\omega}_y \\ \underline{\omega}_z & 0 & -\underline{\omega}_x \\ -\underline{\omega}_y & \underline{\omega}_x & 0 \end{bmatrix} \tag{4.8}$$

The equation (4.6) can therefore be rewritten as:

$$\dot{\mathbf{r}}_i = \dot{\mathbf{R}} + \mathbf{A}\,\tilde{\underline{\boldsymbol{\omega}}}\underline{\mathbf{u}} + \mathbf{A}\,\dot{\underline{\mathbf{u}}}_f = \dot{\mathbf{R}} - \mathbf{A}\,\tilde{\underline{\mathbf{u}}}\underline{\boldsymbol{\omega}} + \mathbf{A}\,\dot{\underline{\mathbf{u}}}_f \tag{4.9}$$

Introducing the relationship between the angular velocity and the time derivative of the orientation states,

$$\underline{\boldsymbol{\omega}} = \underline{\mathbf{B}}\dot{\boldsymbol{\theta}} \tag{4.10}$$

the matrix $\underline{\mathbf{B}}$ being a transformation matrix depending on the orientation parameters, and using (4.3), equation (4.9) can be rewritten as:

$$\dot{\mathbf{r}}_i = \dot{\mathbf{R}} - \mathbf{A}\,\tilde{\underline{\mathbf{u}}}\underline{\mathbf{B}}\dot{\boldsymbol{\theta}} + \mathbf{A}\,\boldsymbol{\Phi}_{\mathrm{R}i}\,\dot{\mathbf{q}}_f \tag{4.11}$$

which can be easily rearranged in matrix format:

$$\dot{\mathbf{r}}_i = \begin{bmatrix}\mathbf{I} & -\mathbf{A}\,\tilde{\underline{\mathbf{u}}}\underline{\mathbf{B}} & \mathbf{A}\,\boldsymbol{\Phi}_{\mathrm{R}i}\end{bmatrix}\begin{Bmatrix}\dot{\mathbf{R}}\\ \dot{\boldsymbol{\theta}}\\ \dot{\mathbf{q}}_f\end{Bmatrix} = \mathbf{L}_i\,\dot{\mathbf{q}} \tag{4.12}$$

Concerning orientation, as the body deforms the generic frame attached to the considered node i rotates relative to the body reference frame. In complete analogy with the translational deformations $\underline{\mathbf{u}}_f$, these *small* angles can be expressed using modal superposition as:

$$\underline{\boldsymbol{\vartheta}}_i = \boldsymbol{\Phi}_{\theta i}\,\mathbf{q}_f \tag{4.13}$$

in which $\boldsymbol{\Phi}_{\theta i}$ is a slice of the modal matrix which corresponds to the rotational DOFs associated to node i. The angular velocity of the considered frame with respect to the body reference frame can be obtained by simply taking the time derivative of (4.13), obtaining:

$$\dot{\underline{\boldsymbol{\vartheta}}}_i = \boldsymbol{\Phi}_{\theta i}\,\dot{\mathbf{q}}_f \tag{4.14}$$

Summing this angular velocity to the angular velocity of the body reference frame yields the angular velocity with respect to the global coordinate system:

$$\underline{\boldsymbol{\omega}}_i = \underline{\boldsymbol{\omega}} + \dot{\underline{\boldsymbol{\vartheta}}}_i = \underline{\mathbf{B}}\dot{\boldsymbol{\theta}} + \boldsymbol{\Phi}_{\theta i}\,\dot{\mathbf{q}}_f \tag{4.15}$$

which can easily be rearranged as a function of the body generalized coordinates as:

$$\underline{\boldsymbol{\omega}}_i = \begin{bmatrix}\mathbf{0} & \underline{\mathbf{B}} & \boldsymbol{\Phi}_{\theta i}\end{bmatrix}\begin{Bmatrix}\dot{\mathbf{R}}\\ \dot{\boldsymbol{\theta}}\\ \dot{\mathbf{q}}_f\end{Bmatrix} = \mathbf{N}_i\,\dot{\mathbf{q}} \tag{4.16}$$

We will use the obtained expressions for the definition of the body kinetic energy in the following sections.

4.1.2 Kinematic constraints

In multibody systems, the individual bodies cannot generally move freely, being linked to each other by a number of joints, and being subjected to specified motion trajectories: in fact, the generalized coordinates are related by a number of constraint equations.

Constraints can be *holonomic*, if they impose restrictions on the positions of the individual bodies in the system, or *nonholonomic*, if they restrict the possible values of their velocities. Considering the former case, the constraint equations can be written in the following vector form:

$$\mathbf{C}\left(\mathbf{q}, t\right) = \mathbf{0} \tag{4.17}$$

where $\mathbf{C}$ is the vector of constraint functions that depend on the system generalized coordinates and possibly on time. The previous constitutes a set of nonlinear algebraic constraint equations.

For a virtual change in the system generalized coordinates $\delta\mathbf{q}$, equation (4.17) gives:

$$\mathbf{C}_\mathbf{q}\,\delta\mathbf{q} = \mathbf{0} \tag{4.18}$$

where $\mathbf{C}_\mathbf{q}$ is the system *Jacobian matrix* containing the partial derivatives of the constraint functions with respect to the generalized coordinates. Considering linearly independent constraint functions, such matrix has full row rank.

Differentiating (4.17) with respect to time yields the kinematic equation that relates the generalized velocities of the multibody system:

$$\mathbf{C}_\mathbf{q}\,\dot{\mathbf{q}} = -\,\mathbf{C}_t \tag{4.19}$$

being $\mathbf{C}_t$ the partial derivative of the vector of constraint functions with respect to time.

Differentiating (4.19) with respect to time yields the kinematic equation relating the generalized accelerations:

$$\mathbf{C}_\mathbf{q}\,\ddot{\mathbf{q}} = -\,\mathbf{C}_{tt} - 2\,\mathbf{C}_{\mathbf{q}t}\,\dot{\mathbf{q}} - \left(\mathbf{C}_\mathbf{q}\,\dot{\mathbf{q}}\right)_\mathbf{q}\,\dot{\mathbf{q}} \tag{4.20}$$

with a clear meaning of the subscripts. The right-hand side of (4.20) will be referred to as $\mathbf{Q}_c$ in the following.

4.1.3 Flexible body dynamics

The governing equations for the generic flexible body are derived from Lagrange's equations, which can be expressed as:

$$\frac{d}{dt}\left(\frac{\partial \mathrm{T}}{\partial \dot{\mathbf{q}}}\right)^{\mathrm{T}} - \left(\frac{\partial \mathrm{T}}{\partial \mathbf{q}}\right)^{\mathrm{T}} + \mathbf{C}_\mathbf{q}^{\mathrm{T}}\,\boldsymbol{\lambda} = \mathbf{Q} \tag{4.21}$$

where T is the kinetic energy of the body, $\boldsymbol{\lambda}$ is the vector of *Lagrange multipliers* used to determine the generalized constraint reaction forces $\mathbf{C}_{\mathbf{q}}^{\mathrm{T}}\boldsymbol{\lambda}$, and $\mathbf{Q}$ is the vector of generalized forces, i.e. the forces acting on the body projected onto the generalized coordinates.

In the lumped mass formulation the total mass of the body is distributed among the grid points of the FE model. The kinetic energy associated with node i having a nodal mass m_i and a nodal inertia tensor $\mathbf{I}_i$ is given as:

$$\mathrm{T}_i = \frac{1}{2} m_i \dot{\mathbf{r}}_i^{\mathrm{T}} \dot{\mathbf{r}}_i + \frac{1}{2} \underline{\boldsymbol{\omega}}_i^{\mathrm{T}} \mathbf{I}_i \underline{\boldsymbol{\omega}}_i \tag{4.22}$$

Using (4.12, 4.16) this can be rewritten as:

$$\mathrm{T}_i = \frac{1}{2} \dot{\mathbf{q}}^{\mathrm{T}} \left(m_i \, \mathbf{L}_i^{\mathrm{T}} \, \mathbf{L}_i + \mathbf{N}_i^{\mathrm{T}} \mathbf{I}_i \mathbf{N}_i \right) \dot{\mathbf{q}} \tag{4.23}$$

The kinetic energy of the considered flexible body is evaluated by summing the contributions of all nodes:

$$\mathrm{T} = \frac{1}{2} \dot{\mathbf{q}}^{\mathrm{T}} \left[\sum_i \left(m_i \, \mathbf{L}_i^{\mathrm{T}} \, \mathbf{L}_i + \mathbf{N}_i^{\mathrm{T}} \mathbf{I}_i \mathbf{N}_i \right) \right] \dot{\mathbf{q}} = \frac{1}{2} \dot{\mathbf{q}}^{\mathrm{T}} \, \mathbf{M} \left(\mathbf{q} \right) \, \dot{\mathbf{q}} \tag{4.24}$$

where the mass matrix of the flexible body, $\mathbf{M}\left(\mathbf{q}\right)$, has been introduced; its dependency upon the generalized coordinates is evidenced. An extended definition is obtained by substituting the expressions $\mathbf{L}_i$, $\mathbf{N}_i$ as in (4.12, 4.16), obtaining a symmetric 3×3 block matrix which is synthesized as follows here:

$$\mathbf{M}\left(\mathbf{q}\right) = \begin{bmatrix} \mathbf{M}_{\mathrm{RR}} & \mathbf{M}_{\mathrm{R}\theta} & \mathbf{M}_{\mathrm{R}f} \\ & \mathbf{M}_{\theta\theta} & \mathbf{M}_{\theta f} \\ \mathrm{Sym} & & \mathbf{M}_{ff} \end{bmatrix} \tag{4.25}$$

As usual, the subscripts R, θ and f denote translational, rotational and modal DOF, respectively. The submatrices in (4.25) can be expressed in terms of 9 *inertia invariants* [63], as:

$$\mathbf{M}_{\mathrm{RR}} = \mathcal{I}^1 \mathbf{I} \tag{4.26a}$$

$$\mathbf{M}_{\mathrm{R}\theta} = -\mathbf{A} \left[\widetilde{\mathcal{I}^2 + \mathcal{I}_j^3 q_j} \right] \underline{\mathbf{B}} \tag{4.26b}$$

$$\mathbf{M}_{\mathrm{R}f} = \mathbf{A} \, \mathcal{I}^3 \tag{4.26c}$$

$$\mathbf{M}_{\theta\theta} = \underline{\mathbf{B}}^{\mathrm{T}} \left[\mathcal{I}^7 - \left[\mathcal{I}_j^8 + \mathcal{I}_j^{8\mathrm{T}} \right] q_j - \mathcal{I}_{jk}^9 q_j q_k \right] \underline{\mathbf{B}} \tag{4.26d}$$

$$\mathbf{M}_{\theta f} = \underline{\mathbf{B}}^{\mathrm{T}} \left[\mathcal{I}^4 + \mathcal{I}_j^5 q_j \right] \tag{4.26e}$$

$$\mathbf{M}_{ff} = \mathcal{I}^6 \tag{4.26f}$$

The inertia invariants can be computed in advance by the FE software, based on the information about the nodal masses and inertias, their undeformed locations, and the flexible component modes. In particular, invariants $\mathcal{I}^1$ and $\boldsymbol{\mathcal{I}}^7$ represent the mass and the inertia, respectively, of the flexible body, while invariant $\boldsymbol{\mathcal{I}}^6$ represents the modal mass; disabling this latter causes ADAMS to consider the body as rigid.

By using (4.24), the Lagrange's equations (4.21) can be rewritten as:

$$\mathbf{M}\,\ddot{\mathbf{q}} + \dot{\mathbf{M}}\dot{\mathbf{q}} - \left[\frac{\partial}{\partial \mathbf{q}}\left(\frac{1}{2}\dot{\mathbf{q}}^{\mathrm{T}}\,\mathbf{M}\,\dot{\mathbf{q}}\right)\right]^{\mathrm{T}} + \mathbf{C}_{\mathbf{q}}^{\mathrm{T}}\boldsymbol{\lambda} = \mathbf{Q} \tag{4.27}$$

Collecting the centrifugal and the Coriolis force components into the quadratic velocity vector $\mathbf{Q}_v$, yields:

$$\mathbf{M}\,\ddot{\mathbf{q}} + \mathbf{C}_{\mathbf{q}}^{\mathrm{T}}\boldsymbol{\lambda} = \mathbf{Q} + \mathbf{Q}_v \tag{4.28}$$

Concerning the generalized forces acting on the flexible body, these can be evaluated by considering the associated *virtual work*, due to a virtual displacement in the body generalized coordinates.

The virtual work of the external forces acting on the body can be written as:

$$\delta \mathrm{W}_e = \mathbf{Q}_e^{\mathrm{T}}\delta\mathbf{q} = \begin{bmatrix}\mathbf{Q}_{\mathrm{R}}^{\mathrm{T}} & \mathbf{Q}_{\theta}^{\mathrm{T}} & \mathbf{Q}_f^{\mathrm{T}}\end{bmatrix}\delta\mathbf{q} \tag{4.29}$$

being $\mathbf{Q}_{\mathrm{R}}$ and $\mathbf{Q}_{\theta}$ the generalized forces associated, respectively, with the translational and rotational coordinates of the selected body, while $\mathbf{Q}_f$ is the vector of generalized forces associated with the elastic coordinates of the body. The procedure to obtain such generalized forces is to substitute in the expression of the virtual work associated to the considered action the position vector of its point of application in terms of generalized coordinates.

The virtual work due to the elastic forces can be written as a function of the generalized stiffness matrix associated with the elastic coordinates of the body $\mathbf{K}_{ff}$, as:

$$\delta \mathrm{W}_s = -\,\mathbf{q}_f^{\mathrm{T}}\,\mathbf{K}_{ff}\,\delta\mathbf{q}_f \tag{4.30}$$

Since only the modal coordinates contribute to the elastic energy, the previous can be rewritten as:

$$\delta \mathrm{W}_s = -\begin{bmatrix}\mathbf{R}^{\mathrm{T}} & \boldsymbol{\theta}^{\mathrm{T}} & \mathbf{q}_f^{\mathrm{T}}\end{bmatrix}\begin{bmatrix}\mathbf{0} & \mathbf{0} & \mathbf{0}\\ \mathbf{0} & \mathbf{0} & \mathbf{0}\\ \mathbf{0} & \mathbf{0} & \mathbf{K}_{ff}\end{bmatrix}\begin{Bmatrix}\delta\mathbf{R}\\ \delta\boldsymbol{\theta}\\ \delta\mathbf{q}_f\end{Bmatrix} = -\,\mathbf{q}^{\mathrm{T}}\,\mathbf{K}\,\delta\mathbf{q} \tag{4.31}$$

where the generalized stiffness matrix of the body has been denoted as $\mathbf{K}$.

The virtual work of all forces acting on the body can be written by summing (4.29, 4.31) as:

$$\delta W = \delta W_e + \delta W_s = \mathbf{Q}^T \delta \mathbf{q} \tag{4.32}$$

where the vector of generalized forces has been introduced:

$$\mathbf{Q} = \mathbf{Q}_e - \mathbf{K}\,\mathbf{q} \tag{4.33}$$

Substituting this expression in (4.28) and rearranging, gives the equations of motion of the flexible body:

$$\mathbf{M}\,\ddot{\mathbf{q}} + \mathbf{K}\,\mathbf{q} + \mathbf{C}_\mathbf{q}^T \boldsymbol{\lambda} = \mathbf{Q}_e + \mathbf{Q}_v \tag{4.34}$$

This represents a system of second-order differential equations, whose solution has to satisfy the algebraic constraint equations describing mechanical joints, as well as imposed motions: equations (4.34) and (4.17) form a set of differential-algebraic equations (DAE) that have to be solved simultaneously. A common strategy consists in combining equations (4.20, 4.34), which gives:

$$\begin{bmatrix} \mathbf{M} & \mathbf{C}_\mathbf{q}^T \\ \mathbf{C}_\mathbf{q} & \mathbf{0} \end{bmatrix} \begin{Bmatrix} \ddot{\mathbf{q}} \\ \boldsymbol{\lambda} \end{Bmatrix} = \begin{Bmatrix} \mathbf{Q}_e + \mathbf{Q}_v - \mathbf{K}\,\mathbf{q} \\ \mathbf{Q}_c \end{Bmatrix} \tag{4.35}$$

In general, a closed-form solution of such a system of equations is difficult to obtain, and numerical methods are employed for the purpose. Furthermore, since the constraint equations have been differentiated twice, equation (4.35) satisfies the constraint equations only at the acceleration level, leading to error accumulation in both position and velocity constraints. This problem can be addressed by applying some constraint stabilization method, see e.g. [4], which reduces the violations in the kinematic constraint equations.

A different solution strategy consists in converting the DAE set to ordinary differential equations (ODE), which can be achieved through coordinate partitioning [76, 81], for which a wider choice of numerical integration schemes is available.

4.2 Multibody model assembly

4.2.1 System description

As mentioned, this chapter discusses the development of a multibody model of the cranktrain of a Ducati L-twin, four strokes IC engine, having a displacement of 1.2 litres, capable of delivering 180 horsepower. Figure 4.1 shows a schematic

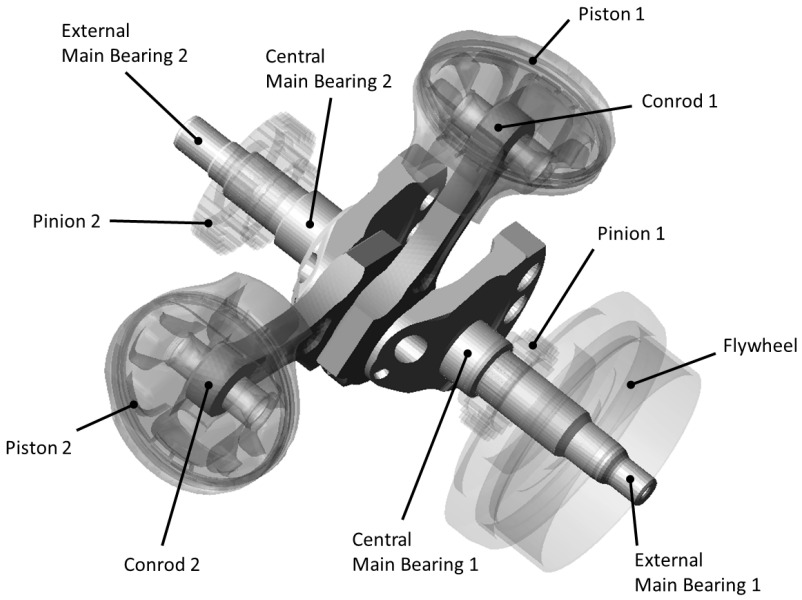

Figure 4.1 The assembled cranktrain model. The flywheel and the two pinions are modelled as concentrated inertias, but they are represented here for reference.

of the mechanism. The main component in the system is a single throw, steel crankshaft supported by four main journals, three of which equipped with ball bearings (the two central ones and the external main bearing 1), the other one with a bush bearing (external main bearing 2). The shaft carries a flywheel, and the two pinions 1 and 2 that transmit power to the valvetrain and the geartrain, respectively. Two titanium alloy connecting rods, arranged in a 90° V configuration, act on the crankpin through hydrodynamically lubricated journal bearings. Wrist pins connect the two pistons to the respective conrods.

Just to provide a clue about the dimensions of the system, it is worth mentioning that the crankshaft length is approximately 300 mm, while the conrod length is about 120 mm. The overall mass of the crankshaft equipped with the flywheel and the two pinions is approximately 7.5 kg, whereas the conrods and the pistons weigh, respectively, 0.35 kg and 0.50 kg each, approximately. Other data cannot be published, being confidential information of the manufacturer.

4.2.2 Preliminary simulations

The first step in the modelling process has been the definition of a multi-rigid-body model of the system, which has been assembled in ADAMS/View.

Both the crankshaft and the connecting rod reduced components, as described in Section 3.2.1, have been imported and assembled by means of kinematic joints. Component flexibility has initially been disabled by disabling the inertia invariant 6, see (4.26), for both parts, in order to debug the initial model by comparing results with those provided by the manufacturer, obtained by means of numerical models based on classical formulations, cf. [5]. It is worth recalling that the crankshaft FE model includes the flywheel and the two pinions, modelled as lumped inertias, as well as the balancing pads; in a similar way, the connecting rod FE model is equipped with the big end bearing shells and the small end bush, along with the two screws holding the bearing cap.

Both pistons, and the related wrist pins, have been imported as CAD data; proper density values have been assigned to those components, in order for their inertial properties to be correctly described.

Great care has been taken to build a single DOF system: joints and joint primitives were arranged with such purpose, preventing the software to detect, and remove, any redundant constraints. In particular, a `spherical` joint and an `inline` joint primitive have been employed to restrain the crankshaft at both central main bearings, while `cylindrical` joints have been used at the crankshaft-conrod interfaces.

Model inputs are the combustion forces acting on both pistons, see Figure 4.2, resulting from an experimental test campaign, and the torques acting on the two pinions driving the valvetrain and the geartrain: the former was estimated by the manufacturer by means of some numerical model of the valvetrain, while the latter was obtained by simply enforcing periodic speed oscillations over the engine cycle. All these data have been imported into ADAMS and converted to continuous, periodic functions of the crank angle, through the `spline` element; these functions are referenced by `sforce` elements, for the combustion forces applied to both pistons, and `gforce` elements, for the torques, and the associated forces, applied to the crankshaft.

The dynamic simulations have been performed by initially applying a kinematic constraint to the crankshaft, via the `motion` element, making its angular velocity rise smoothly from zero to the rated value of 10,000 rpm. Such constraint, introduced in order to avoid numerical instability issues at the beginning of the simulation, is disabled after few cycles, and from this time on the system is driven by the applied forces and torques.

Estimates of the loads acting on both the connecting rod and the crankshaft were retrieved as a result of this first dynamic model, and compared to those provided by the manufacturer and employed in the design phase, confirming an appropriate model setup.

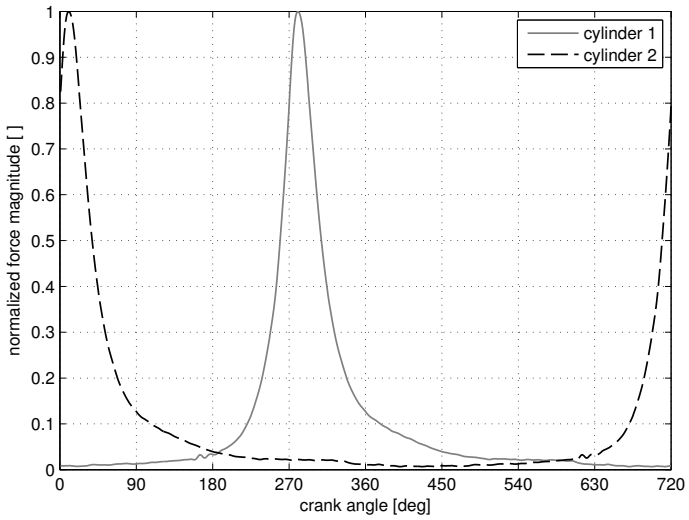

Figure 4.2 Combustion force magnitudes acting on the two pistons. Values are normalized for confidentiality reasons.

The described model, which will be referred as *model 0* in the following, shows some evident limitations. Firstly, loads at two out of four main bearing locations cannot be evaluated, since static indeterminacy of the assembly cannot be treated with a purely kinematic approach: the constraints associated with the external main bearings have therefore been ignored. Secondly, the elastodynamic effects, which might have a major impact on the estimated loads, provided the high rotational speed of the engine, are completely neglected.

These drawbacks can be removed by introducing non-ideal joints at the main interface locations, and by modelling component flexibility. Both procedures concur towards the definition of a more realistic model, which should be capable of predicting the interactions between the components in the system with improved accuracy, and have been exploited in the present study.

4.3 Multibody simulations

4.3.1 Model implementation

The discussed bearing models, see Chapter 2, have been included to describe the main bearing and big end bearing dynamics.

Ball bearings at main bearing locations have been modelled through `field`

elements, referencing the described `fiesub` Fortran subroutine, acting between the flexible crankshaft and the ground; each of those employs a set of bearing-specific parameters, which have been retrieved from the manufacturer. In particular, two angular contact bearings, featuring a contact angle of 15°, are employed at central main bearings, while a single-row radial bearing is used at the external main bearing 1: this has been modelled by exploiting the same `fiesub` subroutine, by simply setting up a value of 0° for the contact angle. The same radial bearing model has been employed at the external main bearing 2, as well, in order to prevent the adoption of any contact model, at the same time removing the need for a purely kinematic joint.

Journal bearings at big end bearing locations have been modelled via `gforce` elements, referencing the illustrated `gfosub` Fortran subroutine. Since both components linked by such elements, i.e. the crankshaft and the connecting rod, have been defined as flexible, and provided that the reaction force from a `gforce` element cannot act on a flexible body, two massless links[1] have been introduced, connected to the conrods with fixed joints, and used as reaction-force bodies for the definition of the bearing elements. Again, the journal bearing model employs a set of user-parameters, some of which have been directly provided by

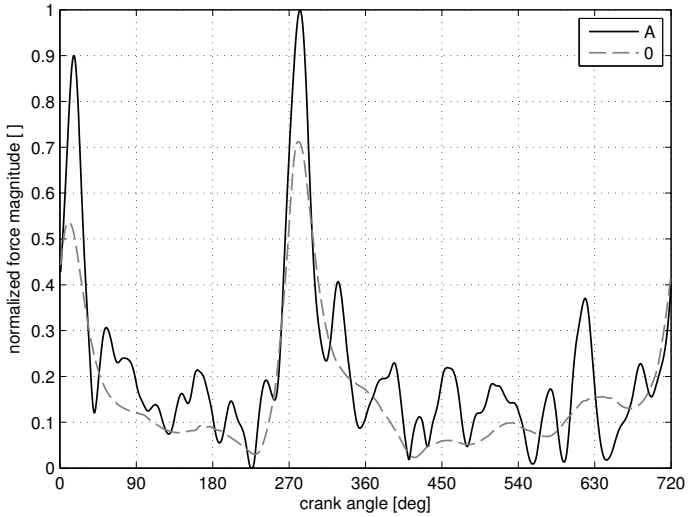

Figure 4.3 Force magnitude at the central main bearing 1 as computed for model A and model 0, normalized over the peak load value of model A.

[1] A massless link, also called a dummy body, is a link with zero or an insignificant amount of both mass and inertia, which can be used to facilitate the creation of a model.

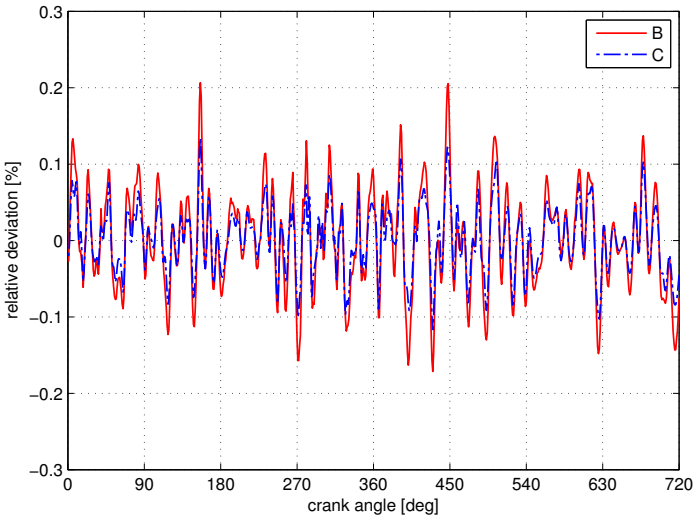

(a)

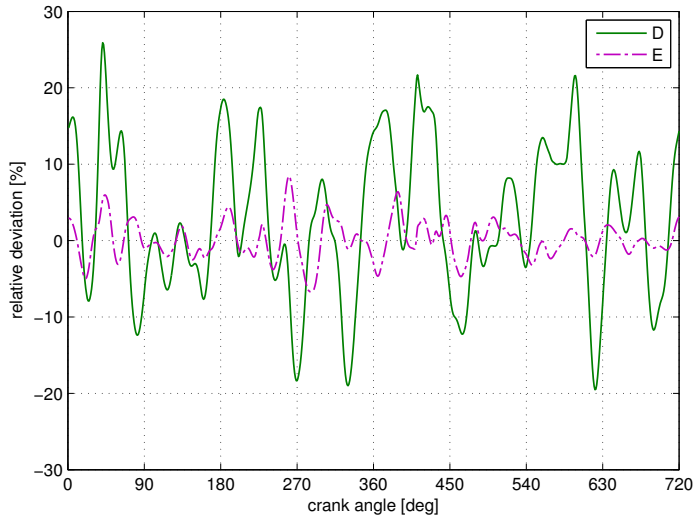

(b)

Figure 4.4 Deviations exhibited by models B, C (a) and D, E (b) relative to model A, concerning the reaction force evaluated at the central main bearing 1.

the manufacturer. It is worth recalling that the implemented model is a 2-DOF, purely radial model: an `inplane` joint primitive has therefore been defined for each big end bearing in order to prevent any relative axial displacement between

the conrods and the crankshaft, removing the need of adopting any contact models.

As a further step, component flexibility for both the crankshaft and the connecting rod reduced models has been enabled. With this respect, a partial coupling formulation has been employed, consisting in disabling inertia invariants 5 and 9, cf. (4.26). These provide a second-order correction to the flexible body inertia tensor, and impose the greatest computational overhead on the evaluation of the flexible body equations of motion: in most cases, disabling them reduces CPU time significantly while having minor impact on the results. Note that ADAMS/Flex disables inertia invariants 3 and 4 by default, being their magnitudes small in most situations; since non-standard procedures for model reduction have been implemented in the present work, these invariants have been enabled using a customized invariant formulation.

The substitution of the ideal, kinematic joints with the described bearing models, along with the introduction of the flexibility of the main components in the system, revealed a dramatic impact on the dynamics of the cranktrain. As an example, Figures 4.3, 4.5 compare the reaction forces acting on the central main bearing 1 and on the big end bearing 1, respectively, of such complete model, denoted as model A in the following sections, with those retrieved from the dynamic simulations performed onto model 0: considerable differences show up, with peaks well above 30%, demonstrating that the adopted modelling strategies are crucial for the present application.

4.3.2 Simulation results

The performances of the proposed model reduction techniques have been evaluated by simulating several versions of the described cranktrain model. A reference model, denoted as *model A*, has been obtained by including those crankshaft and connecting rod models denoted as A_s and A_r, respectively, in Section 3.3, both retaining 80 normal modes sorted by increasing frequency in the related CB reduced representations. In the same manner, a *model B* has been built incorporating models B_s and B_r of Section 3.3, related to the crankshaft and the conrod respectively, which were obtained by retaining those normal modes holding the highest EIM values allowing to hit the target of 90% of dynamic completeness in terms of EIM cumulative sum: this resulted in the selection of 18 eigenmodes for the crankshaft and 42 eigenmodes for the conrod. A *model C* has been generated, as well, including crankshaft model C_s and conrod model C_r, cf. Section 3.3, having the same model order as B_s and B_r, respectively, but including a number of MTVs, 6 for the crankshaft and 12 for the conrod, in the reduced representations.

In order to provide some terms of comparison, two additional models were developed by following a different approach for component model reduction: starting from those employed in model A, the crankshaft and conrod reduced models were obtained in this case by truncating their corresponding orthogonalized CB representations, see Section 3.2.2, at a certain cut-off frequency, according to a practice which is commonly used by multibody dynamics analysts. The frequency cut-off value has been set at 20 kHz in one case, at 30 kHz in the other, obtaining the models which will be referred to as *model D* and *model E*, respectively, in the remainder. It should be noted that a dynamic completeness level expressed in terms of EIM cumulative sum cannot be computed in these cases, since truncation acts directly onto the orthogonalized CB mode set.

It is worth stressing that models A through E are identical to each other, except for the reduced flexible crankshaft and connecting rod models they integrate; model features are summarized in Table 4.1.

Estimates of the loads acting on the connecting rods and the crankshaft were retrieved as a first result of the simulations. Relative deviations were evaluated for models B through E with respect to model A over a mean engine cycle, i.e. two crankshaft full revolutions, obtained by averaging 10 consecutive cycles extracted after the transient initialization effects have properly faded. In each case these errors were normalized based upon the peak load value as estimated for model A, in order to assign a lower importance to deviations occurring at low magnitudes.

As an example, Figure 4.3 shows the normalized force magnitude acting on the central main bearing 1, as evaluated for model A. The relative deviations exhibited by models B through E are shown in Figure 4.4. As for models B and C, these deviations are very small, keeping well below 1% in both cases; concerning

Model		A	B	C	D	E	F	G
crankshaft	orth. modes	128	66	66	128	128	57	57
	cut-off [kHz]	-	-	-	20	30	-	-
	active modes	122	60	60	38	59	51	51
conrod	orth. modes	92	54	54	92	92	35	35
	cut-off [kHz]	-	-	-	20	30	-	-
	active modes	86	48	48	14	27	29	29
cranktrain	active modes	294	156	156	66	113	109	109

Table 4.1 Number of active modes in the simulated multibody models. Note that embedded in the orthogonalized CB modes are 6 rigid-body modes, which need to be removed since ADAMS provides its own large-motion DOFs.

this particular result, model C seems to be slightly superior to model B. On the other hand, it looks evident that models D, E perform much worse than models B, C, actually exhibiting considerable deviations from the reference; as expected, deviations associated to model E are smaller than those related to model D. Looking at the peak load values, these are perfectly captured by models B, C, with errors having an order of magnitude of 0.1%, while they are significantly misestimated by models D, E. It is worth mentioning that these are essential input data for a proper design of components subjected to dynamic loads.

In a similar fashion, Figures 4.5, 4.6 show the normalized force magnitude computed for model A at the big end bearing 1 and the normalized deviations exhibited by models B through E, respectively. Once again, while the differences between models B, C and model A are very small, and less than 1%, models D, E reveal substantial deviations from the reference.

Similar results hold for the loads acting at other interface locations, as well: the RMS value of the relative percentage deviation was used here as a simple and effective metrics to measure the result accuracy of models B through E with respect to the reference model A. Table 4.2 sums up these values, concerning the reaction forces at the crankshaft and conrod interface locations.

Clearly, models B, C outperform models D, E, resulting in all cases closer to model A, which in turn involves a more complete flexible component description

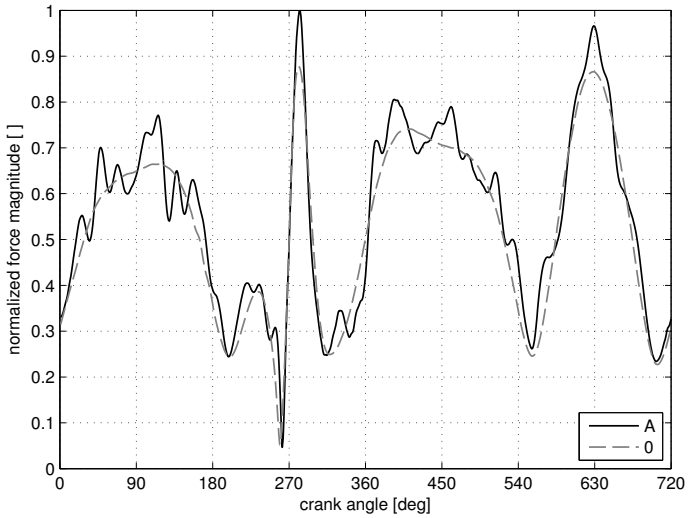

Figure 4.5 Force magnitude at the big end bearing 1 as computed for model A and model 0, normalized over the peak load value of model A.

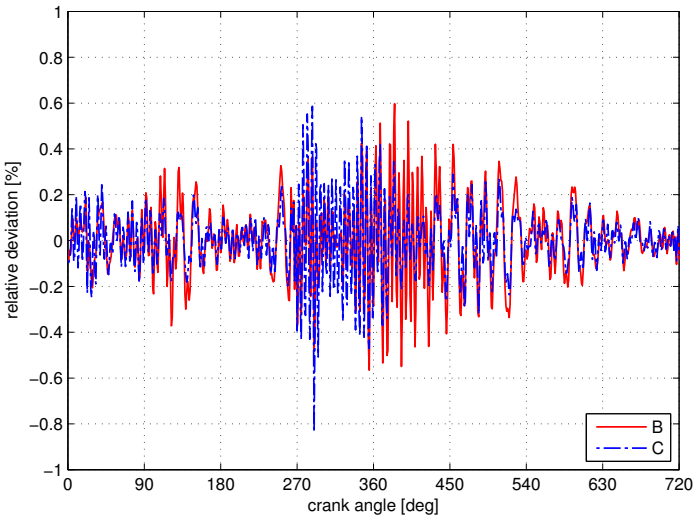

(a)

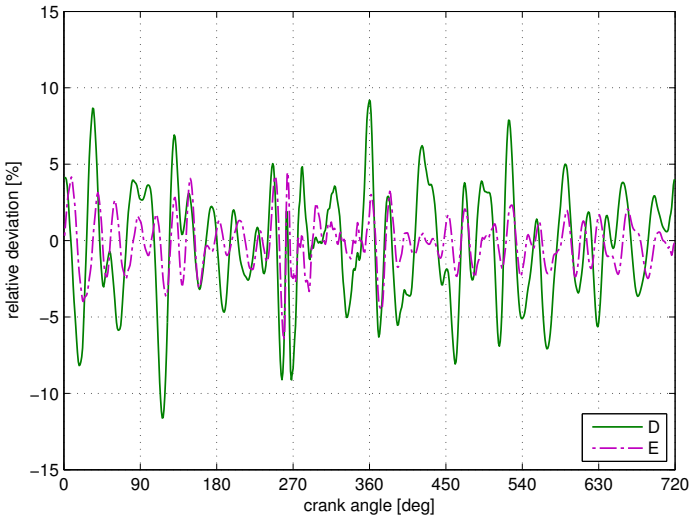

(b)

Figure 4.6 Deviations exhibited by models B, C (a) and D, E (b) relative to model A, concerning the reaction force evaluated at the big end bearing 1.

and as such is supposed to better represent the real behaviour of the system. It should be noted that, for all the models, the largest errors are those related to loads acting on the external main bearings, which likely present a greater

sensitivity to high frequency dynamic effects than the other interface locations.

In addition to the interface forces, some kinematic results were investigated in order to further evaluate the performance of the adopted model reduction schemes. Figure 4.7 shows the normalized minimum oil film thickness experienced at big end bearing 1 as computed for model A, while Figure 4.8 shows the relative deviations related to models B through E: analogous conclusions to those withdrawn so far can be extracted. A similar trend showed up for all the inspected kinematic quantities.

In order to further assess the performances of the proposed component model reduction techniques, two more multibody models were produced in the same fashion as models B and C. A first model has been obtained by setting a threshold of cumulative EIM sum at 75% for both the reduced crankshaft and connecting rod models: that still appears to be a reasonable level of dynamic completeness, at the same time being significantly lower than that used so far, thus appearing suitable for a consistent results comparison. Such a model, that will be referred to as *model F* in the following, includes 9 and 23 normal modes for the crankshaft and conrod models, respectively. A second cranktrain model, having the same model order, has been built and simulated: such model, denoted as *model G*, includes 6 normal modes plus 3 MTVs for the crankshaft, and 11 normal modes plus 12 MTVs for the connecting rod. Features of models F, G are reported in Table 4.1.

Estimates of the interface loads, as well as bearing kinematic quantities, were evaluated for both models, and relative deviations were computed with respect to model A in the same manner described above; in particular, the RMS values of the relative deviations concerning the loads at the interface locations of interest are reported in Table 4.2. As expected, model F and model G exhibit a poorer

Model	B	C	D	E	F	G
Central main bearing 1	0.06	0.04	10.1	2.5	1.9	1.8
Central main bearing 2	0.09	0.06	9.8	3.0	1.7	1.6
External main bearing 1	0.13	0.10	23.8	5.8	4.6	4.5
External main bearing 2	0.53	0.34	19.4	8.4	5.7	5.5
Conrod 1 big end	0.16	0.14	3.8	1.7	1.3	1.3
Conrod 1 small end	0.09	0.06	2.2	1.1	1.0	0.9
Conrod 2 big end	0.15	0.15	3.0	1.4	1.4	1.4
Conrod 2 small end	0.08	0.05	1.7	1.0	1.1	1.1

Table 4.2 RMS values of the relative percentage deviations, computed for models B through G with respect to model A, concerning load magnitudes at the crankshaft and conrod interfaces.

accuracy with respect to models B and C, respectively, in virtue of the lower dynamic completeness associated with the featured flexible members. Compared to models D and E, however, they show a higher precision, which is particularly evident when considering the main bearing deviations.

Concerning computational cost, Table 4.3 reports the CPU time required by the simulations involving models B through G, normalized with respect to model A: this latter results to be much heavier with respect to the other models simulated here, the reason being the large modal basis associated with the flexible components it incorporates. For the sake of completeness, it is worth mentioning that simulations have been performed using the stabilized-index-two `GSTIFF` integrator [32, 33, 34], available in ADAMS/Solver.

4.3.3 Discussion

In most cases, a model including a large number of modes, as the reference model A herein, might result too expensive for a practical use in the design process, where the requirement of optimized component design paralleled with the need of meeting tight deadlines calls for efficient simulation models.

Simulation efficiency is the principal motivation behind the commonly used practice consisting in truncating the modal basis of the components of interest according to an arbitrary cut-off frequency: models D, E were obtained by adopting such approach for both the crankshaft and the connecting rod flexible models. Results show that the chosen cut-off frequency heavily affects accuracy, which represents the other major requirement a simulation model should satisfy. A good dose of experience is required to properly choose such parameter, allowing the analyst to be confident in the results of his simulations; this might not always be the case, especially for components and/or systems he might not be familiar with.

The EIM-based approach, adopted here to obtain models B and F, allows overcoming these drawbacks: relying on a quantitative assessment of the dynamic completeness of a reduced representation of the flexible bodies at issue, it directly provides an indication of model effectiveness, referring in particular to the capability in predicting accurate interface loads. This represents a major

Model	B	C	D	E	F	G
Normalized CPU time	0.37	0.23	0.12	0.17	0.27	0.16

Table 4.3 Normalized CPU time required by the simulated models B through G, computed with respect to model A.

advantage over the more traditional truncation-based approach: a guideline for the normal modes selection is delivered, providing a direct insight on the reduced component performance prior to the multibody simulation phase.

Of course, engineering judgement must still play an important part in the process, particularly when defining the target levels of EIM dynamic completeness of the involved flexible components: this has an important impact on the multibody model performance, as evidenced by comparing results related to models B and F. These include flexible reduced components associated to dynamic completeness levels of 90% and 75%, respectively, in terms of EIM cumulative sum: the former one provides very accurate results, while the latter results in fairly good accuracy combined with a shorter simulation time.

It is worth emphasizing that the importance of the elastodynamic behaviour of different components on the global system dynamics is different, so that the experienced analyst might decide to set a high level of dynamic completeness for the dominant members, and a lower level for the less contributing ones, thus achieving the better compromise between accuracy and computational cost.

Concerning this aspect, the usage of MTVs appears to be advantageous for the present application case, providing comparable result accuracy with reduced computational overhead when compared to the method based upon

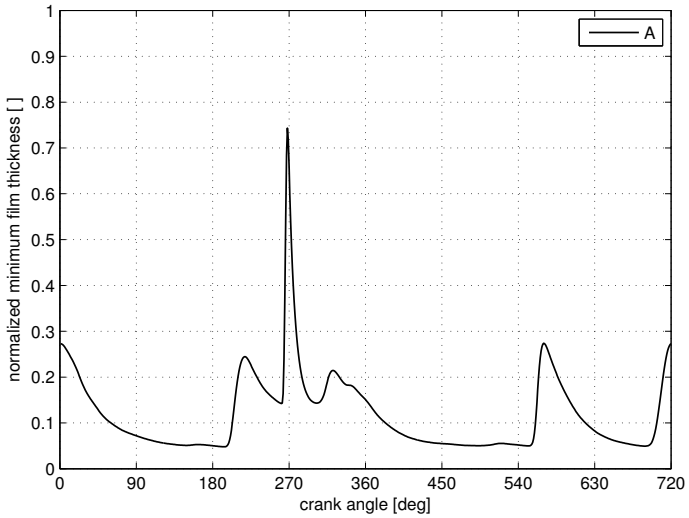

Figure 4.7 Minimum oil film thickness, normalized over radial clearance, at the big end bearing 1. Such quantity cannot be evaluated for model 0, since the bearing is modelled as a cylindrical kinematic joint in that case.

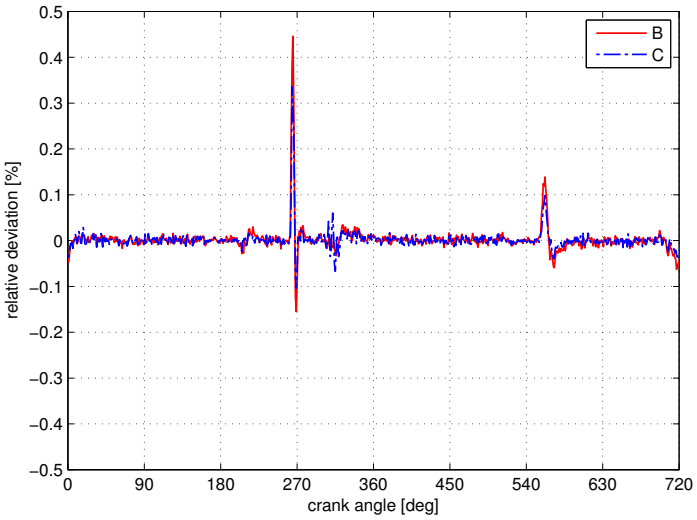

(a)

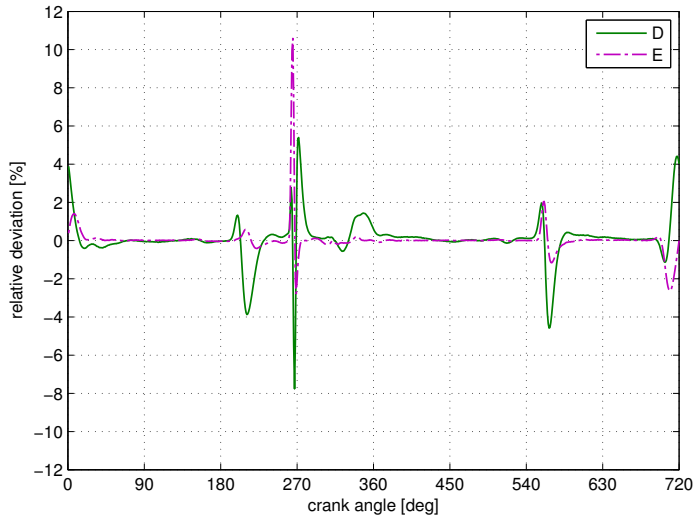

(b)

Figure 4.8 Deviations exhibited by models B, C (a) and D, E (b) relative to model A, concerning the minimum oil film thickness evaluated at the big end bearing 1.

EIM, cf. Tables 4.2, 4.3. With respect to this latter, however, no information about the number of modes to include in the reduced representations of the flexible components is provided, so that the mentioned advantages might result partly

compromised.

This is not the case if, as shown in the present study, the MTA technique is combined with the EIM concept: the latter can be used to define how many normal modes, and possibly which ones, should be retained in order to reach a specified level of dynamic completeness for the considered flexible component; a number of normal modes, potentially those associated to the highest frequencies, may then be replaced with an equal number of MTVs, which compensate the effects of modal truncation with improved efficiency.

Chapter 5

Conclusions

The development of a flexible multibody model of a motorcycle engine cranktrain has been presented in this thesis, with a particular emphasis on the adopted component model reduction methods.

5.1 Main contributions

Two bearing models, one concerning angular contact ball bearings, the other referring to hydrodynamic bearings, have been implemented starting from available literature descriptions, in order to properly capture the dynamic behaviour of the main connections in the system under study, i.e. the crankshaft main bearings and the connecting rod big end bearings. Both the theoretical background of the models and the details about their specific implementation as computational routines within the adopted multibody simulation software have been provided.

Two techniques for model reduction, operating onto the well-established Craig-Bampton methodology, have been implemented: the Effective Interface Mass (EIM) concept provides a useful guideline for the *selection* of component normal modes to include in a reduced representation based upon their contribution to the dynamic loads at the interface, while the Modal Truncation Augmentation (MTA) approach alleviates the effects of modal *truncation* by enriching the reduction basis with pseudo-eigenvectors without affecting the topology of the reduced model. After a concise theoretical overview about these methods, the procedure adopted to obtain reduced representations of both the crankshaft and the connecting rod has been described in detail, with an explanation of the reduction routines which have been implemented within the adopted Finite Element code. The obtained reduced models have been subjected

to numerical testing against reference models, before the multibody simulation phase, in order to asses the performance of the adopted techniques. Standard frequency response and modal correlation criteria have been used for the purpose, showing that both methods lead to more accurate models when compared with the standard Craig-Bampton reduction scheme, provided the same model order.

A multibody model devoted to the dynamic simulation of a motorcycle engine cranktrain has eventually been produced. The first step in the process has consisted in the definition of a system made up of rigid links connected to each other via kinematic joints; the main limitations of such model have been discussed, and overtaken by introducing both the mentioned bearing models and the flexible reduced crankshaft and conrod models. With this respect, a brief theoretical overview about the Floating Frame of Reference formulation for the description of flexible multibody systems is presented. The performances of the proposed reduction techniques have been further evaluated by comparing several versions of the cranktrain model: dynamic simulations prove that model reduction based on EIM leads to more accurate results with respect to the traditional frequency-based truncation approach, provided that a consistent level of dynamic completeness is chosen for each flexible reduced component in the system; the MTA method provides the same high-level of results accuracy, given the same model order, bringing in this case a further advantage in terms of computational cost of the simulations.

5.2 Future research

Some recommendations for future research on the presented subjects is provided in the following.

Regarding the application of the EIM approach, some strategy to identify in a systematic fashion appropriate levels of dynamic completeness for the reduction of the components used for multibody system simulation would be beneficial, especially concerning computational efficiency aspects.

Concerning the application of the MTA method, the definition of some interface reduction technique would result in a more efficient and systematic way for the identification of the pseudo-eigenvectors needed to complement the Craig-Bampton reduced representation of flexible components, especially for those characterized by a large number of interface nodes.

With reference to both model reduction techniques, a common implementation of the described Finite Element routines would make the advantages of both methods directly available for the analyst who wishes to include optimal reduced flexible component models in his multibody simulations.

Concerning the assessment of the adopted model reduction techniques, on the multibody simulation side, a further step consists in the evaluation of the stresses experienced by the flexible components in the system, which should be accomplished in order to extend the performance evaluation of the proposed methodologies.

With regard to the particular application, the cranktrain multibody model should be complemented by integrating a reduced flexible model of the engine block, in order to provide a more complete simulation platform for design optimization, concerning both durability and NVH issues.

Bibliography

[1] R.J. Allemang and D.L. Brown. A correlation coefficient for modal vector analysis. In *Proceedings of the 1st International Modal Analysis Conference*, volume 1, pages 110–116. SEM, Orlando, 1982.

[2] S. Andréason. Load distribution in a taper roller bearing arrangement considering misalignment. *Tribology*, 6(3):84–92, 1973.

[3] J.F. Antoine, G. Abba, and A. Molinari. A new proposal for explicit angle calculation in angular contact ball bearing. *Journal of Mechanical Design*, 128(2):468–478, 2006.

[4] J. Baumgarte. Stabilization of constraints and integrals of motion in dynamical systems. *Computer Methods In Applied Mechanics And Engineering*, 1(1):1–16, 1972.

[5] Giuseppe Bocchi. *Motori a quattro tempi*. Hoepli Editore, 1987.

[6] D. Bonneau, D. Guines, J. Frêne, and J. Toplosky. EHD analysis, including structural inertia effects and a mass-conserving cavitation model. *Journal of Tribology*, 117(3):540–547, 1995.

[7] J.F. Booker. Dynamically loaded journal bearings: mobility method of solution. *Journal of Basic Engineering*, 87:537, 1965.

[8] J.F. Booker. Dynamically-loaded journal bearings: numerical application of the mobility method. *Journal of Lubrication Technology*, 93:168, 1971.

[9] J.F. Booker and K.H. Huebner. Application of finite element methods to lubrication: an engineering approach. *Journal of Lubrication Technology*, 94:313, 1972.

[10] A. Boysal and H. Rahnejat. Torsional vibration analysis of a multi-body single cylinder internal combustion engine model. *Applied Mathematical Modelling*, 21(8):481–493, 1997.

[11] K.E. Brenan, S.L.V. Campbell, and L.R. Petzold. *Numerical solution of initial-value problems in differential-algebraic equations*. Society for Industrial and Applied Mathematics Philadelphia, 1996.

[12] S. Bukovnik, N. Dörr, V. Čaika, W.J. Bartz, and B. Loibnegger. Analysis of diverse simulation models for combustion engine journal bearings and the influence of oil condition. *Tribology International*, 39(8):820–826, 2006.

[13] Y. Cao and Y. Altintas. A general method for the modeling of spindle-bearing systems. *Journal of Mechanical Design*, 126(6):1089–1104, 2004.

[14] N.G. Chalhoub, H. Nehme, N.A. Henein, and W. Bryzik. Effects of structural deformations of the crank-slider mechanism on the estimation of the instantaneous engine friction torque. *Journal of Sound and Vibration*, 224(3):489–503, 1999.

[15] D. Childs, H. Moes, and H. van Leeuwen. Journal bearing impedance descriptions for rotordynamic applications. *Journal of Lubrication Technology*, 99:198, 1977.

[16] R.R. Craig. A review of time-domain and frequency domain component-mode synthesis methods. *Modal Analysis: The International Journal of Analytical and Experimental Modal Analysis*, 2(2):59–72, 1987.

[17] R.R. Craig. Coupling of substructures for dynamic analyses: an overview. In *Proceedings of the 41st AIAA/ASME/ASCE/AHS/ASC Structures, Structural Dynamics and Materials Conference*, Atlanta, 2000.

[18] R.R. Craig and M.C.C. Bampton. Coupling of substructures for dynamic analyses. *AIAA Journal*, 6(7):1313–1319, 1968.

[19] R.R. Craig and A.J. Kurdila. *Fundamentals of structural dynamics*. Wiley, 2006.

[20] J.M. De Mul, J.M. Vree, and D.A. Maas. Equilibrium and associated load distribution in ball and roller bearings loaded in five degrees of freedom while neglecting friction. I: General theory and application to ball bearings. II: Application to roller bearings and experimental verification. *Journal of Tribology*, 111(1):142–155, 1989.

[21] J.M. Dickens, J.M. Nakagawa, and M.J. Wittbrodt. A critique of mode acceleration and modal truncation augmentation methods for modal response analysis. *Computers & Structures*, 62(6):985–998, 1997.

[22] J.M. Dickens and K.V. Pool. Modal truncation vectors and periodic time domain analysis applied to a cyclic symmetry structure. *Computers & Structures*, 45(4):685–696, 1992.

[23] J.M. Dickens and A. Stroeve. Modal truncation vectors for reduced dynamic substructure models. In *Proceedings of the 41st AIAA/ASME/ ASCE/AHS/ASC Structures, Structural Dynamics and Materials Conference*, Atlanta, 2000.

[24] C.B. Drab, H.W. Engl, J.R. Haslinger, G. Offner, R.U. Pfau, and W. Zulehner. Dynamic simulation of crankshaft multibody systems. *Multibody System Dynamics*, 22(2):133–144, 2009.

[25] C.B. Drab, J.R. Haslinger, R.U. Pfau, and G. Offner. Comparison of the classical formulation with the reference conditions formulation for dynamic flexible multibody systems. *Journal of Computational and Nonlinear Dynamics*, 2(4):337–343, 2007.

[26] I.H.Y. Du. Simulation of flexible rotating crankshaft with flexible engine block and hydrodynamic bearings for a V6 engine. *SAE Technical Paper*, 108(3):1852–1860, 1999.

[27] O. Ebrat, Z.P. Mourelatos, H. Kexin, N. Vlahopoulos, and K. Vaidyanathan. An elastohydrodynamic coupling of a rotating crankshaft and a flexible engine block. *Journal of Tribology*, 126(2):233–241, 2004.

[28] H. Elmqvist, S.E. Mattsson, H. Olsson, J. Andreasson, M. Otter, C. Schweiger, and D. Brück. Realtime simulation of detailed vehicle and powertrain dynamics. *SAE Technical Paper*, pages 63–76, 2004.

[29] P. Flores, J. Ambrósio, and J.P. Claro. Dynamic analysis for planar multibody mechanical systems with lubricated joints. *Multibody System Dynamics*, 12(1):47–74, 2004.

[30] P. Flores, J. Ambrósio, J.P. Claro, and H.M. Lankarani. *Kinematics and dynamics of multibody systems with imperfect joints: models and case studies*, volume 34. Springer, 2008.

[31] S.H.J.A. Fransen. Data recovery methodologies for reduced dynamic substructure models with internal loads. *AIAA journal*, 42(10):2130–2142, 2004.

[32] C.W. Gear. *Numerical initial value problems in ordinary differential equations*. Prentice Hall PTR, 1971.

[33] C.W. Gear. Simultaneous numerical solution of differential-algebraic equations. *IEEE Transactions on Circuit Theory*, 18(1):89–95, 1971.

[34] C.W. Gear, B. Leimkuhler, and G.K. Gupta. Automatic integration of Euler-Lagrange equations with constraints. *Journal of Computational and Applied Mathematics*, 12:77–90, 1985.

[35] P.K. Goenka. Analytical curve fits for solution parameters of dynamically loaded journal bearings. *Journal of Tribology*, 106:421–428, 1984.

[36] P.K. Goenka, F.A. Martin, P.E. Allaire, J.F. Booker, and G.A. La Bouff. Dynamically loaded journal bearings: finite element method analysis. *Journal of Tribology*, 106(4):429–437, 1984.

[37] C.Z. Gregory. Reduction of large flexible spacecraft models using internal balancing theory. *Journal of Guidance, Control, and Dynamics*, 7:725–732, 1984.

[38] R.J. Guyan. Reduction of stiffness and mass matrices. *AIAA Journal*, 3(2):380, 1965.

[39] T.A. Harris and M.N. Kotzalas. *Rolling bearing analysis*. CRC/Taylor & Francis, 2007.

[40] G.H.K. Heirman and W. Desmet. Interface reduction of flexible bodies for efficient modeling of body flexibility in multibody dynamics. *Multibody System Dynamics*, 24(2):219–234, 2010.

[41] X. Hernot, M. Sartor, and J. Guillot. Calculation of the stiffness matrix of angular contact ball bearings by using the analytical approach. *Journal of Mechanical Design*, 122(1):83–90, 2000.

[42] D.N. Herting. A general purpose, multi-stage, component modal synthesis method. *Finite Elements in Analysis and Design*, 1(2):153–164, 1985.

[43] W. Heylen and S. Lammens. FRAC: A consistent way of comparing frequency response functions. In *Proceedings of the Conference on Identification in Engineering Systems*, pages 48–57, 1996.

[44] W. Heylen, S. Lammens, and P. Sas. *Modal analysis theory and testing*. Katholieke Universiteit Leuven, Departement Werktuigkunde, 1997.

[45] R.M. Hintz. Analytical methods in component modal synthesis. *AIAA Journal*, 13(8):1007–1016, 1975.

[46] H. Hirani, K. Athre, and S. Biswas. Dynamically loaded finite length journal bearings: analytical method of solution. *Journal of Tribology*, 121(4):844–852, 1999.

[47] D.M.W. Hoffman and D.R. Dowling. Fully coupled rigid internal combustion engine dynamics and vibration - Part I: model development. *Journal of Engineering for Gas Turbines and Power*, 123(3):677–684, 2001.

[48] L. Houpert. Prediction of bearing, gear and housing performances. In *Proceeding of the Rolling Bearing Practice Today Seminar*. I. Mech. E., London, 1995.

[49] L. Houpert. A uniform analytical approach for ball and roller bearings calculations. *Journal of Tribology*, 119(4):851–858, 1997.

[50] W.C. Hurty. Dynamic analysis of structural systems using component modes. *AIAA Journal*, 3(4):678–685, 1965.

[51] A.B. Jones. A general theory for elastically constrained ball and radial roller bearings under arbitrary load and speed conditions. *Journal of Basic Engineering*, 82:309, 1960.

[52] D.C. Kammer, J. Cessna, and A. Kostuch. An Effective Mass measure for selecting free-free target modes. In *Proceedings of the 23rd International Modal Analysis Conference*, Orlando, Florida, 2005.

[53] D.C. Kammer, J. Cessna, and A. Kostuch. A generalization of Effective Mass for selecting free-free target modes. *Journal of Vibration and Acoustics*, 129(1):121–127, 2007.

[54] D.C. Kammer and M.J. Triller. Ranking the dynamic importance of fixed interface modes using a generalization of Effective Mass. *Modal Analysis: The International Journal of Analytical and Experimental Modal Analysis*, 9(2):77–98, 1994.

[55] D.C. Kammer and M.J. Triller. Selection of component modes for Craig-Bampton substructure representations. *Journal of Vibration and Acoustics*, 118(2):264–270, 1996.

[56] A. Kumar and J.F. Booker. A finite element cavitation algorithm. *Journal of Tribology*, 113(2):276–286, 1991.

[57] A. Kumar, J.F. Booker, and P.K. Goenka. Dynamically loaded journal bearings: a modal approach to EHL design analysis. *Tribological Design of Machine Elements*, pages 305–315, 1989.

[58] M. Kushwaha, S. Gupta, P. Kelly, and H. Rahnejat. Elasto-multi-body dynamics of a multicylinder internal combustion engine. *Proceedings of the Institution of Mechanical Engineers, Part K: Journal of Multi-body Dynamics*, 216(4):281–293, 2002.

[59] N.T. Liao and J.F. Lin. A new method for the analysis of deformation and load in a ball bearing with variable contact angle. *Journal of Mechanical Design*, 123(2):304–312, 2001.

[60] T.C. Lim and R. Singh. Vibration transmission through rolling element bearings - Part I: bearing stiffness formulation. *Journal of Sound and Vibration*, 139(2):179–199, 1990.

[61] Z.D Ma and N.C. Perkins. An efficient multibody dynamics model for internal combustion engine systems. *Multibody System Dynamics*, 10(4):363–391, 2003.

[62] R.H. MacNeal. A hybrid method of component mode synthesis. *Computers & Structures*, 1(4):581–601, 1971.

[63] The MacNeal-Schwendler Corporation. *ADAMS/Flex online help*.

[64] The MacNeal-Schwendler Corporation. *MSC NASTRAN Reference Manual, version 2004*.

[65] H. Moes. Discussion on a contribution by K. Jakobsen and H. Christensen, Tribology Convention, Gothenburg. *Proc. Instn. Mech. Engrs*, 183:205–206, 1969.

[66] F.H. Montazersadgh and A. Fatemi. Dynamic load and stress analysis of a crankshaft. *SAE Technical Paper*, 258, 2007.

[67] B.C. Moore. Principal component analysis in linear systems: Controllability, observability, and model reduction. *IEEE Transactions on Automatic Control*, 26(1):17–32, 1981.

[68] Z.P. Mourelatos. An efficient crankshaft dynamic analysis using substructuring with Ritz vectors. *Journal of Sound and Vibration*, 238(3):495–527, 2000.

[69] Z.P. Mourelatos. A crankshaft system model for structural dynamic analysis of internal combustion engines. *Computers & Structures*, 79(20):2009–2027, 2001.

[70] G. Offner, J. Krasser, O. Laback, and H.H. Priebsch. Simulation of multi-body dynamics and elastohydrodynamic excitation in engines especially considering piston-liner contact. *Proceedings of the Institution of Mechanical Engineers, Part K: Journal of Multi-body Dynamics*, 215(2):93–102, 2001.

[71] M.S.M. Perera, S. Theodossiades, and H. Rahnejat. A multi-physics multi-scale approach in engine design analysis. *Proceedings of the Institution of Mechanical Engineers, Part K: Journal of Multi-body Dynamics*, 221(3):335–348, 2007.

[72] M.S.M. Perera, S. Theodossiades, and H. Rahnejat. Elasto-multi-body dynamics of internal combustion engines with tribological conjunctions. *Proceedings of the Institution of Mechanical Engineers, Part K: Journal of Multi-body Dynamics*, 224(3):261–277, 2010.

[73] D.J. Rixen. A dual Craig-Bampton method for dynamic substructuring. *Journal of Computational and Applied Mathematics*, 168(1):383–391, 2004.

[74] S. Rubin. Improved component-mode representation for structural dynamic analysis. *AIAA Journal*, 13:995–1006, 1975.

[75] A.A. Shabana. Flexible multibody dynamics: review of past and recent developments. *Multibody System Dynamics*, 1(2):189–222, 1997.

[76] A.A. Shabana. *Dynamics of multibody systems*. Cambridge University Press, 2005.

[77] H. Sjoväll. The load distribution within ball and roller bearings under given external radial and axial load. *Teknisk Tidskrift, Mekaniska*, page 9, 1933.

[78] J.T. Spanos and W.S. Tsuha. Selection of component modes for flexible multibody simulation. *Journal of Guidance, Control, and Dynamics*, 14:278–286, 1991.

[79] A.Z. Szeri. *Fluid film lubrication*. Cambridge University Press, 2010.

[80] T.M. Wasfy and A.K. Noor. Computational strategies for flexible multibody systems. *Applied Mechanics Reviews*, 56(6):553–614, 2003.

[81] R.A. Wehage and E.J. Haug. Generalized coordinate partitioning for dimension reduction in analysis of constrained dynamic systems. *Journal of Mechanical Design*, 104:247, 1982.

[82] J. Zeischka, L.S. Mayor, M. Schersen, and F. Maessen. Multi-body dynamics with deformable bodies applied to the flexible rotating crankshaft and the engine block. In *Proceedings of ASME*, volume 94, 1994.

[83] X.M. Zhang, Y.Q. Wang, and J. Fang. Dynamic simulation of crank-connecting rod-piston mechanism of internal combustion engine based on virtual prototype technology. *Applied Mechanics and Materials*, 143:433–436, 2012.